

# Single and coupled Josephson junction quantum bits



# Single and coupled Josephson junction quantum bits

## Proefschrift

ter verkrijging van de graad van doctor  
aan de Technische Universiteit Delft,  
op gezag van de Rector Magnificus prof. dr. ir. J. T. Fokkema,  
voorzitter van het College voor Promoties,  
in het openbaar te verdedigen op woensdag 2 februari 2005 om 10.30 uur

door

**Alexander Camillus Johannes TER HAAR**

natuurkundig ingenieur  
geboren te Nijmegen.

Dit proefschrift is goedgekeurd door de promotor:

Prof. dr. ir. J. E. Mooij

Toegevoegd promotor:

Dr. C. J. P. M. Harmans

Samenstelling van de promotiecommissie:

Rector Magnificus,	voorzitter
Prof. dr. ir. J. E. Mooij	Technische Universiteit Delft, promotor
Dr. C. J. P. M. Harmans	Technische Universiteit Delft, toegevoegd promotor
Prof. dr. G. E. W. Bauer	Technische Universiteit Delft
Prof. dr. P. Delsing	Chalmers University of Technology, Göteborg, Zweden
Prof. dr. ir. T. M. Klapwijk	Technische Universiteit Delft
Prof. dr. ir. B. J. van Wees	Universiteit Groningen
Dr. F. K. Wilhelm	Ludwig-Maximilians-Universität, München, Duitsland

# Preface

The work presented in this thesis is the result of more than four years of experimental work done in the Quantum Transport group at Delft University of Technology. In 2000 I started as a Ph.D. student in this group to work on Josephson junction quantum bits. It is a lot of fun to make your own Josephson junction circuit, cool it down in a dilution refrigerator, and to see that things actually work. I had a good time working in this group, and had a lot of fun working on various experiments on Josephson junction qubits. I realised that the infrastructure and experience present in the quantum transport group are of invaluable help in the ongoing research. Ofcourse I also experienced that not everything works all the time, and that sometimes you try something over and over before finally there are some results. Often many samples are fabricated and cooled down for testing. One thing I have definitely learned is that it is hard to get everything to work, and that progress is usually achieved slowly but gradually.

The work presented in this thesis could not have been done without many other people, and I would like to thank those who contributed to this work.

First of all I would like to thank my supervisors Hans Mooij and Kees Harman. They were always very enthusiastic about the ongoing measurements, and always full of new ideas. I learned a lot from working with them and enjoyed the various discussions we had. I am thankful for their help, advice, and the good cooperation during my Ph.D. research.

Many thanks go to Raymond Schouten for all his support and patience when helping out with the electronics. I would like to thank Bram van der Ende and Mascha Oossanen for their technical support and the good times at the coffee table. Also, I would like to thank Ria van Heeren for general administrative support, and Leo Lander, Wim Schot and Willem den Braver for general technical assistance and for the continuous supply of liquid helium. Several people made contributions to this work by discussions and practical advice, and by being good colleagues in the flux qubit team, and I would like to mention Hannes Majer, Jelle Plantenberg, Adrian Lupascu, Floor Paauw, Marko van der Krogt, Patrice Bertet, Jonathan Eroms, Peter Hadley, Irinel Chiurescu, Yasu Nakamura and Ad

Verbruggen. I especially want to thank Caspar van der Wal and Frank Wilhelm, from whom I learned a lot in the years that I worked with them. Also, I enjoyed working together with students who I supervised and want to thank Allard, Paul, Erwin and Pieter for their hard work and the good times we had during and after work.

I had a good time with my office companions Ronald, Jeroen and Adrian and want to thank them for their friendship and the many conversations about physics and non physics subjects we had. Many other people made me enjoy my time in QT, and I want to thank Erwin, Hubert, Floris, Jordan, Laurens, Eugen, Sami, Ivo, Dionne, Jorg, Stijn, Thomas, Marlies, Pablo, Frank, Silvano, Herre, Yuki, Lieven, Leo and all the other people who were part of QT in recent years.

I have enjoyed being in the quantum transport group, and will look back on this period as a very pleasant time!

*Alexander ter Haar*  
*December 2004*

# Contents

<b>1</b>	<b>Introduction</b>	<b>1</b>
	References . . . . .	4
<b>2</b>	<b>The Josephson persistent current qubit</b>	<b>7</b>
2.1	Introduction . . . . .	8
2.2	The Josephson persistent current qubit . . . . .	9
2.3	The SQUID detector . . . . .	14
2.4	Pulsed measurement scheme. . . . .	17
2.5	Decoherence due to the circuitry . . . . .	20
2.6	Summary . . . . .	26
	References . . . . .	27
<b>3</b>	<b>Coupled Josephson Persistent Current Qubits</b>	<b>29</b>
3.1	Introduction . . . . .	30
3.2	Qubit-qubit coupling via the flux . . . . .	30
3.3	Qubit-qubit coupling via a junction or a shared line . . . . .	33
3.4	The energy spectrum of the coupled qubit system . . . . .	37
3.5	Measurements showing the qubit-qubit coupling . . . . .	43
3.6	Conclusions . . . . .	50
	References . . . . .	51
<b>4</b>	<b>Coherent manipulation of two coupled Josephson Persistent Current Qubits</b>	<b>53</b>
4.1	Introduction . . . . .	54
4.2	Transitions from the ground state and the partially populated first excited state . . . . .	55
4.3	Coherent transitions from the ground state to higher states. . . . .	63
4.4	Conditional spectroscopy from the first excited state to higher states. . . . .	68
4.5	Conclusions . . . . .	73
	References . . . . .	73

---

<b>5</b>	<b>Phase distribution in current carrying double layer superconducting lines</b>	<b>75</b>
5.1	Introduction . . . . .	76
5.2	Modelling a double layer separated by a thin oxide barrier . . . . .	76
5.3	Stationary solutions for the current and phase distribution . . . . .	80
5.4	Application of a double layer distributed junction as coupling element	86
5.5	Summary . . . . .	86
	References . . . . .	87
<b>6</b>	<b>Gradiometer qubit with trapped fluxoid bias</b>	<b>89</b>
6.1	Introduction . . . . .	90
6.2	Dephasing due to an unstable flux bias . . . . .	91
6.3	Gradiometer qubit with phase bias by a superconducting trap loop	93
6.4	Spectroscopy Measurements . . . . .	96
6.5	Conclusions . . . . .	99
	References . . . . .	100
	<b>Summary</b>	<b>103</b>
	<b>Samenvatting</b>	<b>105</b>
	<b>Curriculum Vitae</b>	<b>107</b>
	<b>Publications</b>	<b>109</b>

# Chapter 1

## Introduction

Ever since quantum mechanics was shown to be successful in explaining the way atoms work in the beginning of last century the limits of its validity have been investigated. Schrödinger's famous thought experiment consists of a microscopic two-state system, for which quantum mechanics is supposed to be valid, linked to a macroscopic system (for example a cat), which is supposed to behave classically, so that the fate of the cat ('alive' or 'dead') is linked to the state of the quantum two state system ( $|0\rangle$  or  $|1\rangle$ ). The conclusion that a superposition of the quantum system would lead to a superposition of the cat's fate was the beginning of numerous discussions about the interpretation of quantum mechanics.

It was experimentally confirmed that indeed quantum mechanics has some remarkable features which are unknown in classical mechanics. Long distance entanglement between photons was demonstrated in EPR [1] experiments, and tests of Bell's inequalities have shown that quantum correlations are larger than would be possible in classical systems [2, 3]. This peculiar behaviour leads to the question how the classical world emerges from the microscopic quantum world. Numerous experiments were proposed to investigate this issue. The use of superconducting devices was proposed to test the idea that one can make superpositions of macroscopic flux states [4]. Some other remarkable experiments include an interference experiment in which the path-information can be erased after the photon has passed the double slit [5], and an experiment showing interference patterns not using electrons or photons but using large molecules [6].

The fact that the amount of information needed to describe a quantum system grows exponential with the size of the system led to the idea that quantum systems might be suitable to perform certain tasks more efficiently than would be possible in classical systems. Quantum cryptography allows for setting up a secure communication link between two parties: Any third party trying to determine the states of a sequence of bits of information would disturb the state

of the system since the basis in which the information is encoded is not known beforehand, and an eavesdropper would have to guess the basis used by the sending party. This disturbance can then be detected by the communicating parties, and they would know if a third party tried to gain information from the bits that have been sent. Quantum cryptography has been shown to work over many kilometres using photons, and is one of the first applications of quantum information processing which people are starting to use in practice. The discovery of actual quantum algorithms gave rise to the idea that people might one day build a quantum computer to perform certain calculations with an exponential increase in efficiency compared to a classical computer. Shor's factorizing algorithm can be used to factorize a large number in its primes in a number of steps that is a polynomial function of the size of the problem whereas it would take an exponential number of steps to perform the same task classically. The first experiments showing the principle of this algorithm were performed in NMR experiments [7]. Also teleportation of quantum information has been achieved in NMR systems [8]. However, the NMR system is hard to scale to a large number of qubits.

In the last decade many proposals have been put forward to building a scalable system of coupled qubits. Proposals include using trapped ions, in which conditional two qubit quantum operations have been shown recently [9, 10]. Other candidates for building large designable quantum systems are solid state devices like spin or charge of electrons in quantum dots [12], nuclear spins in silicon [11], and devices using superconducting Josephson junctions. The advantage of solid state devices is that conventional techniques can be used to fabricate these systems as they have most in common with the way contemporary computers are constructed. The disadvantage however, may be the large coupling to unwanted degrees of freedom which is always there since these systems consist of many atoms.

The advantages and disadvantages of all systems will become more clear once people will try to couple many quantum two level systems. For a small number of quantum systems promising results have been achieved, and experimental tests of entanglement between spatially separated devices and test of Bell's inequalities in solid state systems are likely to be performed in a few years time.

Coherent oscillations in a Josephson junction system were first demonstrated in a cooper pair box. Other systems in which coherent operations are achieved [13, 14, 15, 16, 17, 18] are a single large Josephson junction biased in such a way that only a few levels are present in the potential well, as well as a charge/phase system, and the Josephson persistent current qubit discussed in this thesis.

Conditional gate operations have been performed in a set of coupled Cooper-pair boxes [19] and coupling of superconducting flux systems has been achieved

[20, 21].

This thesis is about the Josephson persistent current qubit, which consists of a superconducting ring intersected by three Josephson junctions. Coherence in a single Josephson persistent current qubit was first shown a few years ago. The main focus now is on improving coherence of the single system as well as finding ways to create a network of these systems to show entanglement between spatially separated qubits, and to perform quantum algorithms in Josephson junction systems. Focus on improving the coherence of a single system are on reducing flux noise using gradiometer designs and on reducing the unwanted effects of the measurement and control circuitry on the quantum system. In addition technological progress is needed to fabricate high-quality reproducible junctions to decrease critical current noise in the junctions.

### **Outline of this thesis**

This thesis describes measurements on single and coupled Josephson persistent current qubits. The basic principles of this system as well as the measurement device are presented in chapter 2. In chapter 3, coupling of two qubits via the flux degree of freedom is discussed. Measurements showing coupling in a two-qubit system with mainly geometrical coupling are presented as well as measurements on a two-qubit system where coupling was achieved using a shared Josephson junction. In chapter 4, measurements of coherent Rabi oscillations between the states of a coupled qubit system flipping either qubit of the system are presented, as well as conditional spectroscopy measurements. Spectroscopy measurements from the ground state and the first excited state to higher states reveal the energy spectrum of the coupled qubit system. In chapter 5 we model the double layer structures which are created since we use shadow evaporation for fabrication of our Josephson junctions. Precise knowledge of the phase distribution in these layers allows them to be used as large junctions. Finally, in chapter 6 spectroscopy measurements on a gradiometer-type persistent current qubit show trapped fluxoid bias can be used to correctly bias the qubit.

### **Acknowledgements**

The measurements on the first coupled qubit sample in chapter 3 have been performed together with Hannes Majer, who started the coupled qubit project, and Floor Paauw. The measurements in chapter 3 on the second sample and the measurement in chapter 4 have been performed together with Pieter de Groot. The spectroscopy measurements on the gradiometer qubit described in chapter 6

have been performed together with Erwin Heeres and in cooperation with Jelle Plantenberg.

## References

- [1] A. Einstein, B. Podolsky, and N. Rosen , "Can Quantum-Mechanical Description of Physical Reality Be Considered Complete?", *Phys. Rev.* **47**, 777 (1935).
- [2] J.S. Bell, "On the Einstein Podolsky Rosen paradox", *Physics*, 195 (1964).
- [3] S.J. Freedman and John Clauser, "Experimental test of local Hidden-variable Theories", *Phys. Rev. Let.* **28**, 14 (1972).
- [4] A. J. Leggett, A. Garg, "Quantum mechanics versus macroscopic realism: Is the flux there when nobody looks?", *Phys. Rev. Let.* **54**, 857 (1985).
- [5] M. O. Scully, B.G. Englert, and H. Walther, "Quantum optical tests of complementarity", *Nature* **351**, 111 (1991).
- [6] M. Arndt, O. Nairz, J. Vos-Andreae, C. Keller, G. Zouw, A. Zeilinger, "Waveparticle duality of C60 molecules", *Nature* **401**, 680 (1999).
- [7] L. M. K. Vandersypen, M. Steffen, G. Breyta, C. S. Yannoni, M. H. Sherwood, and I. L. Chuang, "Experimental realization of Shor's quantum factoring algorithm using nuclear magnetic resonance", *Nature* **414**, 883 (2001).
- [8] M. A. Nielsen, E. Knill, R. Laflamme, "Complete quantum teleportation using nuclear magnetic resonance", *Nature* **396**, 52 (1998).
- [9] Ferdinand Schmidt-Kaler, Hartmut Häffner, Mark Riebe, Stephan Gulde, Gavin P. T. Lancaster, Thomas Deuschle, Christoph Becher, Christian F. Roos, Jrgen Eschner, Rainer Blatt, "Realization of the Cirac - Zoller controlled-NOT quantum gate", *Nature* **422**, 408 (2003).
- [10] D. Leibfried, B. DeMarco, V. Meyer, D. Lucas, M. Barrett, J. Britton, W. M. Itano, B. Jelenkovi, C. Langer, T. Rosenband, D. J. Wineland, "Experimental demonstration of a robust, high-fidelity geometric two ion-qubit phase gate ", *Nature* **422**, 412 (2003).
- [11] B. E. Kane, "A silicon-based nuclear spin quantum computer", *Nature* **393**, 133 (1998).
- [12] Daniel Loss, David P. DiVincenzo, "Quantum computation with quantum dots", *Phys. Rev. A* **57**, 120 (1998).

- 
- [13] Y. Nakamura, Yu. A. Pashkin, J.S. Tsai, "Coherent control of macroscopic quantum states in a single-Cooper-pair box", *Nature* **398**, 786 (1999).
- [14] D.Vion, A. Aassime, A. Cottet, P. Joyez, H. Pithier, C. Urbina, D. Esteve, M.H. Devoret, "Manipulating the quantum state of an electric Circuit", *Science*, **296**, 886 (2002).
- [15] Yang Yu, Siyuan Han, Xi Chu, Shih-l Chu, Zhen Wang, *Science* **296**, 889 (2002).
- [16] J. Martinis, S. Nam and J. Aumentado, "Rabi Oscillations in a Large Josephson-Junction Qubit", *Phys. Rev. Lett.* **89** 117901 (2002).
- [17] I. Chiorescu, Y. Nakamura, C. J. P. M. Harmans, J. E. Mooij, "Coherent quantum dynamics of a superconducting flux-qubit", *Science* **299**, 1869 (2003).
- [18] T. Duty, D. Gunnarsson, K. Bladh and P. Delsing, "Coherent dynamics of a Josephson charge qubit", *Phys. rev B* **69**, 140503 (2004).
- [19] T. Yamamoto, Yu. A. Pashkin, O. Astafiev, Y. Nakamura, J. S. Tsai, "Demonstration of conditional gate operation using superconducting charge qubits", *Nature* **425**, 941 (2003).
- [20] A. Izmalkov, M. Grajcar, E. Ilichev,<sup>1</sup> Th.Wagner, H.-G. Meyer, A.Yu. Smirnov, M. H. S. Amin, Alec Maassen van den Brink, and A.M. Zagoskin, "Evidence for Entangled States of Two Coupled Flux Qubits", *Phys. Rev. Let* **93** (2004).
- [21] J. B. Majer, F.G. Paauw, A.C.J. ter Haar, C.J.P.M. Harmans, J.E. Mooij, "Spectroscopy on two coupled superconducting flux qubits", cond-mat/0308192.



## Chapter 2

# The Josephson persistent current qubit

The Josephson persistent current qubit consists of a superconducting loop intersected by three Josephson junctions. For an applied flux bias of half a flux quantum the potential energy forms a double well potential, making this system act as a quantum two-level system. A SQUID can be used to read out the flux signal produced by the Josephson persistent current qubit.

## 2.1 Introduction

The use of superconducting structures for investigating macroscopic quantum behaviour started with the possibility to fabricate underdamped Josephson junctions in the end of the seventies [1]. Since then superconducting Josephson systems have been proposed to investigate macroscopic super positions of flux states in such systems [2]. Interest in these designable superconducting quantum systems was boosted when the concept of quantum computation became known. Since then other superconducting systems were proposed and coherent quantum dynamics in many of these systems was achieved [3, 4, 5, 6, 7, 8]. The main focus in many of these experiments now lies in improving the coherence properties of these system, and to find way to couple a number of them to show two qubit operations and to perform test on Bell's inequalities in solid state systems. In this chapter basic properties of the Josephson persistent current qubit will be discussed [9]. The Josephson persistent current qubit is a system that consists of a loop intersected with three Josephson junctions. When a flux bias of  $\Phi = \frac{1}{2}\Phi_0$  is applied the Josephson energy of the junctions form a double well potential making the system act as a two state quantum system, usable as a quantum bit. For investigating the properties of single and entangled quantum systems one needs to find a measurement method suitable for the specific system under consideration. The properties of this measurement system are of importance since any measurement will influence the quantum system. A weak measurement will only give partial information, and will only influence the quantum state slightly. A strong measurement allows for determining the state with one measurement. Such a measurement will force the system to be in the state measured after the measurement is performed. For superconducting flux qubits one can measure the phase of the system by detecting the flux produced by the qubit using a SQUID (Superconducting Quantum Interference Device) magnetometer coupled to the system via the mutual inductance. One can either measure the Josephson inductance of the SQUID by putting it in a resonance circuit [10, 11, 12] and detecting the resonance frequency, or measure the switching current of the SQUID. The advantage of the first method is that no switching to the finite voltage state of the SQUID takes place, but the second method is simpler to implement. In this chapter first the general properties of this qubit system like the energy spectrum will be shown. The states of the system will be treated as an artificial spin and the Hamiltonian will be written using Pauli spin matrices. For the measurements in this thesis a SQUID is used to determine the state of the qubit. In section 2.3 some junction and SQUID basics will be given, and the escape rates for thermal excitation and quantum tunnelling will be compared. After this in section 2.4

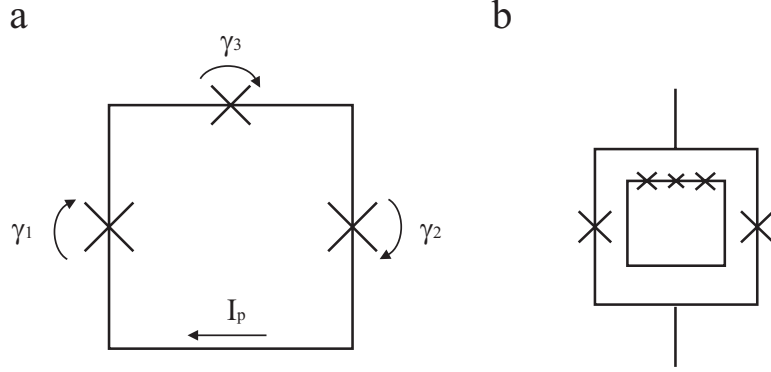


**Figure 2.1:** The Josephson persistent current qubit consists of a superconducting loop with three junctions. One junction is smaller by a factor of  $\alpha \approx 0.6-0.8$ . (b) A SQUID surrounding the qubit is used for measuring the flux signal produced by the qubit.

the pulsed measurement scheme will be studied. Finally decoherence properties of the qubit due to the measurement and control circuitry will be discussed.

## 2.2 The Josephson persistent current qubit

The Josephson persistent current qubit [9] consists of a superconducting aluminium ring intersected with three Josephson junctions (see figure 2.1).

The energy of the system is given by the potential energy  $V$ , which is a function of the phases  $\gamma_i$ , and the kinetic energy  $T$ , a function of  $\dot{\gamma}_i$ , given by

$$V_{Jos} = E_J [2 + \alpha - \cos(\gamma_1) - \cos(\gamma_2) - \alpha \cos(-\gamma_1 - \gamma_2 - 2\pi \frac{\Phi}{\Phi_0})] \quad (2.1)$$

$$T = \frac{1}{2} C \frac{\Phi_o}{2\pi} \dot{\gamma}_1^2 + \frac{1}{2} C \frac{\Phi_o}{2\pi} \dot{\gamma}_2^2 + \frac{1}{2} \alpha C \frac{\Phi_o}{2\pi} (\dot{\gamma}_1 + \dot{\gamma}_2)^2 \quad (2.2)$$

where  $\gamma_1$  and  $\gamma_2$  are the phases over the Josephson junctions.  $I_p$  is the persistent current flowing in the loop. The eigen energies of the system are shown in figure 2.2 as a function of the applied flux  $\Phi$ . Around a flux bias of  $\Phi = \frac{1}{2}\Phi_0$  the two classical energies cross. The system has two stable states, with opposite circulating currents, given by the slopes of the levels with respect to flux. The tunnel coupling  $\Delta$  depends on the barrier between the two local minima and can be numerically calculated. For  $\frac{E_J}{E_c} \sim 60$  and  $E_J \sim 150GHz$  the tunnelling is of the order of a few Giga Hertz. A smaller  $\alpha$  means the barrier between the wells

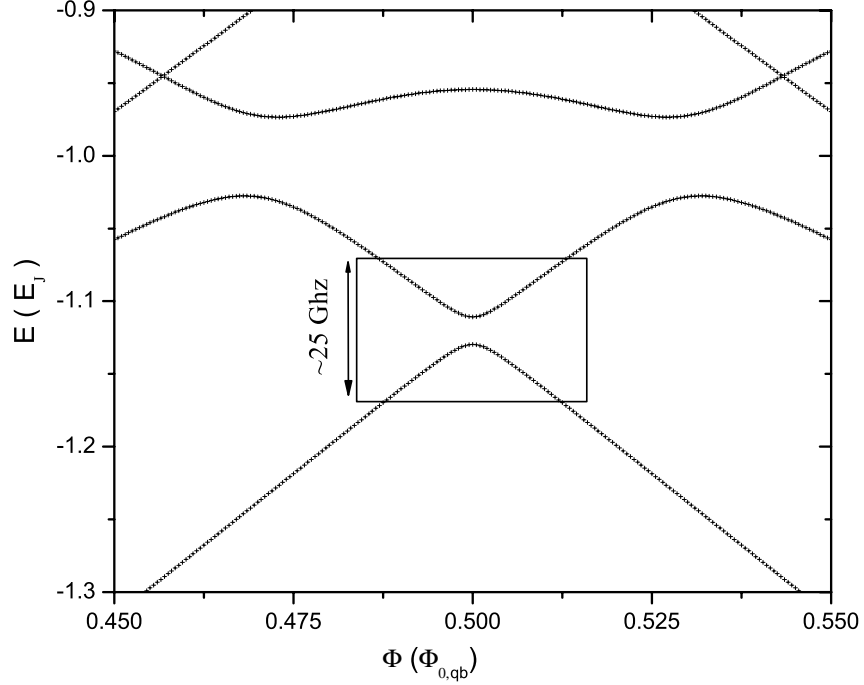


**Figure 2.2:** Energy levels of a Josephson persistent current qubit. Around  $\Phi = \frac{1}{2}\Phi_0$  the system can be described by the two classical current states corresponding to the minima in the potential energy and a tunneling term between the wells.

is lower so tunnelling is increased (see figure 2.3). Tunnel coupling between these two states creates an anti crossing between the classical energy levels, visible in the centre of the energy diagram in figure 2.2, and can be measured using spectroscopy measurements [13]. Around  $f = \frac{1}{2}$  the classical persistent currents are independent of the applied flux. Away from half a flux quantum through the loop (in figure 2.2 at  $f = 0.47$  and  $f = 0.53$ ) the second level changes slope indicating the current associated with it changes direction; The double well potential is tilted so far that two levels can be present in the lowest well before there is any occupation of the highest well.

In figure 2.4 the potential landscape along the  $\gamma_1 = \gamma_2$  direction is plotted. The system has two stable states at the bottom of the energy wells with positive and negative phase  $\gamma$  and thus with positive and negative circulating persistent currents  $I_p = \pm I_c \sin \gamma$  in the loop [9]. The position of the energy minima are,

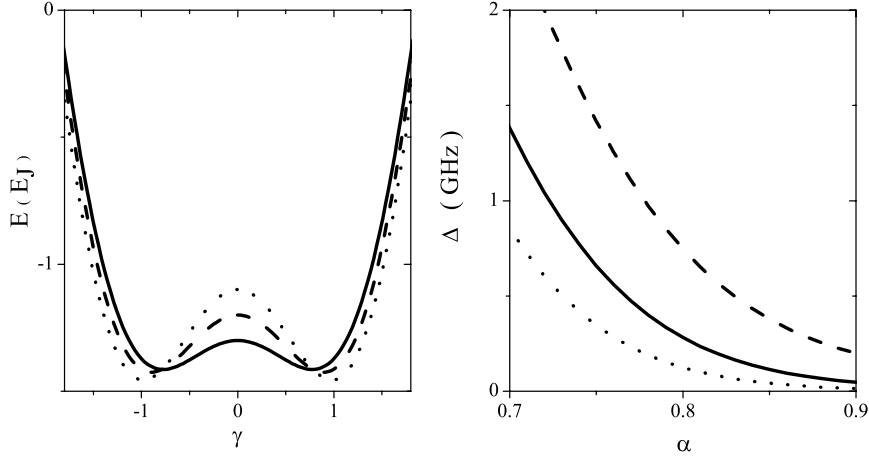


**Figure 2.3:** The tunnel coupling  $\Delta$  between the wells is mainly determined by the barrier between the local minima which depends strongly on  $\alpha$ , the ratio of the smallest junction and the larger junctions. The potential landscape is plotted for  $\alpha = 0.7$ , 0.8 and 0.9 with  $\frac{E_J}{E_c} = 60$  and  $E_J = 150\text{GHz}$ . The tunnel coupling  $\Delta$  is plotted for  $E_J = 150\text{GHz}$  and  $\frac{E_J}{E_c} = 40$  (dashed),  $\frac{E_J}{E_c} = 60$  (solid) and  $\frac{E_J}{E_c} = 80$  (dotted). The tunnel coupling is increased for small  $\alpha$  since the barrier is lowered. For lower charging energy  $E_c$  the tunneling is reduced.

near half a flux quantum, independent of the applied flux. Therefore the persistent current  $I_p$  is independent of the flux for a given well. The classical energy associated with the energy minima of the double well potential is

$$E_{0,1} = \pm I_p \left( \Phi - \frac{1}{2} \Phi_0 \right) \quad (2.3)$$

The system can be described as a two-state system or pseudo spin [9] in terms of the Pauli spin matrices  $\sigma_z$  and  $\sigma_x$  as

$$\mathbf{H}_\Phi = -\frac{\epsilon}{2} \sigma_z + \frac{\Delta}{2} \sigma_x = \begin{pmatrix} -\frac{\epsilon}{2} & \frac{\Delta}{2} \\ \frac{\Delta}{2} & \frac{\epsilon}{2} \end{pmatrix} \quad (2.4)$$

where  $\epsilon = 2I_p(\Phi - \frac{1}{2}\Phi_0)$  is the classical energy bias of the qubit.  $\Delta$  is the tunnel coupling between the wells. This gives eigen energies of the system as  $E_{0,1} = \mp \sqrt{(\frac{\epsilon}{2})^2 + (\frac{\Delta}{2})^2}$  giving a level splitting  $E_1 - E_0$  of  $\nu = \sqrt{\epsilon^2 + \Delta^2}$  as plotted in figure 2.4b. The dashed lines are the classical energies of the system.

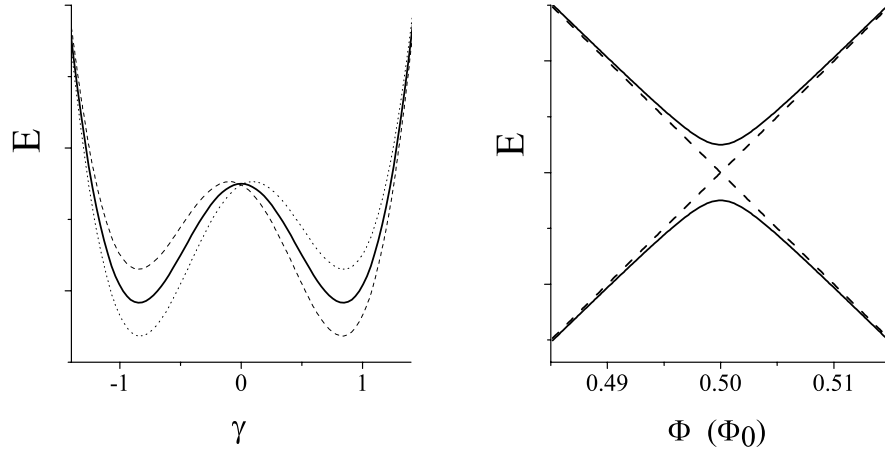


**Figure 2.4:** The double well potential can be tilted by applying a flux to the qubit loop. Around a flux bias of  $\Phi = \frac{1}{2}\Phi_0$  the system behaves as a two state system. The classical energy of the two states is given by  $E = \pm I_p(\Phi - \frac{1}{2}\Phi_0)$

The Hamiltonian can be transformed by rotating the matrix according to  $UHU^*$  where  $U$  contains the normalised eigenvectors of the Hamiltonian in the flux basis

$$\mathbf{H}_{\text{eig}} = \begin{pmatrix} -\frac{1}{2}\sqrt{\epsilon^2 + \Delta^2} & 0 \\ 0 & \frac{1}{2}\sqrt{\epsilon^2 + \Delta^2} \end{pmatrix} \quad (2.5)$$

### Excitation of the system using an oscillating flux

When a cosine like  $\sigma_x$  perturbation is applied in resonance with the difference in energy between the levels the quantum state  $\psi = \alpha|0\rangle + \beta|1\rangle$ , the system performs coherent Rabi oscillations between the eigenstates of the system [15]. In the case of the Josephson persistent current qubit the system can be excited by applying a microwave frequency magnetic flux  $\delta\Phi_{mw} = |\Phi_{mw}|\sin(\omega t)$  to the system, where  $|\Phi_{mw}|$  is the amplitude and  $\omega$  is the frequency of the signal. This gives a change in the energy bias of the system according to  $\epsilon_{mw} = 2I_p(\delta\Phi_{mw})$ . This radiation is applied in the  $\sigma_z$  direction in the flux-basis. The part of the microwave radiation that ends up in the  $\sigma_x$  direction is calculated by transforming the microwave Hamiltonian  $H_{mw} = -\frac{\epsilon_{mw}}{2}\sigma_z = -\Phi_{mw}I_p\sigma_z$  using  $UH_{mw}U^*$  where  $U$  is the matrix rotating the unperturbed Hamiltonian to its diagonal form (equation 2.5). This

gives for the microwave Hamiltonian in the eigen basis of the system

$$\mathbf{H}_{\text{eig}} = \begin{pmatrix} -\frac{\epsilon}{\sqrt{\epsilon^2 + \Delta^2}} \frac{\epsilon_{mw}}{2} & \frac{\Delta}{\sqrt{\epsilon^2 + \Delta^2}} \frac{\epsilon_{mw}}{2} \\ \frac{\Delta}{\sqrt{\epsilon^2 + \Delta^2}} \frac{\epsilon_{mw}}{2} & \frac{\epsilon}{\sqrt{\epsilon^2 + \Delta^2}} \frac{\epsilon_{mw}}{2} \end{pmatrix} \quad (2.6)$$

The part of the radiation coupling as  $\sigma_x$  to our qubit is then given by  $\frac{\Delta}{\sqrt{\epsilon^2 + \Delta^2}} \Phi_{mw} I_p$ .

### Spectroscopy measurements on a Josephson persistent current qubit

Measurements on the Josephson persistent current qubit are performed at low temperatures ( $T \sim 15mK$ ) in a dilution refrigerator. Signals from room temperature down to the sample in the cryostat are filtered using copper powder filters to filter out any high frequency noise in the current bias lines or the voltage measurement lines. Microwave attenuators are placed at the various temperature stages to attenuate thermal noise from higher temperatures. The substrate of  $5mm$  by  $5mm$  on which the Josephson persistent current qubit and the SQUID are fabricated is placed inside a cavity with connections for the dc measurement signal and for the microwave signal. To reduce substrate heating and to reduce influence of quasi particles produced after each switching event measurements are performed at a repetition rate of  $\sim 1kHz$ .

The qubit signal is picked up by a SQUID whose critical current depends on the total flux through the SQUID loop. A typical measurement consist of fixing the applied microwave frequency and power and then sweeping the flux around the region  $\Phi = \frac{1}{2}\Phi_0$  (see figure 2.5). The 'step' at  $\Phi = \frac{1}{2}\Phi_0$  occurs since the ground state energy of the system changes slope indicating a change in persistent current of the qubit from clockwise to counter-clockwise. At those values of the external field where the applied microwave radiation is resonant with the qubit energy splitting resonance peaks are visible meaning the system is partially excited to the higher state through the continuous microwave radiation and an incoherent mixture is formed.

### Coherent Rabi oscillations between qubit states

When the flux bias is fixed at resonance and microwaves are applied the system coherently performs Rabi oscillations as a function of the duration of the applied micro wave pulse, as shown in figure 2.6. Oscillations flipping one qubit in a coupled qubit system are shown. In this example the oscillations shown have a decay time of the order of  $60ns$ .

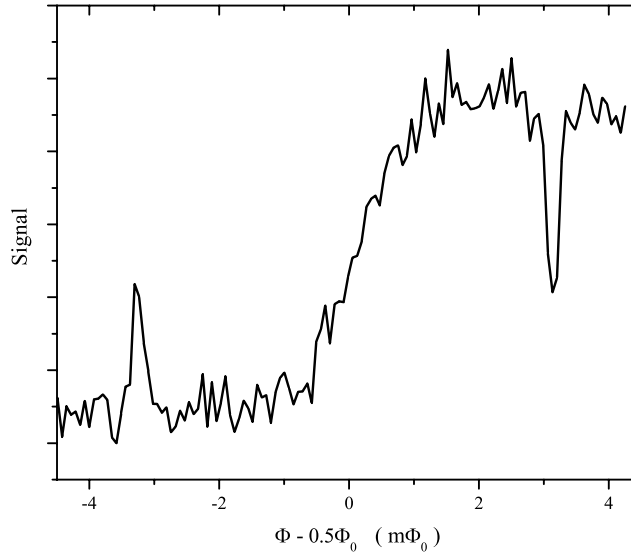


**Figure 2.5:** Measured qubit signal for applied microwave frequency  $f = 14.34\text{GHz}$  for various values of the external magnetic field. The characteristic step around  $\Phi = \frac{1}{2}\Phi_0$  indicates the qubit ground state changes character as we move through the degeneracy point. The peak on the left side and the dip on the right indicate the applied microwaves are resonant with the energy levels of the qubit and the system is incoherently pumped from the ground state to the first excited state.

## 2.3 The SQUID detector

A SQUID can be used as a magnetometer either by detecting its switching current which depends on the flux through the loop, or by using the Josephson inductance in a resonant circuit and detecting the resonance frequency. The Josephson potential of a junction gives a cosine like potential in which the phase is at rest in one of the energy minima. By applying a bias current  $I_{bias}$  through the junction the potential landscape formed by the Josephson energy is tilted [23, 24, 16]. When a bias current  $I_{bias} > I_c$ , where  $I_c$  is the critical current of the junction, is applied the potential landscape no longer forms energy minima. Around this point the phase will start to roll and the junction will leave the zero-voltage state and switch to the finite voltage state. Escape will occur before this point is reached due to thermal excitation or quantum tunnelling [1, 16] at a point called the switching current  $I_{sw} < I_c$ . Since this switching is a statistical process there

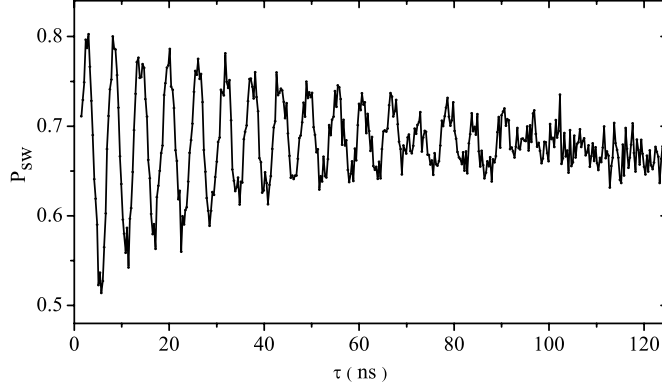


**Figure 2.6:** Rabi oscillations flipping a single qubit in a coupled qubit system. The system oscillates coherently between the ground state and the first excited state with a level distance of  $f = 9.4\text{GHz}$ .

is a spread in switching currents as is visible in figure 2.7). The current through the junction is slowly ramped to a finite value many times after each other and each time the switching current is detected to build the histogram.

Both thermal escape and quantum tunnelling escape will be discussed here briefly but in experiments performed the SQUIDs used are in the quantum tunnelling regime. The escape rate of either process is determined by the plasma frequency and the barrier height. The plasma frequency at zero bias current is given by

$$\omega_{p,0} = \sqrt{\frac{2\pi I_c}{\Phi_0 C}} \quad (2.7)$$

where  $I_c$  is the critical current of the junction, and  $C$  is the capacitance of the junction. The plasma frequency decreases at finite bias currents due to the less steep potential according to  $\omega_p = \omega_{p,0}\sqrt{1 - i^2}$  with  $i = \frac{I_b}{I_c}$ . The potential energy as a function of the applied current is given by [1, 16]

$$\Delta U = \frac{I_c \Phi_0}{2\pi} (2\sqrt{1 - i^2} - 2\arccos(i)) \quad (2.8)$$

Thermal escape is given by

$$\Gamma_{escape} = \omega_p e^{-\frac{\Delta U}{k_B T}} \quad (2.9)$$

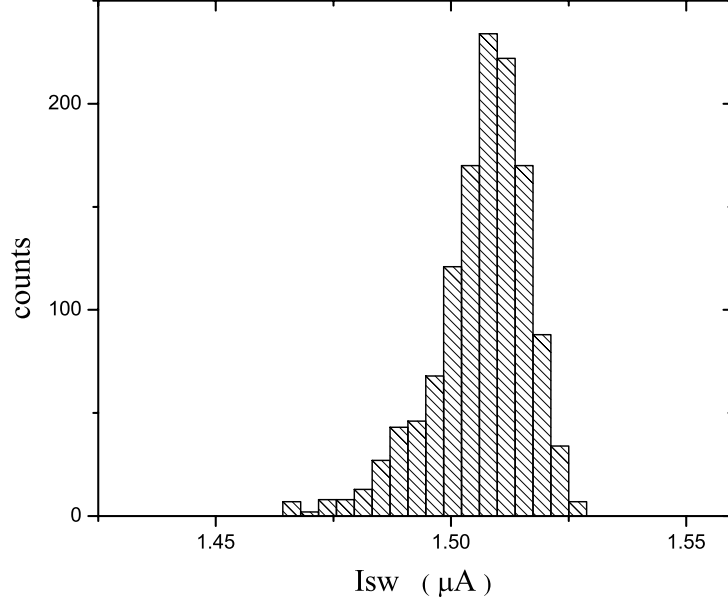


**Figure 2.7:** Measured switching current distribution. By repeatedly ramping the current at a rate of  $\sim 1\mu\text{A}/\text{ms}$  and detecting the moment the SQUID switches to the finite voltage state one can build a histogram.

Here  $T$  is the temperature and  $\Delta U$  is the barrier height to overcome at a given bias current. For quantum tunnelling this rate is [1]

$$\Gamma_{\text{escape}} = a_q \omega_p e^{-\frac{36}{5} \frac{\Delta U}{\hbar \omega_p}} \quad (2.10)$$

where  $a_q = \sqrt{120\pi \frac{36}{5} \frac{\Delta U}{\hbar \omega_p}}$ . By comparing these we find the transition between quantum tunnelling and thermal escape at  $\frac{5}{36} \hbar \omega_p \approx k_B T$ .

### The SQUID as a magnetometer

The potential energy of a SQUID as seen in figure 2.8 is given by the sum of the Josephson energies of the junctions [23]. The maximum current that can be sent through the SQUID without switching to the finite voltage state is depending on the flux through the SQUID loop. The SQUID thus behaves as a flux-tunable junction with a critical current given by

$$I_{c,sq} = 2I_{c,j} |\cos(\pi f)| \quad (2.11)$$

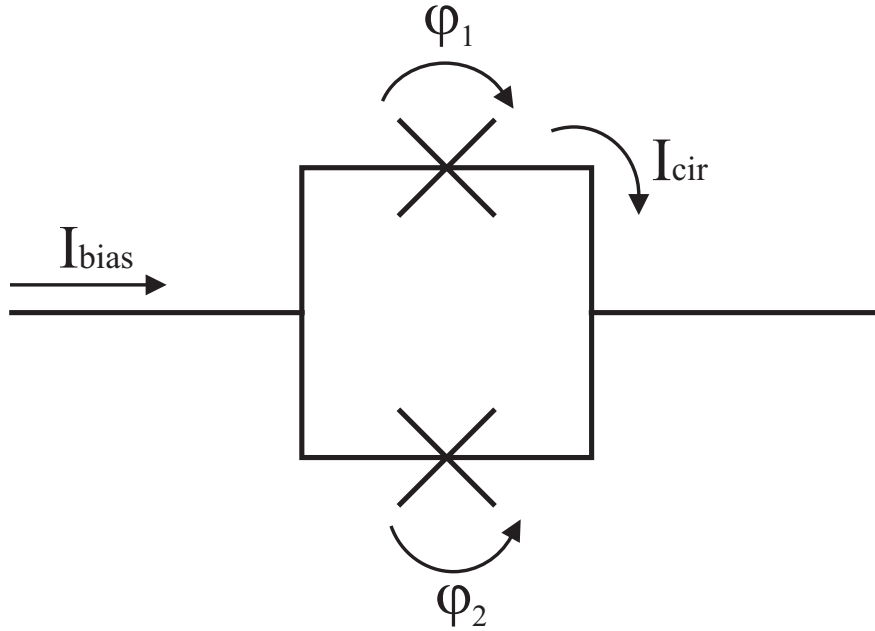


**Figure 2.8:** Schematic layout of a SQUID. The maximum current through the junctions is modulated with the flux through the SQUID loop, making it useful as a magnetometer.

since the flux modulates the barrier height in the  $\phi_{ext}$  direction. It is this dependence of the barrier height on the flux which makes it useful as a magnetometer. The measured switching current of a typical SQUID versus magnetic field is seen in figure 2.9 where the cosine like behaviour of the critical current as a function of the flux is visible. The SQUID is designed to be operated somewhere on the slope of the curve. By making the coupling to the measurement system high the qubit state can be determined with one or a few measurements but then also decoherence due to coupling to the measurement circuit is high. On the other side a low coupling means every single measurement only reveals part of the information of the state under consideration and averaging over many experiments is needed to determine its state for sure. The important factor is the relative change in escape rate of the SQUID induced by the qubit.

## 2.4 Pulsed measurement scheme.

For measuring the state of a single or coupled qubit system a bias current pulse (figure 2.10) is sent through the SQUID after manipulation of the qubit is performed. Measurement has to be performed before the system relaxes to the

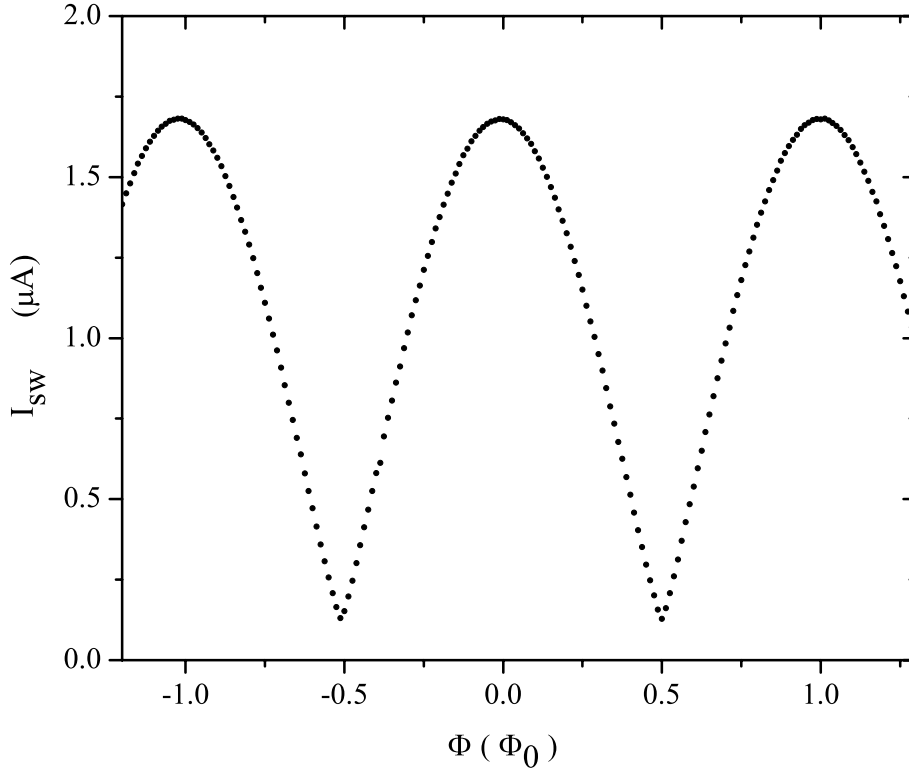


**Figure 2.9:** Measured switching current of a SQUID versus flux applied to the SQUID loop. Each point is an average switching current of 100 switching events. The dependence of the switching current on the flux is used to determine the state of the qubit.

ground state and all information is lost. This means the measurement has to be performed within tens of nanoseconds to a few microseconds after the operations. This relaxation time depends on the details of the specific system parameters.

Depending on the flux in the SQUID loop the switching probability will change and the state of the qubit can be determined. Typical measurement pulse times  $\tau_{meas}$  used are of the order of  $20ns - 2000ns$ . To be able to detect whether the SQUID has switched during the measurement pulse a tail to the measurement pulse is added to keep the system in the finite voltage state for a longer time. The escape rate for the quantum tunnelling case is plotted in figure 2.11 for various values of the capacitance seen by the external degree of freedom. The sensitivity of the SQUID is determined by the change of the escape rate  $\Gamma$ . For

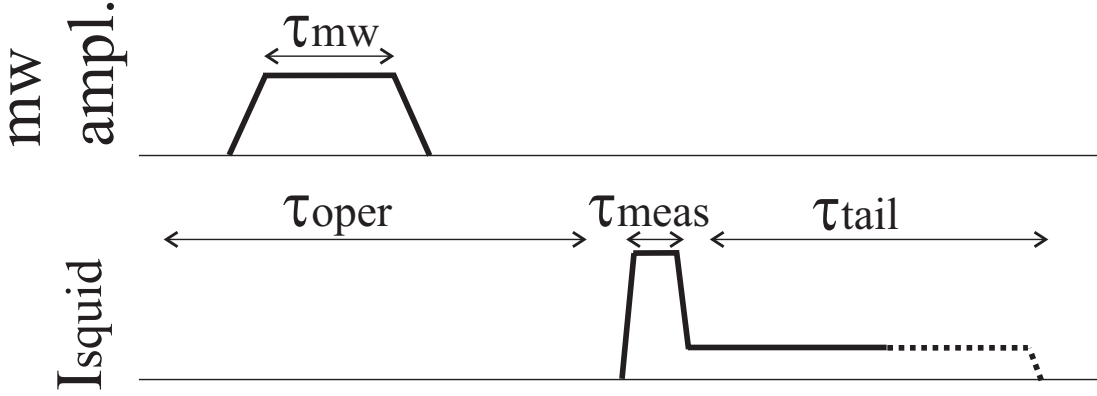


**Figure 2.10:** First qubit operations are performed by applying micro wave pulses to the qubit. Then a current pulse of time  $\tau_{meas}$  is applied to the SQUID. To measure if the SQUID switched to the finite voltage state a tail in the applied measurement pulse is added to keep the SQUID in the finite voltage state. The switching probability of the SQUID  $P_{sw}$  is a measure for the flux produced by the qubit and thus for the qubit state.

$C = 25 \cdot 10^{-14}$ ,  $C = 0.25 \cdot 10^{-12}$  and  $C = 2.5 \cdot 10^{-12}$  the escape rates are plotted. Clearly visible is the dependence on the capacitance: A higher capacitance gives a steeper slope and thus makes the measurement more sensitive. For a constant bias current pulse of time  $\tau_{meas}$  the probability that the SQUID has switched after a bias current pulse is given by

$$P_{switch} = 1 - e^{-\Gamma\tau_{meas}} \quad (2.12)$$

where  $\Gamma$  is the escape rate for a given bias current  $I_{bias}$  as given in equation 2.10 and  $\tau_{meas}$  is the length of the applied pulse. For a pulse length of  $\tau_{meas} = 500ns$  and a critical current of  $I_c = 1\mu A$  the switching probability can be seen in figure 2.12. Also the sensitivity of the escape to a change in the relative bias current to the SQUID  $i = \frac{I_{bias}}{I_c}$  is plotted. The measurement is most sensitive when the pulse height is tuned around this maximum in slope of  $P$  versus  $i$ . In figure 2.13 the measured switching probability of a capacitively shunted SQUID versus applied bias current is plotted. The on-chip capacitor has a value of  $C \sim 1.25pF$ . The theoretical line plotted has a capacitance of  $C \sim 0.25pF$ . The escape chance for various capacitances is plotted in figure 2.14. The measured switching probability curve thus indicates that the effective mass associated with the phase of the system is only partially influenced by the external capacitance. This is attributed to the inductance of the line connecting the SQUID to the external capacitance. For high frequencies this inductance is a large impedance

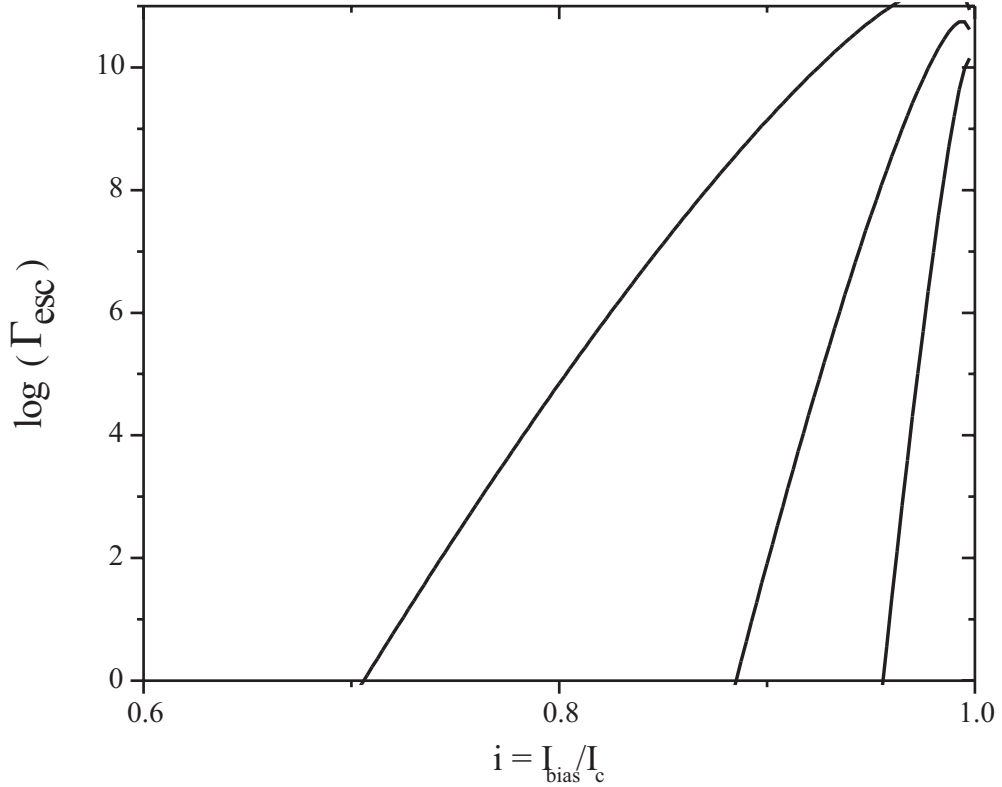


**Figure 2.11:** Escaperate  $\Gamma_{esc}$  as a function of the bias current through the SQUID  $i = \frac{I_{bias}}{I_c}$ . Different plots are for capacitances  $C = 25 \cdot 10^{-14}$ ,  $C = 0.25 \cdot 10^{-12}$  and  $C = 2.5 \cdot 10^{-12}$ . For a pulsed measurement the pulse height is set such that the escape chance is  $\sim 50\%$  for a given pulselength  $\tau_{meas}$ .

so the capacitor only partially feels the voltage fluctuation over the SQUID. The effective mass is much more then the estimated junction capacitance which is of the order of  $C \sim 5fF$ , indicating the external capacitance still partially influences the switching.

## 2.5 Decoherence due to the circuitry

The relaxation and dephasing rates of a quantum system are determined by coupling to its environment. The system can lose energy to (emission) or gain energy from (absorption) the environment at a typical time scale called the mixing time  $T_1$ . Also, noise from the environment can cause the energy difference  $\Delta E = E_1 - E_0$  between the levels of the quantum system to fluctuate causing dephasing at a typical time scale  $T_2$ . Many sources of decoherence can be present, such

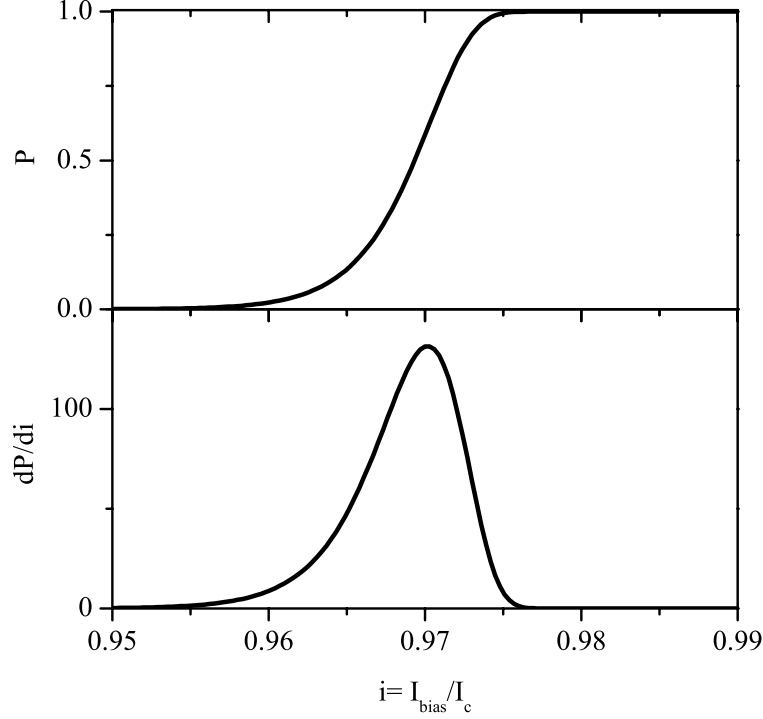


**Figure 2.12:** *Top: Escape chance  $P$  versus the bias current for a measurement pulse of  $\tau = 500\text{ns}$  and a critical current of  $I_c = 1\mu\text{A}$ . Bottom: Derivative of the escape chance  $P$  with respect to the relative applied bias current  $i$ . For the most sensitive readout the SQUID is operated at the maximum of this curve.*

as flux or charge noise. Here the coupling to the environment via the on-chip electrical circuitry will be considered. This environment can be characterized by the resistors, capacitors and inductances seen by the qubit. The spectral density of the voltage noise caused by a resistive environment depends on the real part of the impedance of the environment. This spectral density can be described by the following expression [22]:

$$S_V(\omega) = \frac{2\Re(Z(\omega))\hbar\omega}{1 - e^{-\hbar\omega/k_B T}} \quad (2.13)$$

The spectral density is defined at positive and negative frequencies to take into account the fact that the environment can absorb ( $\omega > 0$ ) and emit ( $\omega < 0$ ) energy (figure 2.15) from and to the qubit.

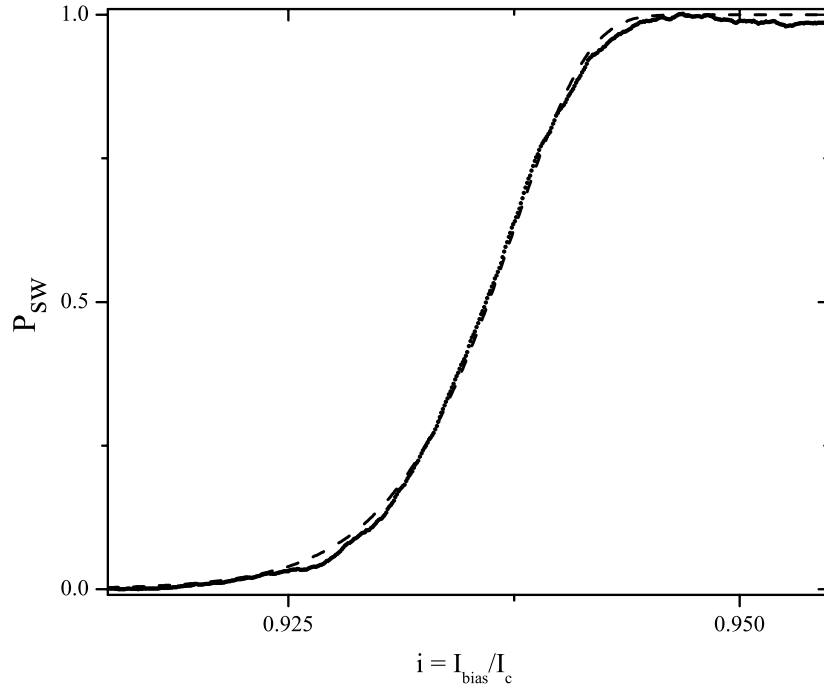


**Figure 2.13:** Measured switching probability of a  $C$ -shunted SQUID as a function of  $i = \frac{I_b}{I_c}$ . The width of the transition region from no switching (on the left) to always switching (on the right) is determined by the capacitance and the critical current. The dashed line is the theoretical switching probability for  $I_c = 1.45 \mu\text{A}$  and  $C = 0.25 \text{pF}$ . The value of the capacitance indicates only a part of the external capacitance counts for the mass of the phase ball in the Josephson potential.

For a temperature of  $T = 0$  only the positive frequencies are present in the spectrum indicating only absorption of energy by the environment can take place, while at high temperatures both rates are equal leading to an equal distribution of the population between the levels.

### Relaxation of a two level system

The absorption rate and emission rate for the qubit absorbing or emitting energy from and to the environment are described by [22]

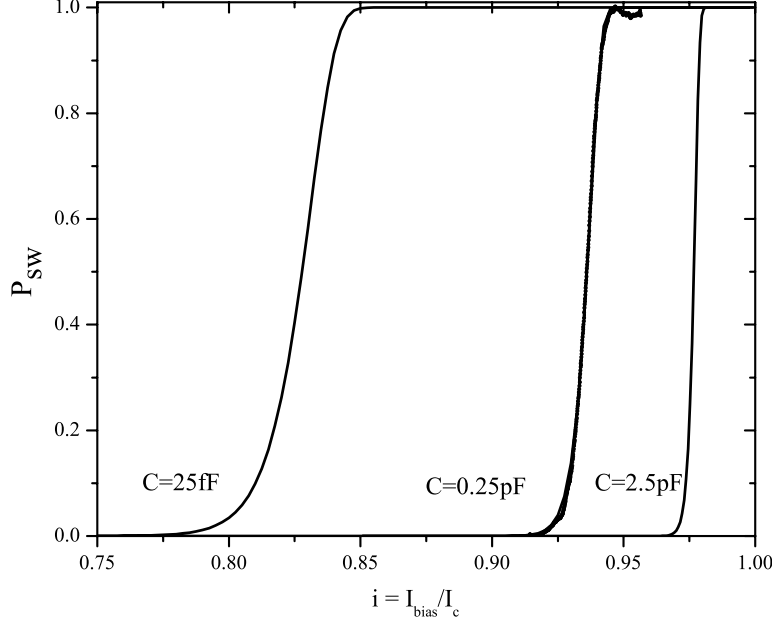


**Figure 2.14:** *Theoretical switching curves for  $C = 25\text{fF}$ ,  $C = 0.25\text{pF}$  and  $C = 2.5\text{pF}$ . The first value is approximately the expected junction capacitance, and the last value is the capacitance value of the external shunt capacitor. The data is fitted with a capacitance of  $C = 0.25\text{pF}$ .*

$$\Gamma_{\downarrow,\uparrow} = \frac{1}{\hbar^2} S_E(\pm\omega) = \frac{A^2}{\hbar^2} S_V(\pm\omega) \quad (2.14)$$

where  $S_E(\pm\omega)$  is the spectral density of the energy fluctuation seen by the qubit as  $\sigma_x$ . The factor  $A$  determines how the voltage fluctuations  $S_V$  are translated in  $\sigma_x$  fluctuations in the Hamiltonian of the two level system. The steady state situation can be obtained by looking at the rates at which energy is absorbed or emitted. Mixing of the system to the steady state situation is determined by both adsorption and emission at the frequency of the energy difference of the transition. Any excursion from the equilibrium situation of the polarisation  $P = p_0 - p_1$ , with  $p_0$  the ground state population and  $p_1$  the excited state population, will decrease according to

$$\delta P(t) = \delta P(0) e^{-(\Gamma_{\downarrow} + \Gamma_{\uparrow})t} \quad (2.15)$$

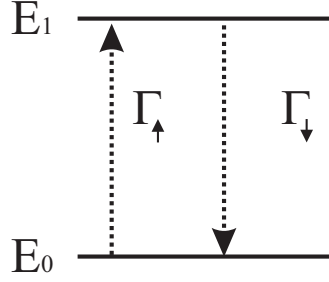


**Figure 2.15:** The qubit can undergo transition from the ground state to the excited state and visa versa by absorbing or emitting a photon from the environment.

so the mixing rate  $\Gamma_r$  is given by [17, 18, 19, 20, 21]

$$\Gamma_r \equiv \frac{1}{T_1} = \frac{A^2}{\hbar^2} (S_V(-\omega) + S_V(+\omega)) \quad (2.16)$$

This rate is the rate at which the polarisation of the system  $P = p_0 - p_1$  will go to the steady state situation  $P_0$ , and can for the spectrum of equation 2.13 be written as

$$S_{V,tot} = S_V(-\omega) + S_V(\omega) = 2\Re(Z(\omega))\hbar\omega \coth\left(\frac{\hbar\omega}{2k_B T}\right) \quad (2.17)$$

### Dephasing

Noise from the environment can cause dephasing given by [17, 18]

$$\Gamma_\phi = \frac{\Gamma_r}{2} + \frac{\epsilon^2}{\nu^2} \alpha 2\pi \frac{2k_B T}{\hbar} \quad (2.18)$$

where  $\alpha$  is the limit for low frequencies of the spectral density of the noise .

### Relaxation and dephasing due to SQUID and microwave circuitry

The factor  $A$  in equation 2.16 is determined by the coupling of the noise of the environment to the energy levels of the quantum system. The electrical environment seen by the Josephson persistent current qubit consists of a microwave line used to apply a varying magnetic field to the qubit and a C-shunted SQUID used for measuring the qubit signal, see figure 2.16. Voltage fluctuations are caused by the effective resistances  $R_{mw}$  and  $R_l$  in the microwave line and the SQUID.

Any voltage  $\delta V$  over the SQUID translates to current through the SQUID which in turn translates to a change in circulating current in the SQUID. These

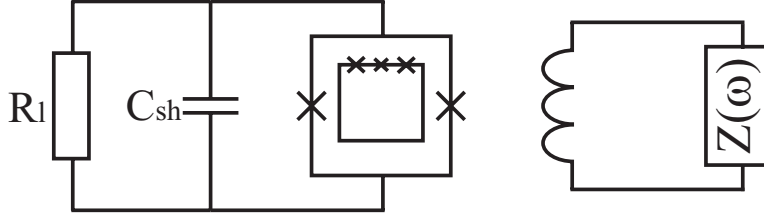


**Figure 2.16:** *The measurement circuit connected to the DC SQUID surrounding the qubit and the circuit connected to the microwave guides for applying a high frequency oscillating flux to the qubit can all cause relaxation and dephasing of the quantum system of interest. The electrical environment can be designed in such a way that the effect of noise causing relaxation and dephasing is minimized.*

fluctuations cause flux fluctuations in the qubit causing relaxation. The voltage noise is given by the impedance as seen by the SQUID given by the SQUID inductance in parallel with the shunt capacitor and the resistor  $R_l$ .  $M_{sq,qb}$  determines the flux coupling from the qubit to the SQUID loop and takes into account how the circulating current in the squid translates to flux in the qubit. There can also be direct coupling of the SQUID bias line to the qubit,  $M_{bias,qb}$ . This contribution can be reduced by using a symmetric configuration of the SQUID with respect to the qubit. For a Josephson persistent current qubit coupled to a SQUID or to microwave leads with various types of environments (C-shunt, RC-shunt and microwave leads) this relaxation is discussed in [17, 18, 21]. The resulting relaxation rate due to the SQUID is given by

$$\Gamma_{r,sq} = \frac{1}{\hbar} \frac{\Delta^2}{\epsilon^2 + \Delta^2} \frac{1}{\omega} I_p^2 M_{sq,qb}^2 \tan^2(\pi f) \left( \frac{2\pi 2I_{sq}}{\Phi_0} \right)^2 \Re(Z(\omega)) \coth\left(\frac{\hbar\nu}{2k_B T}\right) \quad (2.19)$$

where  $C$  and  $R_l$  are the capacitance and resistance values (figure 2.16).  $M$  is the mutual inductance from the SQUID to the qubit and  $I_p$  is the persistent current in the qubit. The microwave circuit gives a relaxation rates of

$$\Gamma_{r,mw} = \frac{\Delta^2/\hbar^2}{\hbar\omega} \frac{(M_{mw}I_p)^2}{R_{mw}} \coth\left(\frac{\hbar\nu}{2k_B T}\right) \quad (2.20)$$

with  $M_{mw,qb}$  the inductive coupling from the microwave line to the qubit, and  $R_{mw} = 50\Omega$  the impedance seen in the microwave line.

The relaxation times for typical system parameters are plotted in figure 2.17. In designing the qubit-SQUID system one should take into account that the operating point of the system should not coincide with the SQUID resonance (around  $f = 2.5GHz$  in the figure) since the influence of fluctuations in the environment is enhanced. Assumed is an asymmetry in the SQUID junctions of

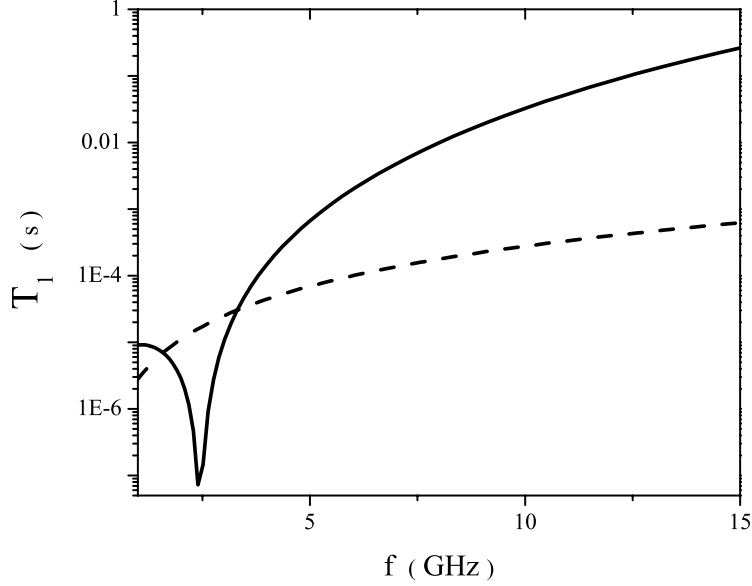


**Figure 2.17:** Relaxation rates for a typical qubit ( $I_p = 300\text{nA}$ ,  $\Delta = 1\text{GHz}$ ) due to coupling to the SQUID measurement circuit (solid line) and the microwave line (dashed line).

10 percent and circuit parameters are  $C = 20\text{pF}$ ,  $R_l = 100\Omega$  and  $I_{c,sq} = 2500\text{nA}$ . The SQUID is operated at a point where the critical current is reduced to  $1500\text{nA}$ . Coupling from the SQUID to the qubit is  $M = 8\text{pH}$  and coupling from the microwave lead to the qubit is  $M = 0.1\text{pH}$ .

The dephasing rates due to the SQUID and microwave environment are given by [18]

$$\Gamma_{\phi,sq} \approx \frac{(2\pi)^2}{\hbar^2} \left( \frac{M_{sq} I_p}{\Phi_0} \right)^2 I_{sq}^2 \tan^2(f) \frac{L_J^2}{R} k_B T \quad (2.21)$$

$$\Gamma_{\phi,mw} \approx \frac{4}{\hbar^2} \frac{(M_{mw} I_p)^2}{R_{mw}} k_B T \quad (2.22)$$

## 2.6 Summary

The Josephson persistent current qubit can be used as an artificial two level system near a frustration of half a flux quantum through the qubit loop. A

SQUID can be used to pick up the flux signal produced by the quantum system under consideration. The design of the measurement circuit is of importance for the sensitivity of the SQUID as a measurement device for the Josephson persistent current qubit. Experimental tests indicate there is a limit to the effectiveness of an external shunt capacitor as far as the sensitivity of the SQUID is concerned. Also, in designing the on-chip circuitry one has to take care that the noise from resistors in the measurement circuit, the microwave circuit or flux bias lines does not cause severe decoherence of the system.

## References

- [1] R.F. Voss and R.A. Webb, "Macroscopic quantum tunnelling in a 1- $\mu$ m Nb Josephson junctions", *Phys. Rev. Lett.* **47**, 265 (1981).
- [2] A. J. Leggett, A. Garg, "Quantum mechanics versus macroscopic realism: Is the flux there when nobody looks?", *Phys. Rev. Lett.* **54**, 857 (1985).
- [3] Y. Nakamura, Yu. A. Pashkin, J.S. Tsai, "Coherent control of macroscopic quantum states in a single-Cooper-pair box", *Nature* **398**, 786 (1999).
- [4] D.Vion, A. Aassime, A. Cottet, P. Joyez, H. Pithier, C. Urbina, D. Esteve, M.H. Devoret, "Manipulating the quantum state of an electric Circuit", *Science*, **296**, 886 (2002).
- [5] Yang Yu, Siyuan Han, Xi Chu, Shih-l Chu, Zhen Wang, *Science* **296**, 889 (2002).
- [6] J. Martinis, S. Nam and J. Aumentado, "Rabi Oscillations in a Large Josephson-Junction Qubit", *Phys. Rev. Lett.* **89**, 117901 (2002).
- [7] I. Chiorescu, Y. Nakamura, C. J. P. M. Harmans, J. E. Mooij, "Coherent quantum dynamics of a superconducting flux-qubit", *Science* **299**, 1869 (2003).
- [8] T. Duty, D. Gunnarsson, K. Bladh and P. Delsing, "Coherent dynamics of a Josephson charge qubit", *Phys. rev B* **69**, 140503 (2004).
- [9] T. P. Orlando, J. E. Mooij, L. Tian, C. H. van der Wal, L. S. Levitov, S. Lloyd, J. J. Mazo, "Superconducting persistent-current qubit", *Phys. Rev. B* **60**, 15398 (1999).
- [10] I. Siddiqi, R. Vijay, F. Pierre, C. M. Wilson, M. Metcalfe, C. Rigetti, L. Frunzio, and M. H. Devoret, "RF-Driven Josephson Bifurcation Amplifier for Quantum Measurement", *Phys. Rev. Lett.* **93**, 207002 (2004).

- [11] A. Lupascu, C. J. M. Verwijs, R. N. Schouten, C. J. P. M. Harmans, and J. E. Mooij, "Nondestructive Readout for a Superconducting Flux Qubit", *Phys. Rev. Lett.* **93**, 177006 (2004).
- [12] J. C. Lee, W. Oliver, T. Orlando, and K. Berggren, "Resonant readout of a persistent current qubit" (2004) .
- [13] C. H. van der Wal, A.C.J. ter Haar, F.K. Wilhelm, R.N. Schouten, C.J.P.M. Harmans, T.P. Orlando, Seth Lloyd, J.E. Mooij, *Science* **290**, 773 (2000).
- [14] T. Orlando and Delin, "Foundations of Applied Superconductivity", Addison-Wesley publishing company (1991).
- [15] C. Cohen-Tannoudji , "Quantum Mechanics", J.Wiley and Sons, (1977).
- [16] Fulton and Dunkelberger, "Lifetime of the zero-voltage state in Josephson tunnel junctions", *Phys. Rev. B* (1974).
- [17] C.H. van der Wal, "Quantum Superpositions of Persistent Josephson Currents", PhD Thesis (2001).
- [18] C.H. van der Wal, F.K. Wilhelm, C.J.P.M. Harmans, J.E. Mooij, "Engineering decoherence in Josephson persistent current qubits", *Eur. Phys. J. B.* (2001).
- [19] M. Grifoni, E. Paladino, U. Weiss, "Dissipation, decoherence and preparation effects in the spin-boson system", *Eur. Phys. J. B.* **10**, 719 (1999).
- [20] M. Governale, M. Grifoni, G. Schon, "Decoherence and dephasing in coupled Josephson-junction qubits" (2000).
- [21] M. J. Storcz , F.K. Wilhelm, "Decoherence and gate performance of coupled solid state qubits", *Phys. Rev. A.* **67**, 042319 (2003)
- [22] R.J. Schoelkopf, A.A. Clerk, S.M. Girvin, K.W. Lehnert and M.H. Devoret, "Qubits as spectrometers of quantum noise", cond-mat/0210247 (2002).
- [23] T. Orlando and Delin, "Foundations of Applied Superconductivity", Addison-Wesley publishing company (1991).
- [24] M. Tinkham, "Introduction to Superconductivity" (1975).

## Chapter 3

# Coupled Josephson Persistent Current Qubits

The principles of coupling Josephson persistent current qubits are discussed and measurements showing the qubit-qubit coupling of two qubits with geometrical coupling and of two qubits with coupling via kinetic inductance are presented.

### 3.1 Introduction

Two coupled Josephson persistent current qubits are studied for investigating the principles of quantum computation as well as performing measurements on entangled systems. Coupling of superconducting systems has been achieved in Cooper-pair boxes and in Josephson persistent current qubits [1, 2, 3, 4]. We want qubits to be coupled in a controlled way, and ultimately a tunable coupling is needed [5]. The goal of this work is to show that qubits can be coupled and that the full four dimensional Hilbert space of this system can be exploited. In order to do this, we must first understand the mechanisms leading to the coupling, and investigate the energy levels and transition probabilities of a coupled quantum system. Josephson persistent current qubits can be coupled inductively. In this chapter the energy levels of inductively coupled qubits are mapped out using spectroscopy measurements. In section 3.2 the origin and magnitude of flux coupling is discussed. Another way to achieve this coupling between two flux qubits is via their phase degree of freedom using a shared line (and its kinetic inductance) or a shared Josephson junction (and its Josephson inductance) for the current in the qubits to flow through. This will be treated in section 3.3, where these mechanisms will be linked to the simpler case where there are only fluxes involved. It will become clear that all these extra phase coupling mechanisms enter the equations in a similar way, and that these terms can all be summed up to form one simple expression. In section 3.5 experimental results on coupled qubits are presented, and coupling of two Josephson persistent current qubits will be shown in two samples using either geometrical coupling (sample A) or coupling via a shared junction (sample B).

### 3.2 Qubit-qubit coupling via the flux

Josephson persistent current qubits can be coupled via their flux by putting them next to each other. Depending on the flux state of one qubit the flux bias of the other is influenced and visa versa. Here the coupling energy  $J$  involved in going from the uncoupled to the coupled situation is deduced for the configuration shown in figure 3.1.

#### The energy of the coupled qubit system

To calculate the coupling one has to derive the total potential energy of the coupled system. The potential energy can be divided into two parts. First there is the energy in the Josephson junctions  $E_J$  due to the phase bias. When there is

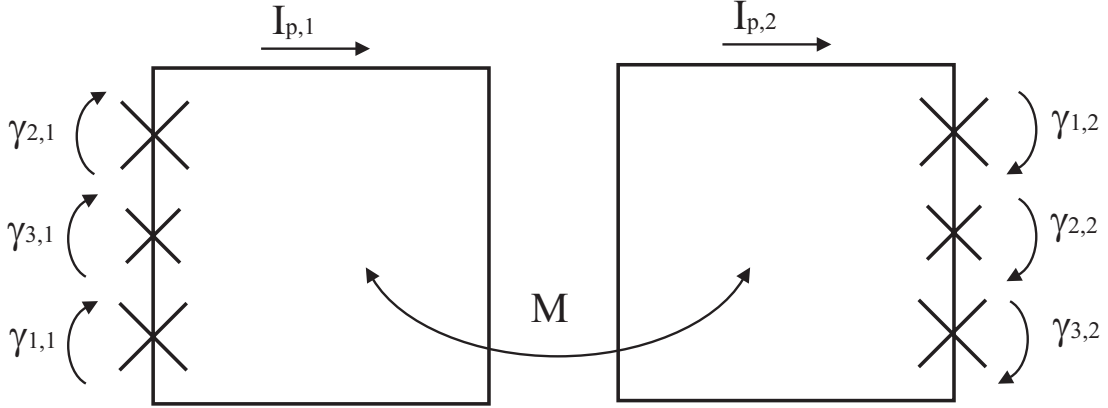


**Figure 3.1:** Two Josephson persistent current qubits can be coupled via their flux. The phases over each qubit are influenced via flux quantisation by the flux produced by the other qubit. Also energy is stored in the mutual magnetic field between the qubits depending on the fluxes adding or subtracting from each other.

coupling the qubits influence each others phase bias and thus change the energy. Second, there is the potential energy stored in the mutual magnetic field of the qubits  $E_{magn}$ . Near  $f = \frac{1}{2}$  the qubits are loops with a persistent current of  $I_p = \pm I_{p,0}$ . Since each loop produces a flux in the other loop there is a magnetic energy involved. From this the difference in potential energy  $J = \Delta E_J + \Delta E_{magn}$  between the case of two uncoupled and two coupled qubits will be derived. It will be shown that, near  $f = \frac{1}{2}$ , the ratio between the energy terms is given by  $2E_J = -E_{magn}$ .

### The Josephson energy in the junctions of each individual qubit.

The Josephson part of the energy of the system as shown in figure 3.1 is given by

$$V_{Jos} = \sum_{i \in \{1,2\}} E_{J,i} [2 + \alpha - \cos(\gamma_{1,i}) - \cos(\gamma_{2,i}) - \alpha \cos(\gamma_{3,i})] \quad (3.1)$$

with  $E_{J,i}$  the Josephson energy of the large junctions of the  $i$ 'th qubit and  $\alpha$  the ratio of the small junction compared to the large junctions. Applying flux quantization for each loop ( $i \in [1, 2]$ ), gives

$$\gamma_{1,i} + \gamma_{2,i} + \gamma_{3,i} + 2\pi \frac{\Phi_{i,tot}}{\Phi_0} = 0 \quad (3.2)$$

Here the total flux in one qubit is the sum of the externally applied flux  $\Phi_{i,ext}$ , the self produced flux  $\Phi_{i,self} = L_i I_{p,i}$  and the flux produced in qubit  $i$  by qubit

$j$ ,  $\Phi_{i,j} = MI_{p,j}$ , where  $L_i$  are the geometrical self inductances of the loops, and  $M$  is the geometrical mutual inductance between the loops. This gives

$$\gamma_{1,i} + \gamma_{2,i} + \gamma_{3,i} + 2\pi \frac{\Phi_{i,ext}}{\Phi_0} + \frac{2\pi}{\Phi_0} L_i I_{p,i} - \frac{2\pi}{\Phi_0} M_{geo} I_{p,j} = 0 \quad (3.3)$$

By using (3.3) in (3.1) we have

$$V_{Jos} = \sum_{i \in \{1,2\}} E_{J,1,i} [2 + \alpha - \cos(\gamma_{1,i}) - \cos(\gamma_{2,i}) - \alpha \cos(-\gamma_{1,i} - \gamma_{2,i} - 2\pi \frac{\Phi_{i,ext} + L_i I_{p,i} - M I_{p,j}}{\Phi_0})] \quad (3.4)$$

The qubits are coupled because the phase over the junctions in one qubit is influenced by the current in the other due to flux quantisation.  $L$  and  $M$  are defined positive and the sign of the coupling is taken into account in the flux quantization rules. Near half a flux quantum the energy values of the minima (associated with a persistent current of  $\pm I_{p,0}$ ) of the double well potentials are linear in the applied flux  $\Phi_{i,tot}$  according to  $I_{p,i} = -\frac{\partial E_{Jos,i}}{\partial \Phi_{tot}}$  and thus also for the dependence on the flux created in one qubit by the other,  $I_{p,i} = -\frac{\partial E_{Jos,i}}{\partial \Phi_{i,j}}$ . For both qubits biased at  $\Phi_{i,tot} < 0.5\Phi_0$  the current associated with the ground state opposes the applied flux in that loop, so that it enhances the flux in the other loop for the configuration of figure 3.1. This means that in the linear regime around  $f = 1/2$  the system acquires an extra Josephson energy  $MI_{p,1}I_{p,2}$  when the coupling is switched on for each qubit giving for both qubits

$$\Delta E_{Jos} = 2MI_{p,1}I_{p,2} \quad (3.5)$$

This energy is positive if both persistent currents are of the same sign, indicating that there is an energy advantage for the qubits being anti parallel, and a disadvantage for the parallel configuration.

### The energy stored in the magnetic field

The second contribution to the energy associated with the coupling of two qubits is the energy stored in their common magnetic field. This contribution comes from the fact that there is energy involved in changing the configuration of current carrying loops. This energy is given by  $W = \sum_{i \in \{1,2\}} \frac{1}{2} I_i \Phi_j$  [6]. When coupling two qubits together in this way the energy in the field is decreased when the qubits are in the same state, because for currents in the same direction they decrease their mutual magnetic field and thus the total energy stored in the field is less. This

energy stored in the field means there is an energy contribution to the system when two qubits are coupled of

$$\Delta E_{magn} = -MI_{p,1}I_{p,2} \quad (3.6)$$

giving an advantage for the qubits being in the same state for the configuration in figure 3.1.

### The Qubit-Qubit coupling energy $J$

The qubit-qubit coupling energy  $J$  is the energy associated with changing the mutual inductance  $M$  from 0 to a finite value. When  $M = 0$  all coupling terms in the total potential energy disappear and the added energies of two single uncoupled qubits are obtained. The total coupling is given by  $J = \Delta E_{Jos} + \Delta E_{magn}$ , where the first part (eq. 3.5) is for parallel fluxes a positive contribution and the second part (eq. 3.6) a two times smaller negative contribution. The ratio between the terms is given by  $E_J = -2E_{magn}$ . The total qubit-qubit coupling energy is thus given by

$$J = MI_{p,1}I_{p,2} \quad (3.7)$$

For the geometry of figure 3.1 it favours the qubits to be anti parallel by an energy of  $2J$  compared to the parallel case.

## 3.3 Qubit-qubit coupling via a junction or a shared line

In this section the scenario where the loops will be coupled via an extra junction or via the kinetic inductance of a shared line is discussed. It will be shown that this kind of coupling has the same effect as the flux coupling discussed in section 3.2. For these coupling mechanisms the sign and magnitude of the coupling will be calculated.

### Using the Josephson inductance of a junction for coupling

Instead of the mutual inductance a large Josephson junction with critical current  $I_{c,cj}$  can be used to couple the qubits as in figure 3.2. The Josephson inductance  $L_J = \frac{\Phi_0}{2\pi I_c}$  determines the coupling strength.

Similar to equation (3.3) flux quantization can be rewritten to include the phase over this large junction. For persistent currents in the qubit much smaller

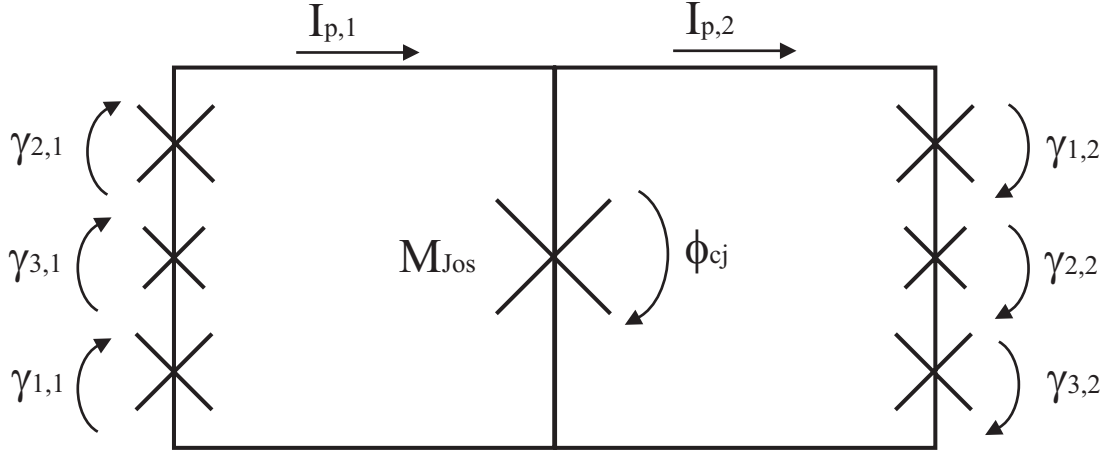


**Figure 3.2:** Schematic overview of coupling two qubits via a shared junction. Both qubits send a current through this coupling junction and thus a phase  $\phi_{cj}$  is imposed over it. This phase will influence flux quantisation of both qubits just as in the case with a magnetic field. Also there will be energy stored in the coupling junction.

then the critical current of the coupling junction the phase over this junction is given by

$$\phi_{cj} = \arcsin\left(\frac{I_{p,1} - I_{p,2}}{I_{c,cj}}\right) \approx \frac{I_{p,1} - I_{p,2}}{I_{c,cj}} \quad (3.8)$$

The Josephson energy in this junction is

$$E = E_J(1 - \cos(\phi_{cj})) \approx \frac{1}{2} \frac{\Phi_0}{2\pi} \frac{(I_{p,1} - I_{p,2})^2}{I_{c,cj}} \quad (3.9)$$

By using the Josephson inductance  $M_{Jos} = \frac{\Phi_0}{2\pi I_{c,cj}}$  [7, 8], this phase and energy can be rewritten as

$$\phi_{cj} = \frac{2\pi}{\Phi_0} M_{Jos} (I_{p,1} - I_{p,2}) \quad (3.10)$$

and

$$E = \frac{1}{2} M_{Jos} (I_{p,1} - I_{p,2})^2 \quad (3.11)$$

The first relation can be used in the part of the coupling concerned with fluxoid quantisation so we get :

$$\gamma_{1,i} + \gamma_{2,i} + \gamma_{3,i} + 2\pi \frac{\Phi_{i,ext}}{\Phi_0} + 2\pi \frac{M_{Jos}(I_{p,i} - I_{p,j})}{\Phi_0} = 0 \quad (3.12)$$

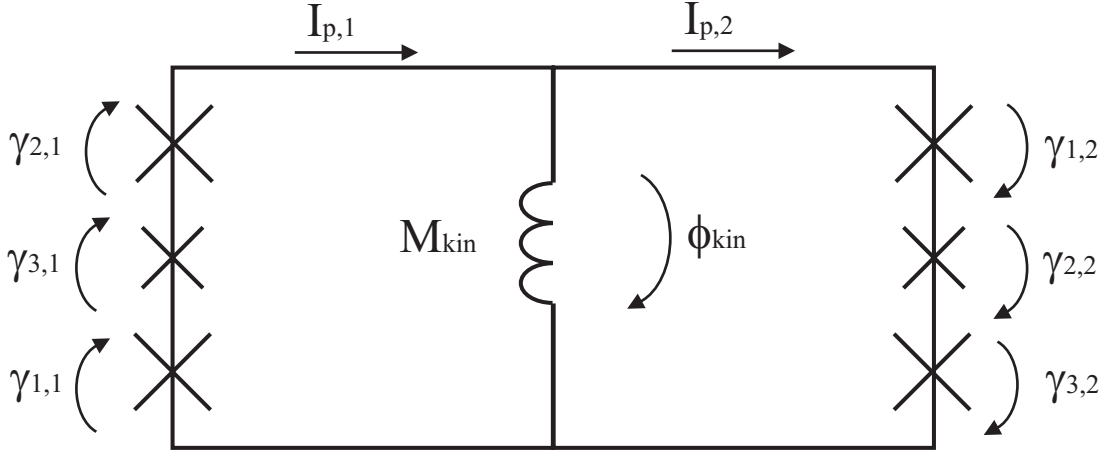


**Figure 3.3:** Schematic overview of coupling two qubits via a shared line. Again the current through this common line will impose an extra phase difference on the other qubit, and there will be energy paid or gained when changing the state of the qubits.

The second relation ( 3.11 ) gives for the energy in the medium :

$$E = \frac{1}{2}M_{Jos}I_{p,1}^2 + \frac{1}{2}M_{Jos}I_{p,2}^2 - M_{Jos}I_{p,1}I_{p,2} \quad (3.13)$$

In these terms  $M_{Jos}$  has the same role as either the self inductance  $L_{geo}$  or as the mutual inductance  $M_{geo}$  as in section (3.2) and one can go through similar arguments to arrive at an energy advantage for anti parallel qubits as compared to parallel qubit alignment of  $2J$  where

$$J_{junc} = M_{Jos}I_{p,1}I_{p,2} \quad (3.14)$$

The form of this coupling is the same as equation 3.7 with the mutual geometrical inductance replaced by the Josephson inductance of the shared junction..

### Coupling via a shared line

In the case of a shared line (3.3) there is a coupling of the two systems via the kinetic inductance of the line, just as is the case with the kinetic inductance of a shared Josephson junction. This represents the kinetic energy that is stored in the current carriers in the line [7, 8, 9]. This energy is given by

$$E = \frac{1}{2}L_{kin}I_{line}^2 \quad (3.15)$$

where the kinetic inductance is  $L_{kin} = \Lambda \frac{l}{\sigma}$ . With the current in the shared line given by  $I_{line} = I_{p,1} - I_{p,2}$  this energy is written as

$$E = \frac{1}{2}L_{kin}I_{line}^2 = \frac{1}{2}L_{kin}I_{p,1}^2 + \frac{1}{2}L_{kin}I_{p,2}^2 - L_{kin}I_{p,1}I_{p,2} \quad (3.16)$$

This is the energy stored in the line. Again we can distinguish terms which behave as the self inductance in a single qubit, and a part which behaves like the mutual inductance. We see that this energy contribution to the total  $J$  is  $-L_{kin}I_{p1}I_{p2}$ . There is a phase associated with the current flowing through this line just as with any inductance, influencing again the flux quantization of the qubits. The phase along a current carrying line with a certain kinetic inductance  $L_{kin}$  is given by

$$\Delta\theta_{kin} = L_{kin}I \quad (3.17)$$

This phase adds up to the phases due to the flux as in equation (3.3) so again there is an energy associated with this of  $2L_{kin}I_{p1}I_{p2}$ . By now adding the energy contributions we end up with an extra coupling  $J$  due to the kinetic inductance of

$$J_{kin} = +L_{kin}I_{p1}I_{p2} \quad (3.18)$$

This makes the kinetic inductance behave the same as the mutual inductance or the linearised Josephson inductance.

### Estimations for realistic systems

In realistic systems all these contributions add to the total coupling. Here the coupling strength of each of the previous terms will be estimated so we can calculate the total mutual coupling  $M = M_{geo} + M_{kin} + M_{Jos}$  and thus  $J$  for any design. For a reasonable coupling of  $J = 1.5GHz$  with persistent currents of  $I_p = 300nA$  we need a total mutual inductance of  $M \approx 10pH$ .

#### Geometric induction

For the typical size of qubits of 5 by 5 um the geometrical mutual inductance  $M_{geo}$  is only  $\sim 1 - 2pH$  if the lines are not shared and the qubits are positioned 250 nm apart, giving a coupling strength  $J$  of only a few hundred MHz. This is not so easy to make much larger (especially when the qubits are physically apart) while keeping the qubit area small. However, this contribution is always present.

#### Kinetic induction

The kinetic inductance of a line is proportional to its length and inversely proportional to its cross section. In the limit of a dirty one-dimensional superconductor  $L_{kin}$  is linked to the normal state resistance  $R_n$  as

$$L_{kin} \approx \frac{\Phi_0}{\pi^2} \frac{eR_n}{\Delta} \quad (3.19)$$

For typical lines of  $50nm$  height and  $150nm$  wide we find a value of  $2pH/\mu m$ , making it feasible to get to the wanted coupling of  $10pH$ . The line width can be made smaller to increase the coupling. This allows the kinetic inductance to be designed within a large range.

#### Josephson induction

The coupling via a Josephson junction also allows for great flexibility in designing the coupling value between the qubits since one can tune its critical current to high precision. For a value of  $L_J = 10pH$  a critical current of  $I_{c,cj} = 40\mu A$  is needed. One way to create such a large junction is to make use of the double layer structure of our lines which are unavoidably present when using shadow evaporation for fabricating the junctions (chapter 5). A line of 5 micrometer by 1 micrometer gives a critical current of  $\sim 40\mu A$  in the transverse direction. One has to make sure that the connections to this coupling junction are correct so that all currents will cross the junction. Also, for large long junctions there will be the kinetic contribution and current will redistribute along the line (see chapter 5).

### 3.4 The energy spectrum of the coupled qubit system

In order to determine the energy spectrum of this system near a frustration of  $\Phi = 1/2\Phi_0$  we use a two-level approximation to the full Hamiltonian for a single qubit. The two level system will be written using the Pauli spin matrix notation. Here this approximation will be given, and energy levels and transition elements between the levels will be calculated. Also some comments will be made on the validity of this 4-level approximation.

#### Hamiltonian of the coupled qubit system

Near  $\Phi = 0.5\Phi_0$  the qubit energy levels can be approximated by the levels of a two state system. Around this point the classical persistent currents ( $I_p = -\frac{\partial E}{\partial \Phi} = \pm I_{p0}$ ) are independent of the applied magnetic field, as can be seen in figure 3.4. The system can be described as

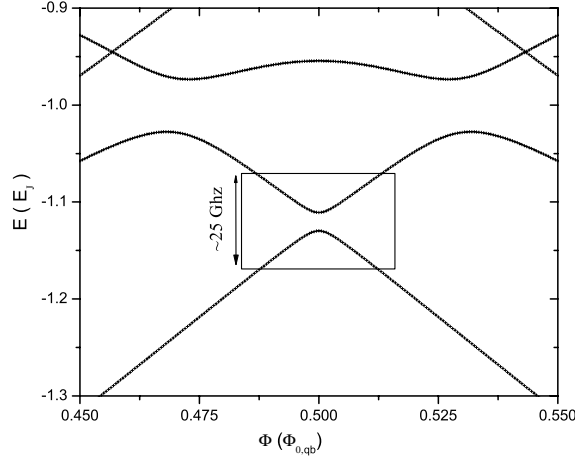


**Figure 3.4:** Energy levels of a single qubit for  $E_J/E_c = 40$  and  $I_p = 300\text{nA}$ . One can see that too far out the third level start to influence the second level.

$$\mathbf{H} = \begin{pmatrix} -\epsilon/2 & \Delta/2 \\ \Delta/2 & \epsilon/2 \end{pmatrix} \quad (3.20)$$

in the basis of the  $|\downarrow\rangle$  and  $|\uparrow\rangle$  state, similar to the case of a spin in a magnetic field. The energy bias  $\epsilon = 2I_p(\Phi - \frac{1}{2}\Phi_0)$  of the system depends on the applied flux.  $\Delta$  is the tunnel coupling between the states. For the specific case of figure 3.4 more than  $0.025\Phi_0$  away from the degeneracy point the third level crosses the second level. Here the simple two level approximation breaks down because  $I_p$  will not be independent of the applied flux any more and there will not be a fixed energy  $J$  accounting for the coupling between the qubits. In order for the two level picture to be valid  $f$  needs to be close enough to  $\Phi = \frac{1}{2}\Phi_0$  so that the third level is far away. Also in the case of a large anti ferromagnetic coupling this demand is even stricter since the shift of  $2J$  due to the coupling should also not bring us outside this region. Each of the qubits can be described as a pseudo-spin by using the Pauli spin matrices. The Hamiltonian of two uncoupled qubits looks like  $H = H_1 \otimes I_2 + H_2 \otimes I_1$  where  $H_1$  and  $H_2$  represent the individual qubits.  $I_1$  and  $I_2$  represent the identity matrices in the Hilbert space of qubit 1 and 2 respectively. This will give the following matrix in the basis of the classical persistent current states as pseudo-spin states,  $|\downarrow\downarrow\rangle$ ,  $|\downarrow\uparrow\rangle$ ,  $|\uparrow\downarrow\rangle$  and  $|\uparrow\uparrow\rangle$ :

$$\mathbf{H} = \begin{pmatrix} -\frac{\epsilon_1 + \epsilon_2}{2} & \frac{\Delta_2}{2} & \frac{\Delta_1}{2} & 0 \\ \frac{\Delta_2}{2} & -\frac{\epsilon_1 - \epsilon_2}{2} & 0 & \frac{\Delta_1}{2} \\ \frac{\Delta_1}{2} & 0 & \frac{\epsilon_1 - \epsilon_2}{2} & \frac{\Delta_2}{2} \\ 0 & \frac{\Delta_1}{2} & \frac{\Delta_2}{2} & \frac{\epsilon_1 + \epsilon_2}{2} \end{pmatrix} \quad (3.21)$$

where the energies are  $\epsilon_1 = -2I_{p,1}(\Phi_1 - \frac{1}{2}\Phi_0)$  and  $\epsilon_2 = -2I_{p,2}(\Phi_2 - \frac{1}{2}\Phi_0)$  respectively, and  $\Delta_1$  and  $\Delta_2$  are the tunnel couplings for both qubits. In this two level picture of the qubits the coupling is  $\sigma_z\sigma_z$  coupling in the basis of the flux states since the coupling described in section 3.2 couples the flux or phase degrees of freedom of two (or more) qubits. This coupling can be added to the Hamiltonian via a term  $J\sigma_1^z\sigma_2^z$  where J is given by  $J = MI_{p,1}I_{p,2}$ . The Hamiltonian now looks like

$$\mathbf{H} = \begin{pmatrix} -\frac{\epsilon_1 + \epsilon_2}{2} + J & \frac{\Delta_2}{2} & \frac{\Delta_1}{2} & 0 \\ \frac{\Delta_2}{2} & -\frac{\epsilon_1 - \epsilon_2}{2} - J & 0 & \frac{\Delta_1}{2} \\ \frac{\Delta_1}{2} & 0 & \frac{\epsilon_1 - \epsilon_2}{2} - J & \frac{\Delta_2}{2} \\ 0 & \frac{\Delta_1}{2} & \frac{\Delta_2}{2} & \frac{\epsilon_1 + \epsilon_2}{2} + J \end{pmatrix} \quad (3.22)$$

By diagonalising this matrix as a function of the applied flux bias we can determine the energy spectrum of this four level system. Asymmetries are taken into account via the different  $\Delta_i$  the differences in  $\epsilon_i$  due to a difference in surface or a difference in the persistent currents  $I_{p,i}$  of the qubits.

### Transition elements

In order to calculate the transition elements one needs to look at the way an applied oscillating magnetic field  $\Phi_{i,mw}$  couples via the energy bias  $\epsilon_i$  to the  $\sigma_x$  component of the Hamiltonian in the eigenbasis of the system. Two realistic microwave-line configurations are given in figure 3.5. In the case of identical qubits for the case as in figure 3.5a both qubits 'see' the radiation with the same phase. This means the amplitude of this oscillating flux signal is added to the flux bias  $\Phi_{i,j}$  in the 4 level approximation according to

$$\Phi_{i,tot} = \Phi_i + \Phi_{i,mw} \quad (3.23)$$

Analogous to the single qubit case (chapter 2), in order to calculate the effective power exciting the system to one of the higher levels, we should find the amplitude of the oscillating signal in the basis of the eigenstates. This is done by rotating the Hamiltonian matrix which includes the driving to the eigen basis of

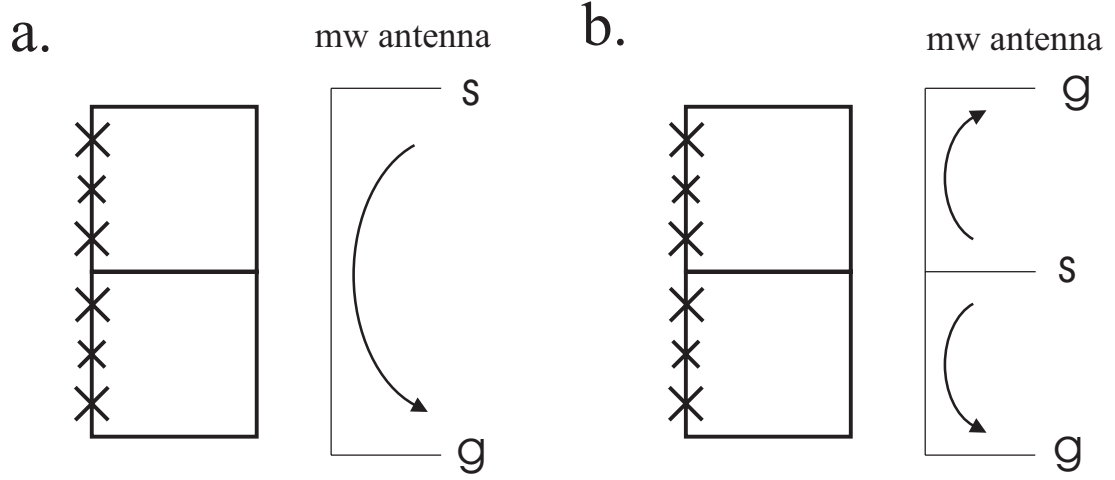


**Figure 3.5:** Two possible configurations for applying microwave radiation to the qubits,  $s$  denotes the signal wire and  $g$  is the ground wire. a) Both qubits receive the same oscillating flux signal. b) The phase of the oscillating flux seen by the qubits is  $\pi$  out of phase.

the unperturbed system according to  $UH_{mw}U^*$ . Here  $U$  is the matrix containing the eigenvectors of the unperturbed Hamiltonian so it satisfies  $UHU^* = I$ . The resulting Hamiltonian including the perturbation term for identical qubits looks like

$$\mathbf{H}_{mw} = \begin{pmatrix} -\frac{\epsilon_{1,mw} + \epsilon_{2,mw}}{2} & 0 & 0 & 0 \\ 0 & -\frac{\epsilon_{1,mw} - \epsilon_{2,mw}}{2} & 0 & 0 \\ 0 & 0 & \frac{\epsilon_{1,mw} - \epsilon_{2,mw}}{2} & 0 \\ 0 & 0 & 0 & \frac{\epsilon_{1,mw} + \epsilon_{2,mw}}{2} \end{pmatrix} \quad (3.24)$$

Here  $\epsilon_{i,mw}$  are the amplitudes of the energy oscillation due to the oscillating flux used to excite the system,  $\epsilon_{i,mw} = 2I_{p,i}\Phi_{i,mw}$  with  $\Phi_{i,mw}$  the oscillating fluxes through qubit 1 and 2 respectively. For the configuration as in figure (3.5a) this means that for identical qubits the terms with  $(\epsilon_{1,mw} - \epsilon_{2,mw})$  will be zero, and for the configuration as in figure (3.5b)  $(\epsilon_{1,mw} + \epsilon_{2,mw})$  will be zero.

### Energy level diagram and transition rates for identical qubits

The energy levels and transition elements can be calculated numerically and are shown for  $J = 1GHz$  and  $\Delta = 2GHz$  in figure (3.6). In the symmetric case the second level is independent of the flux applied to the system. Far away from the degeneracy point at a flux bias of  $\Phi = \frac{\Phi_0}{2}$  the states are the classical states of

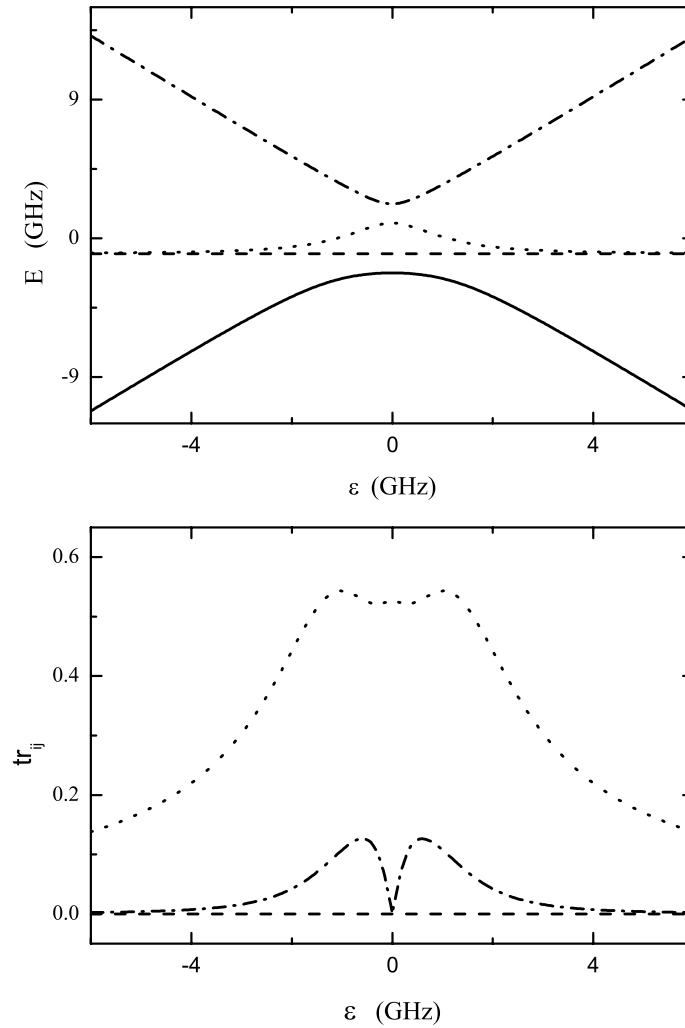


**Figure 3.6:** a) Energy levels for identical qubits. Away from degeneracy the qubits follow the straight lines indicating the energy is given by the sum of the classical qubit energies and the coupling energy  $J$ . For the first and second excited states the qubits are in anti parallel configuration giving an energy advantage of  $2J$  compared to the parallel case. b) Transitions are more likely near the degeneracy point since applied flux radiation will couple in the  $\sigma_x$  direction more efficient there.

the flux qubits, with the second and third state corresponding to superpositions of the  $|\downarrow\uparrow\rangle$  and  $|\uparrow\downarrow\rangle$  states.

When extrapolating the energy difference between the ground state and the second two states it is seen that these lines intersect below zero at the value of  $-2J$ . This represents the energy advantage for the anti parallel configuration of the persistent currents of the qubit as compared to the parallel case. The resonance lines for high frequencies can be used to determine the value of  $J$  from spectroscopy measurements in this way. The transition to the second excited state is easiest (see figure 3.6b) whereas the transition to the first excited state has zero probability for the symmetric microwave configuration. Outside the degeneracy point transitions to the highest level require more microwave amplitude than the others, whereas excitation of the system is in general more easy near the degeneracy point because the applied micro wave flux couples more directly in the  $\sigma_x$  direction, just as in the case of the single qubit.

### Energy level diagram and transition rates for realistic qubits

In any realistic system there will be asymmetries present due to either fabrication uncertainties or introduced on purpose for addressing one qubit at a time. The asymmetries that can occur are differences in critical currents of the junctions and thus in circulating currents ( $I_{p,1}$  and  $I_{p,2}$ ), leading to different slopes of the energy levels, differences in area of the qubits ( $A_1$  and  $A_2$ ), leading to a shift of the qubit levels with respect to each other, and a difference in the tunnel couplings of each qubit ( $\Delta_1$  and  $\Delta_2$ ).

In figure 3.7 the energy levels and transition elements for a system with (a) different persistent currents and (b) different surfaces is shown. For the case where the persistent currents are different the graph clearly shows the energy of the first excited state and the second excited state are no longer independent of the flux, since the fluxes produced will not cancel as in the symmetric case. Since the slopes are different compared to the ground state level, a different  $I_p$  allows for making a distinction between the levels because the resonance peaks will shift differently with flux. Also, the transition elements for going to the first excited state will no longer be zero since the levels are sensitive to flux. In the case of different surfaces the energies are still independent on the applied flux, but the degeneracy is lifted and the resonance lines will be shifted compared to each other.

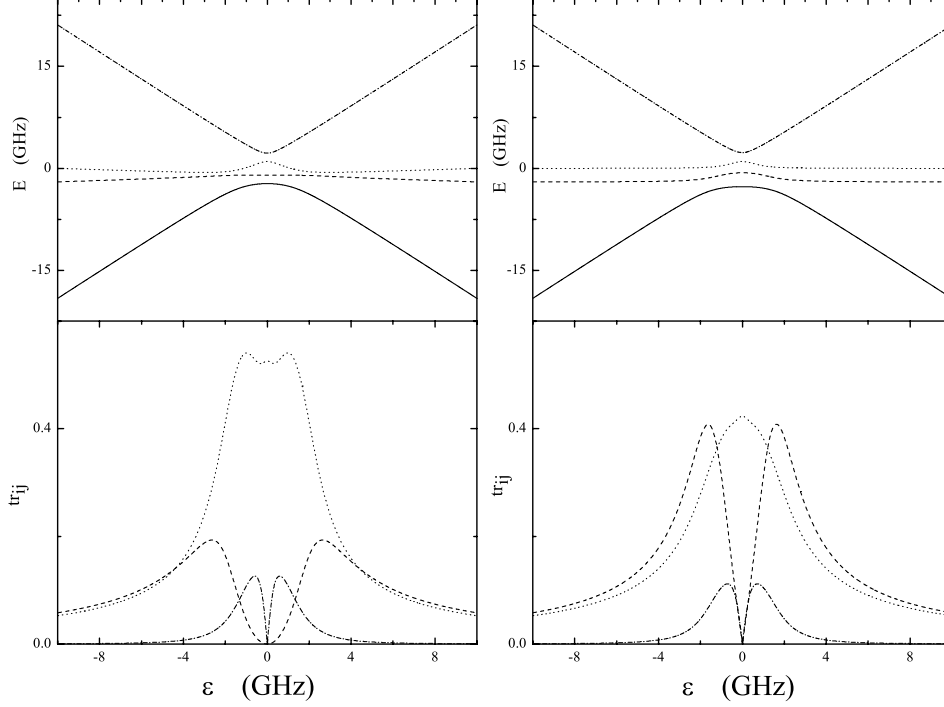


**Figure 3.7:** (a) Qubits with different persistent currents. A different persistent current for each qubit will give non-zero slopes for the first and second excited states. Also the transition element to the first excited state is no longer zero. (b) Qubits with different areas. A different area for a given external magnetic field makes the energy bias of the qubits different, causing the degeneracy of the first and second excited states to be lifted.

### 3.5 Measurements showing the qubit-qubit coupling

Measurements were performed on two coupled-qubit systems with different parameters. In this section first the general measurement principles will be given. Then measurements on a system with mainly geometrical coupling (sample A, see figure 3.8) of  $J = 500\text{MHz}$  will be shown. Since current from both qubits flow in different superconducting layers of their shared line, mainly geometrical coupling was present. Measurements were then performed on a system with coupling via a shared junction (sample B) as is explained in section 3.3.

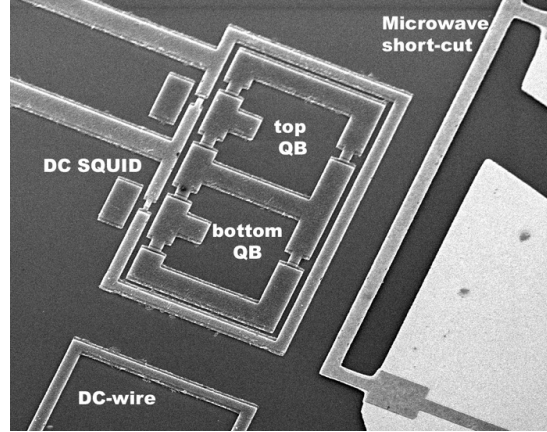


**Figure 3.8:** *Layout for the coupled qubit system of sample A. The two qubits are positioned next to each other so they are coupled via their produced flux. The coupling arising from this configuration is so that the system favours a state in which the qubits are anti parallel compared to the uncoupled case by an energy of  $2J$ .*

### Measurement principles

Measurements are performed by placing the samples inside a cavity at temperature  $T = 20mK$ . Both dc connections and high frequency connections are present for sending current through the squid and applying high frequency microwave radiation to the qubits. The switching probability of the SQUID is determined and the state of the qubit is deduced. Copper powder filters are placed to filter out any high frequency noise ( $> 100MHz$ ) from the current through the squid magnetometer. Switching probability was determined via both slow ramping (10 ms) and via fast pulse measurements (pulses of order  $20ns - 2.5\mu s$  where used). The expected signal for qubits which are only geometrically coupled to the squid changes the switching probability by only a small amount, making it necessary to repeat each measurement many times to obtain enough resolution to determine the state of the qubit.

Typical spectroscopy measurements can be seen in figure 3.9 where the magnetic field is positioned just outside the degeneracy point  $\Phi_{qb} = \frac{1}{2}\Phi_0$  of the qubits where  $E_1 - E_0 = 10.5GHz$  and  $E_2 - E_0 = 11.3GHz$ . Continuous microwave radiation is applied to the system. When the frequency of the radiation is in resonance with the energy distance between the ground state and one of the other levels the system is partially excited and a mixture between  $|\downarrow\downarrow\rangle$  and  $|\downarrow\uparrow\rangle$  at  $f = 10.5GHz$  and between  $|\downarrow\downarrow\rangle$  and  $|\uparrow\downarrow\rangle$  states  $f = 11.3GHz$  is created. Since the circulating current associated with those higher states is different from

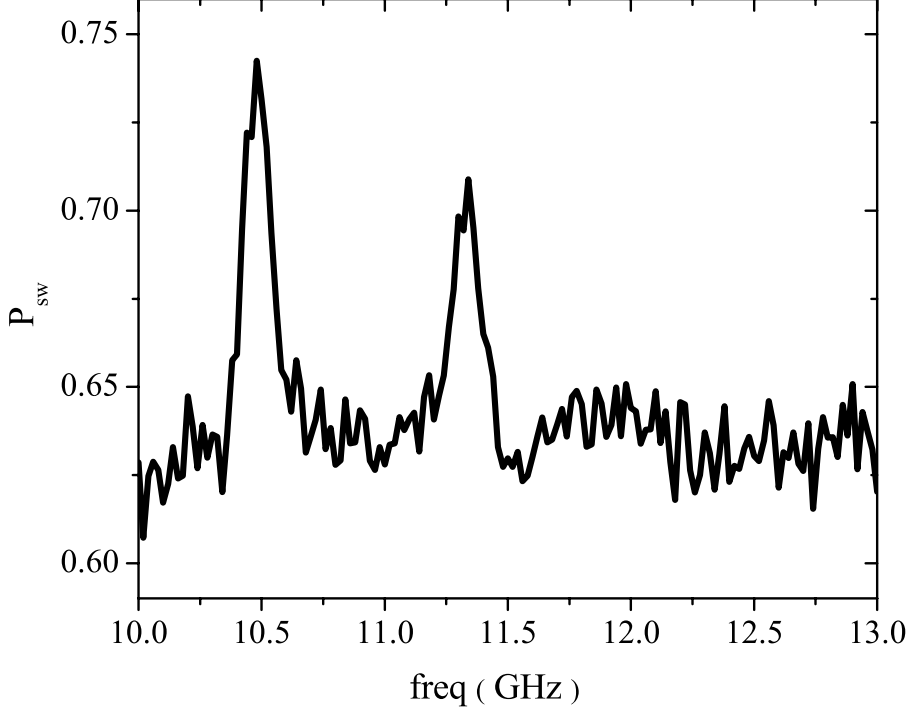


**Figure 3.9:** *Switching probability of the squid measurement device of sample B for various frequencies at a fixed magnetic field around  $\Phi_{qb} = \frac{1}{2}\Phi_0$ . At frequencies where the radiation is resonant with the level splitting of the qubit it is excited to one of the higher states changing the persistent current in the coupled qubit system. In this case this change in produced flux translates to a higher switching probability of the squid.*

the current in the ground state resonances occur as dips or peaks on top of the ground state curve due to a different flux picked up by the SQUID. From the position of the resonance peaks and dips as a function of the applied flux the energy spectrum of the coupled system is determined and from this the parameters as the coupling  $J$  and the tunnel splitting  $\Delta$  can be determined.

### Coupling via the magnetic inductance (sample A)

For sample A (figure 3.8) spectroscopy measurements are performed mapping out the energy spectrum for transitions from the ground state to the first and second excited state as shown in figure 3.10. The spectroscopy points shown are the

observed transitions from the ground to the first and second energy states. The spectroscopy lines for going from the ground to the first and second state are not on top of each other and have a different slope, indicating that the persistent currents in both loops are different by approximately 20 %. The inset shows measurements performed at  $\Phi = \frac{1}{2}\Phi_0$  compared with those performed at a flux bias of  $\Phi = \frac{3}{2}\Phi_0$ . The shift in the lines is due to the difference in qubit areas, which is about 0.03%.

A full fit is used to determine the persistent currents  $I_{p1}$  and  $I_{p2}$ , the qubit-qubit coupling  $J$ , the tunnel splitting  $\Delta_1$  and  $\Delta_2$  and the surface difference  $\sigma$  between the qubits. From the fit it was obtained that the persistent currents where  $I_{p1} = 512nA$  and  $I_{p2} = 392nA$ , the individual tunnel splitting  $\Delta_1 = 0.45GHz$  and  $\Delta_2 = 1.9GHz$  and the difference in surface area  $\sigma = 0.027\%$ . The qubit-qubit coupling is  $J = 0.5GHz$ . The difference in persistent currents of the qubits can be explained by a spread in the junction critical currents. The difference of 10% is understandable but on the high side for the current state of technology in which typical junctions can be made identical to within 5%. The difference in the tunnel splitting is consistent with the difference in Josephson energies of the junctions: The qubit with the higher persistent current has the smaller tunnel coupling.

In these measurements the transition to the highest state  $|\uparrow\uparrow\rangle$  flipping both qubits was not observed. The transition elements coupling the eigenstates of the system with  $\sigma_z$  radiation are shown in figure 3.11. Away from  $\Phi = \frac{1}{2}\Phi_0$ , transition to the  $|\uparrow\downarrow\rangle$  state is most likely, followed by a high probability for a transition to the  $|\downarrow\uparrow\rangle$  state. However, the transition element from the ground to the highest energy state is at least an order of magnitude less, which explains the absence of this resonance in the spectrum. This transition can be forced by applying higher microwave powers, but this has two significant disadvantages. For high powers the switching behaviour of the squid is severely influenced. Also at high power levels the other resonances are extremely broad so all other structure on the measured curves is blurred out.

In summary, we have performed spectroscopy measurements on two coupled flux qubits with mainly geometrical coupling. The mutual inductance between the two qubits leads to a  $\sigma_x\sigma_x$  coupling. The observed resonances agree very well with the two qubit Hamiltonian assuming a coupling of  $J = 500MHz$ .

### Coupling via a large Josephson junction (sample B)

Measurements have been performed on sample B in which coupling is achieved via an extra junction used as a coupling element. A junction with a large enough

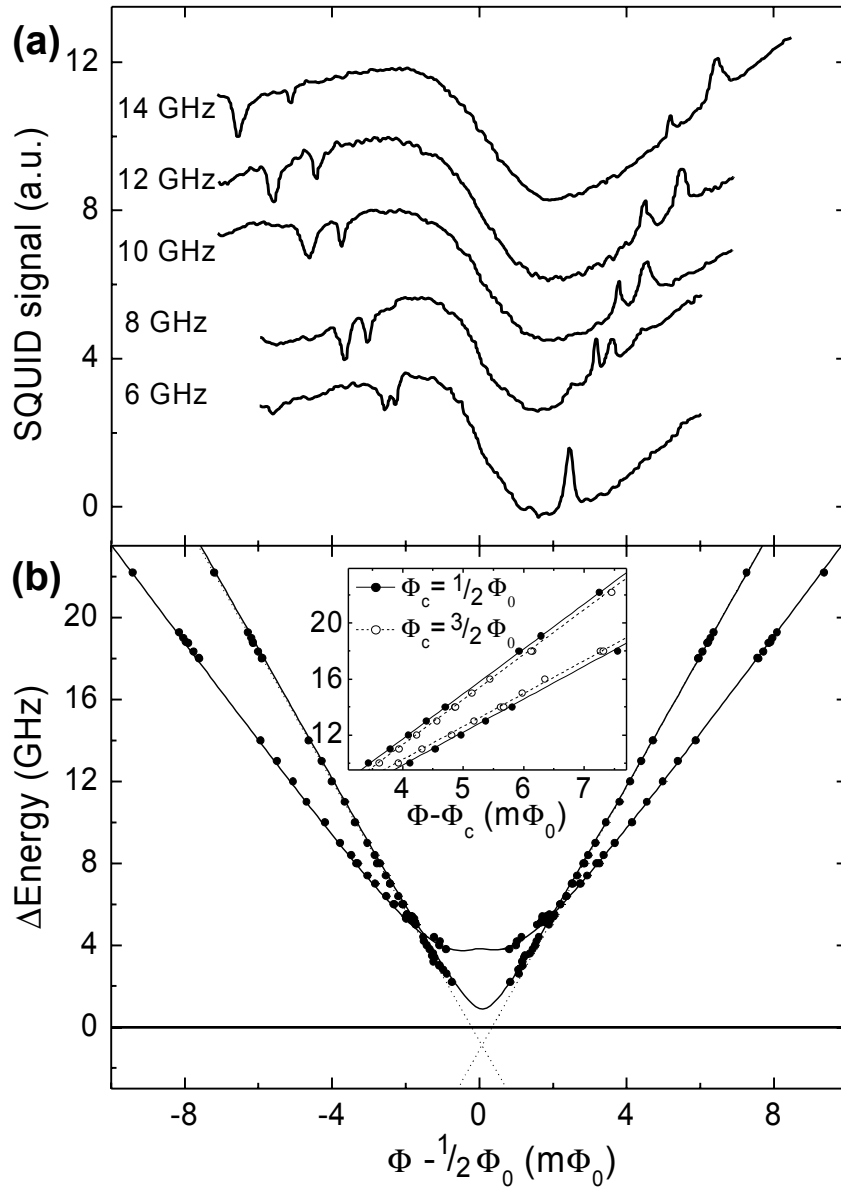


**Figure 3.10:** Energy levels of the inductively coupled qubits of sample A. Clearly visible is the difference in persistent currents of the qubits of  $\pm 10\%$ . The surface difference is estimated to be  $0.0027\%$ . A full fit of the spectroscopy lines showed a coupling of  $500$  MHz.

critical current is fabricated by using the double layers which are present when using shadow evaporation. A key element of this design is the central island and its connections to both the qubits (figure 3.13). The two top junctions are part of one qubit, the two lower junctions are part of the other. The layout is such

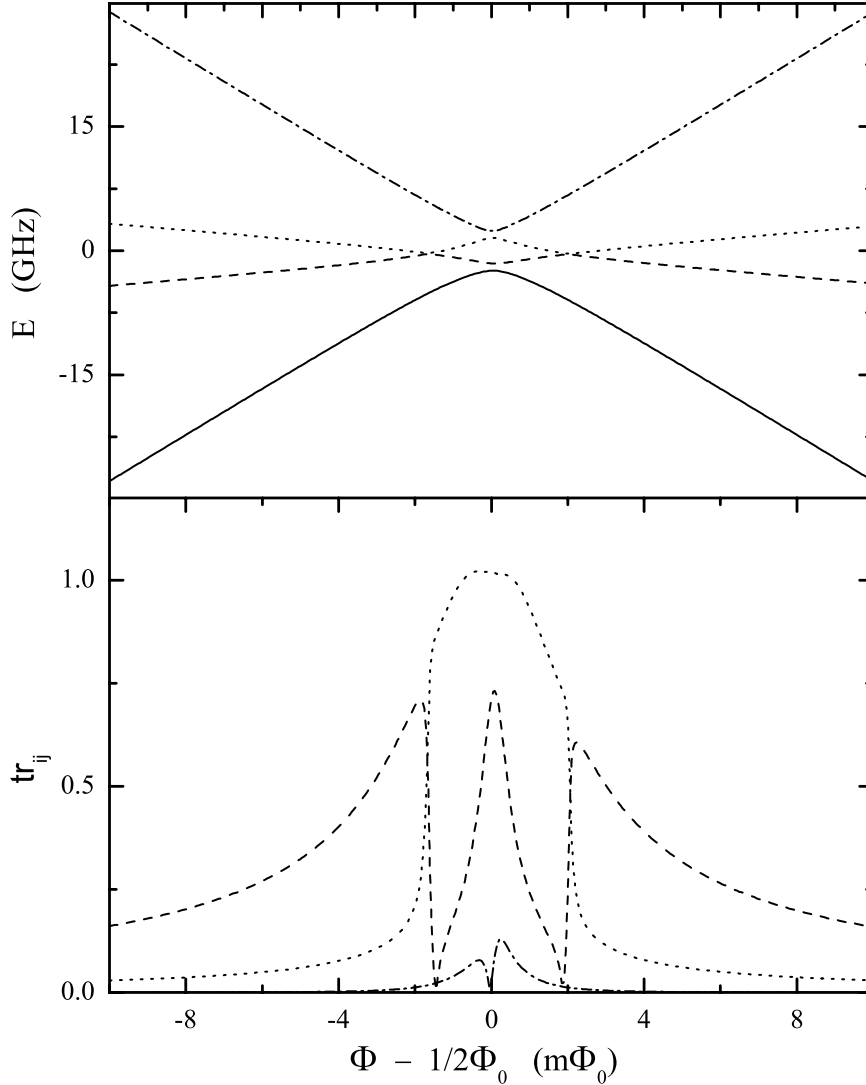


**Figure 3.11:** Energy levels and transition probabilities of the qubits coupled via the mutual inductance as a function of the applied flux (sample A).

that the persistent currents from both qubits are forced to cross from one layer to the other in a well defined part of the circuit. The central island visible in the SEM picture forms the coupling junction. Current leaving the junction of either qubit on the left is forced in the top layer of the central island, whereas the

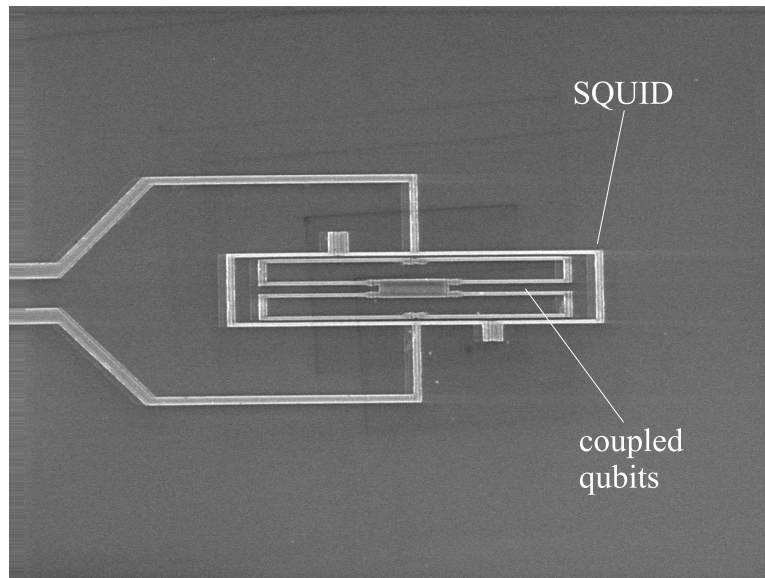


**Figure 3.12:** *Two coupled flux qubits surrounded by a squid (sample B). Key element of this design is the central island and its connections to both the qubits. This is done in such a way that the current will distribute equally in each layer, allowing the island to be described as a single large Josephson junction with a well defined critical current.*

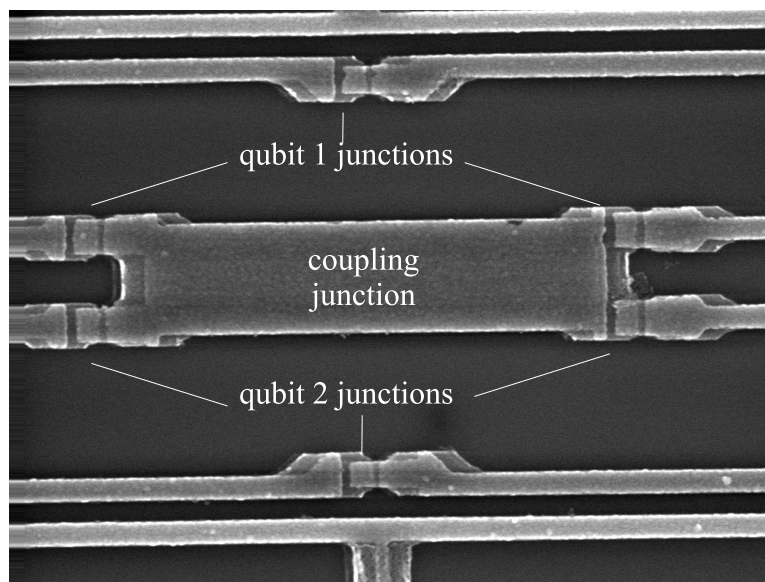


**Figure 3.13:** *Here the way the junction are connected to the central island is clearly visible. Any current extracted from the island on the right side comes from the bottom layer of the island, and any current injected on the left side enters in the top layer of the island (sample B, zoom in of figure 3.12).*

current on the right entering either junction is taken out of the bottom layer (figure 3.13). The island sizes are chosen so that the kinetic inductance in each layer is much smaller than the Josephson inductance of the oxide barrier between the layers. Effectively the central island can then be regarded as a large Josephson junction with a critical current of  $I_{c,cj} = 35\mu A$ , giving a Josephson inductance of  $9pH$ . Spectroscopy measurements performed away from  $\Phi = \frac{1}{2}\Phi_0$  (see figure 3.14) show straight lines each pair associated with the transitions associated with flipping either qubit to the excited state,  $|\downarrow\downarrow\rangle \rightarrow |\downarrow\uparrow\rangle$  and  $|\downarrow\downarrow\rangle \rightarrow |\uparrow\downarrow\rangle$ . The surface difference between the qubits is determined to be  $\Delta A = 0.15\mu m^2$  or 0.4 % of the total surface. The persistent currents are determined from the slopes to be  $I_{p,1} = 260nA \pm 4nA$  and  $I_{p,2} = 275nA \pm 4nA$ . The qubit-qubit coupling is measured from the crossing points of the spectroscopy lines for high frequencies to be  $J = 1.15GHz \pm 0.15GHz$ , in good agreement with the  $J = 1.2GHz \pm 0.1GHz$  calculated from the critical current of the coupling junction, the persistent currents of the qubits, and the estimated geometrical contribution of  $2pH$ .

### 3.6 Conclusions

The origin of the coupling of flux qubits is discussed. The coupling strength is given by  $J = MI_{p1}I_{p2}$  where  $M$ , the mutual inductance, has contributions from geometric, kinetic and Josephson inductances. Although these contributions might have different mechanisms, they all add to the coupling in a similar way. Using spectroscopy measurements to map out the level diagram of a coupled system it is shown that Josephson persistent current qubits can be coupled via their flux degree of freedom.

In sample A mainly geometrical coupling is achieved giving a coupling of  $J = 500MHz$ . In order to increase the coupling and to make it more controllable in the fabrication process a shared junction was used as a coupling element in sample B. Coupling in this way is achieved by making use of the double layer structure one always has with shadow evaporation. Measurements on sample B show a coupling of  $J = 1.15GHz$  which is in good agreement with the calculated value. The measurements presented show that two coupled qubits can be well described by the four dimensional two-qubit Hamiltonian obtained by approximating the Josephson persistent current qubit as a two level system.

It is also shown that coupling in such system can be designed flexible within the wanted range via a large shared junction between the qubits. This allows for great flexibility in designing systems in which coupling via the phase degree of

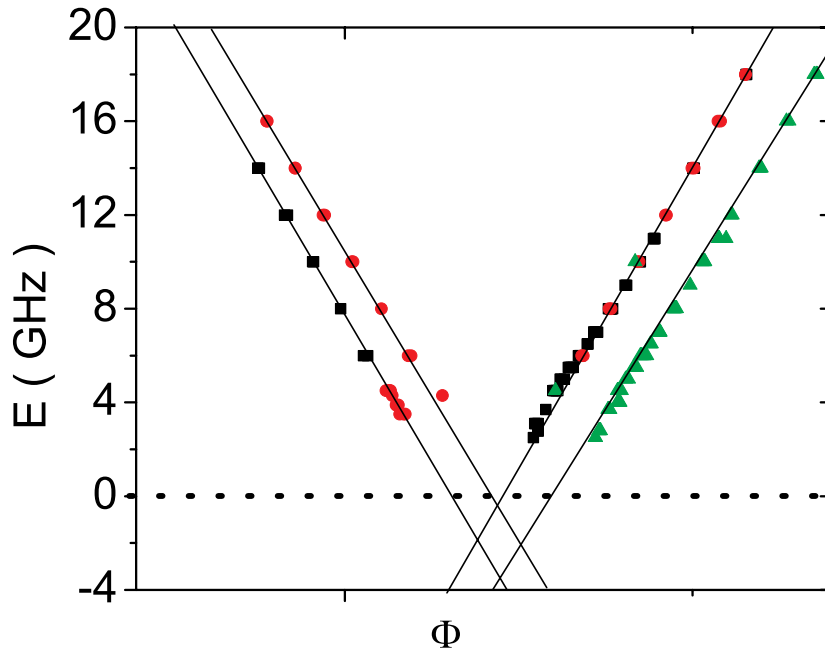


**Figure 3.14:** *High-bias spectroscopy measurements show the lines intersect on average at approximately  $f = -2.2\text{GHz}$  indicating a qubit qubit coupling of  $J = 1.1\text{GHz}$ . The lines do not fall on top of each other due to an asymmetry in the qubit surface and thus in the flux bias of the qubits.*

freedom is needed. Also, since the coupling is mainly via the phase over this large junction the actual flux signal can be smaller which is convenient for minimizing cross talk between Josephson persistent current qubits when many systems have to be placed near each other.

## References

- [1] Yu. A. Pashkin, T. Yamamoto, O. Astafiev, Y. Nakamura, D.V. Averin, J. S. Tsai, "Quantum oscillations in two coupled charge qubits", *Nature* **421**, 823 (2003).
- [2] T. Yamamoto, Yu. A. Pashkin, O. Astafiev, Y. Nakamura, J. S. Tsai, "Demonstration of conditional gate operation using superconducting charge qubits", *Nature* **425**, 941 (2003).

- [3] A. Izmalkov, M. Grajcar, E. Ilichev, Th. Wagner, H.-G. Meyer, A. Yu. Smirnov, M. H. S. Amin, Alec Maassen van den Brink, and A.M. Zagoskin, "Evidence for Entangled States of Two Coupled Flux Qubits", *Phys. Rev. Let* **93** (2004).
- [4] J. B. Majer, F.G. Paauw, A.C.J. ter Haar, C.J.P.M. Harmans, J.E. Mooij, "Spectroscopy on two coupled superconducting flux qubits", cond-mat/0308192.
- [5] B.L.T. Plourde, J. Zhang, K.B. Whaley, F.K. Wilhelm, T.L. Robertson, T. Hime, S. Linzen, P.A. Reichardt, C.E. Wu and John Clacke, "Entangling flux qubits with a bipolar dynamic inductance" (2004).
- [6] David J. Griffiths, "Introduction to electrodynamics" (1989).
- [7] T. Orlando and Delin, "Foundations of Applied Superconductivity", Addison-Wesley publishing company (1991).
- [8] M. Tinkham, "Introduction to Superconductivity" (1975).
- [9] R. Meservey and P.M. Tedrow, "Measurements of the Kinetic Inductance of Superconducting Linear Structures", *Journal of Applied Physics* **40**, 5 (1969).
- [10] J. B. Majer, "Superconducting Quantum Circuits", PhD Thesis, TU Delft, (2002).
- [11] M.J. Storcz, and F. K. Wilhelm, "Decoherence and gate performance of coupled solid-state qubits", *Phys. Rev. A.* **67**, 042319 (2003)

## Chapter 4

# Coherent manipulation of two coupled Josephson Persistent Current Qubits

Spectroscopy measurements from the ground state as well as from the partially populated first excited state reveal the energy level structure of two coupled Josephson persistent current qubits. Coherent Rabi oscillations in a coupled qubit system have been observed. Conditional spectroscopy is performed by using a  $\pi$ -pulse to flip one of the qubits followed by a microwave burst to incoherently pump the system from this excited state to a higher state.

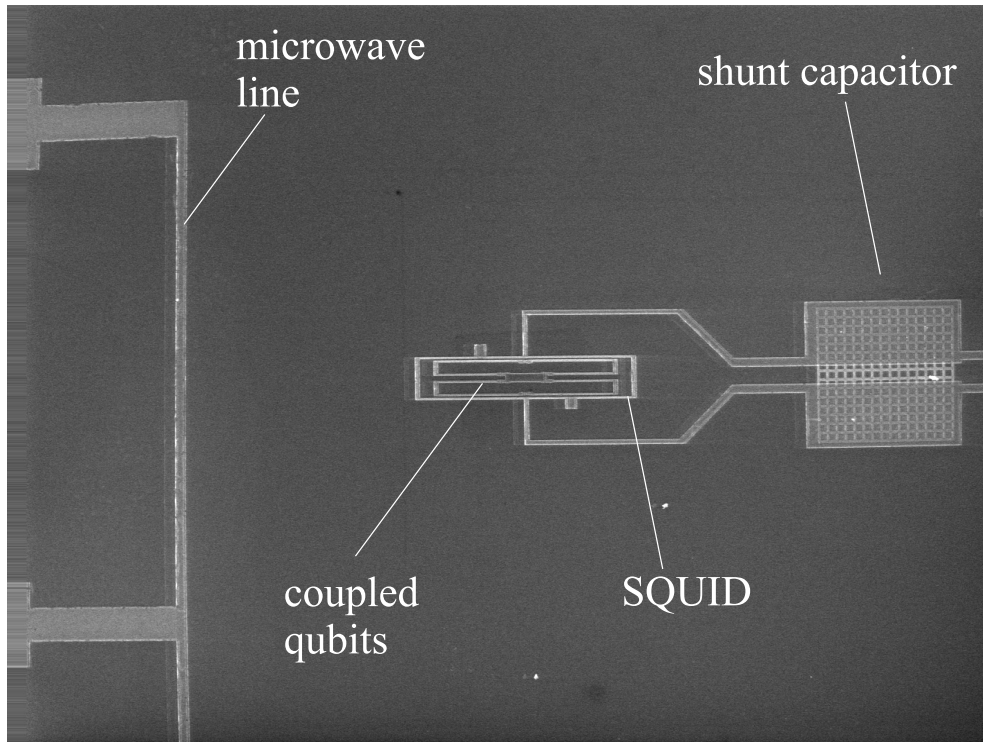


**Figure 4.1:** *Coupled qubits sharing a large junction to achieve a coupling of  $J = 1.15\text{GHz}$ . On the left the microwave line is visible used for exciting the system by applying a high frequency microwave signal. The SQUID is shunted with a capacitor visible on the right.*

## 4.1 Introduction

Coherent operations have been performed in coupled superconducting charge qubits [1, 2] as well as in a single Josephson persistent current qubit coupled to an oscillator [3]. Also coupling of superconducting flux qubits has been achieved [4, 5]. In order to create entangled states in qubits and demonstrate two-qubit operations for investigating the principles of quantum computation, complete knowledge of the energy spectrum of these systems is needed. One should then be able to coherently move the state of the system through the four dimensional Hilbert space.

In this chapter measurements on two coupled Josephson persistent current qubits (figure 4.1) are shown. Spectroscopy measurements have been performed on a coupled qubit system showing not only transitions starting from the ground state, but also excitations from the first excited state to higher states. This reveals the two qubit energy level structure (section 4.2).

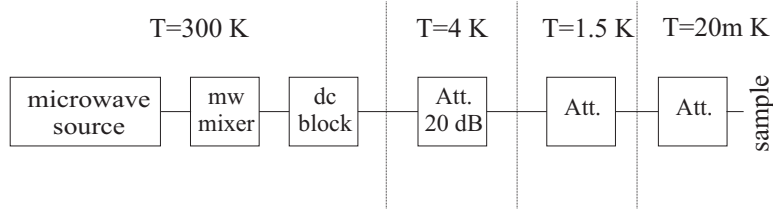


**Figure 4.2:** Attenuation of the microwave signals is present at various temperature stages to reduce thermal noise from higher temperatures.

Transitions from the first excited state to higher states were visible in continuous-wave spectroscopy due to a noise induced non-zero population of the first excited state. This unwanted population of the higher states was reduced by additional attenuation of the noise from high temperatures. In section 4.3 coherent oscillations flipping each individual qubit of the coupled qubit system are presented and possible decoherence mechanisms will be discussed.

Finally conditional spectroscopy measurements exciting higher lying transitions after applying an  $n\pi$ -pulse to go coherently from the ground state to the first excited state have been performed (section 4.4).

## 4.2 Transitions from the ground state and the partially populated first excited state

In the coupled qubit system discussed in section 3.5 a relatively large qubit-qubit coupling  $J$  is achieved by using a large Josephson junction as a coupling element. Spectroscopy measurements were performed on this system to determine the position of the energy levels as a function of the external applied flux. Spectroscopy measurements show a qubit-qubit coupling of  $J = 1.15GHz$  (see chapter 3).

Measurement wires and microwave lines going from room temperature at  $T \sim 300K$  down to the mixing chamber temperature  $T \sim 20mK$  are filtered using copper powder filters and microwave attenuators (see figure 4.2) at various stages to filter out noise from higher temperatures. Without attenuation at the mixing chamber stage ( $20mK$ ), resonances from the first excited state to higher states were also observed. The measured spectrum is shown in the lower part of figure 4.3 by the solid dots, together with the fitted energy level diagram of this system. The transitions from the ground state to the first, second and third excited state are indicated with the solid black line. The dotted lines indicate the transitions from the first excited state to the second and third excited states, and from the

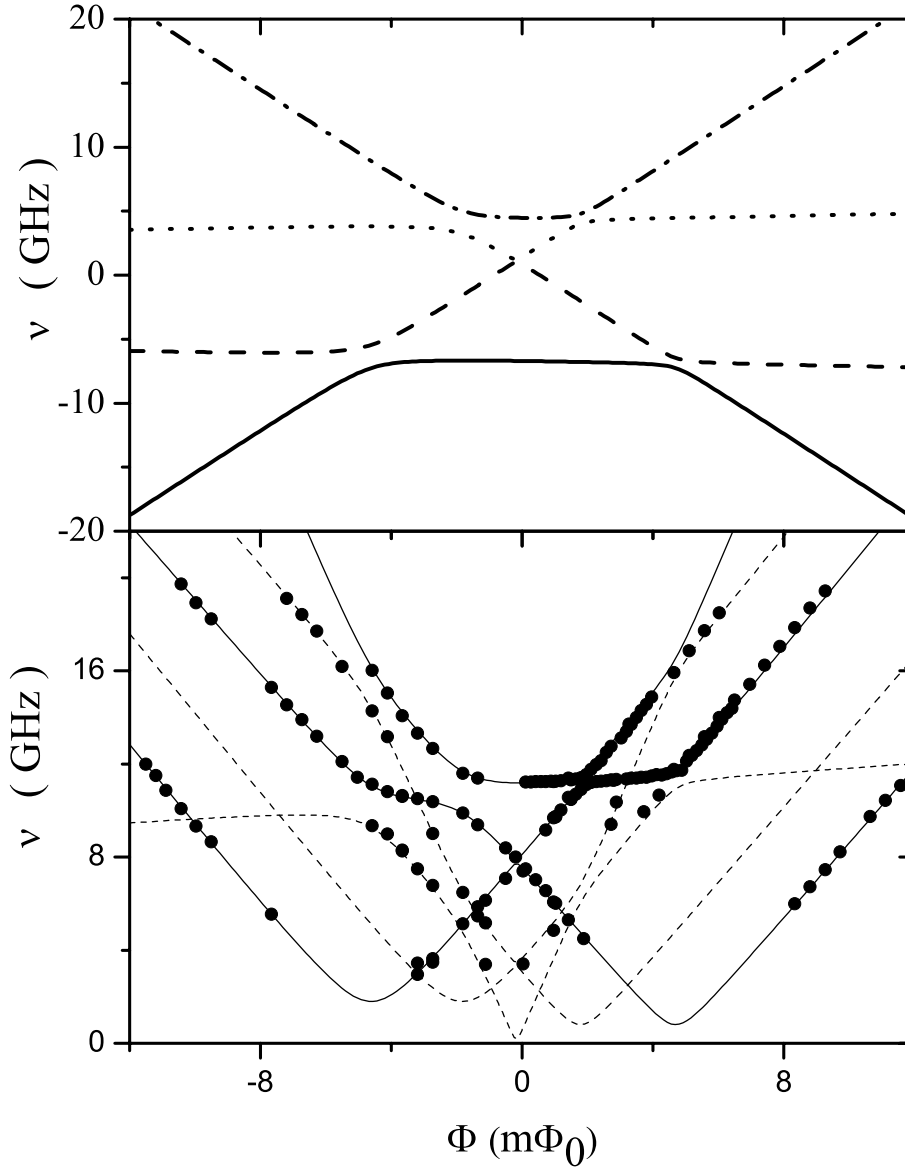


**Figure 4.3:** Energy spectrum (top) of the two qubit system. The dots (bottom) are measured transitions. The calculated transitions from the ground state to the higher states (solid line) and from the first excited state to the higher states (dashed line) are in good agreement with the measurements. The energies and energy differences are plotted with  $I_{p,1} = 260nA$  and  $I_{p,2} = 275nA$ , the qubit-qubit coupling  $J = 1.15GHz$ , and tunnel splitting  $\Delta_1 = 1.7GHz$  and  $\Delta_2 = 0.8GHz$ . The difference in area is  $\Delta S = 0.004S_{average}$

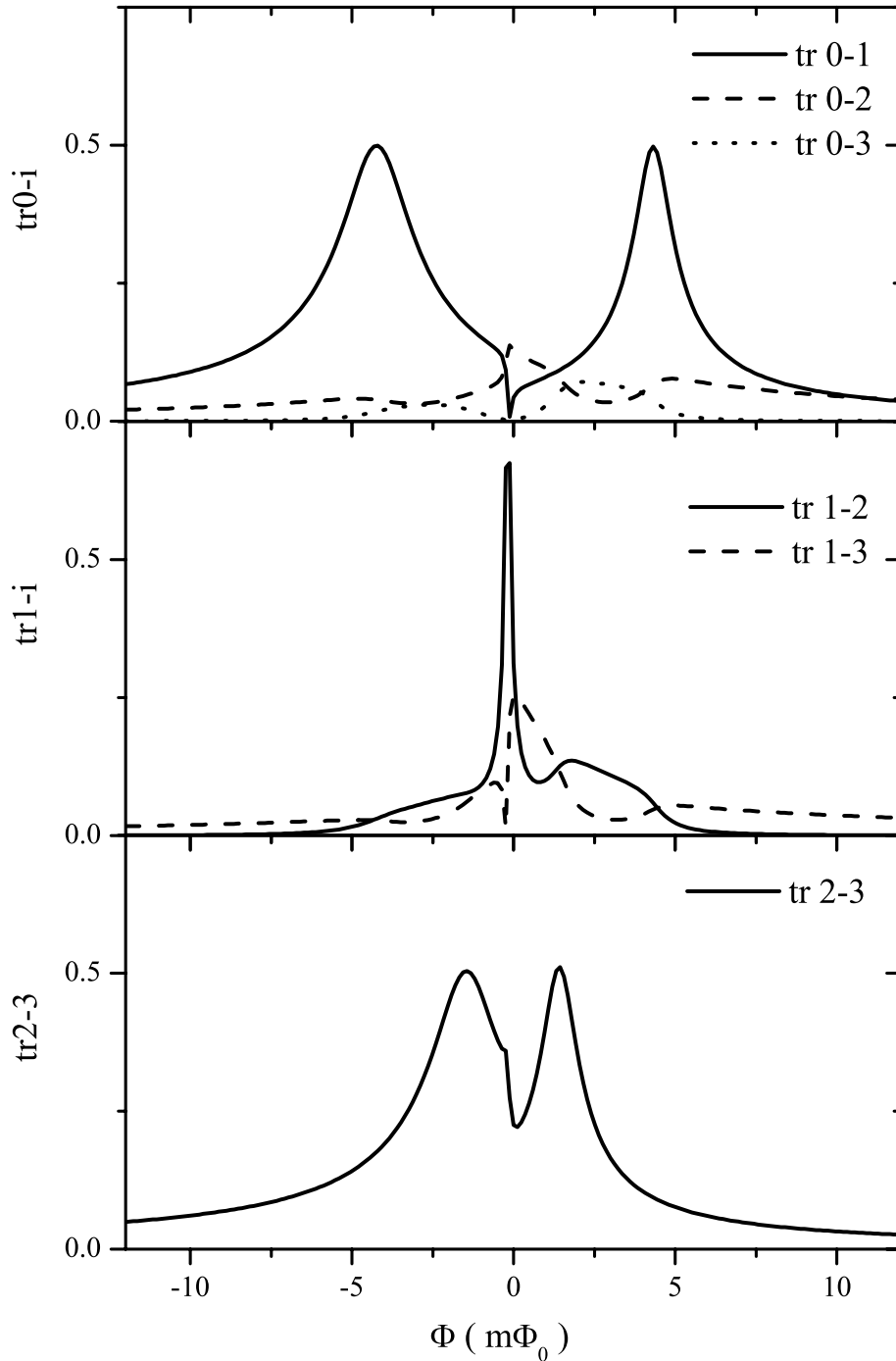


**Figure 4.4:** Calculated transition elements for excitations from the ground state to the higher states, from the first excited state to the higher states, and from the second excited state to the highest state. Parameters used here are the fitting parameters of figure 4.3

second excited state to the third excited state. Observation of transitions from a higher state implies that the system did not fully cool down to its ground state, as would be expected from the substrate temperature of  $T = 20mK$ . The higher effective temperature is attributed to the presence of the microwave line used for applying high frequency radiation to the qubits. The theoretical level diagram shown in the top part of figure 4.3 is obtained with  $I_{p1} = 260nA$ ,  $I_{p2} = 275nA$ ,  $\Delta_1 = 1.7GHz$  and  $\Delta_2 = 0.8GHz$ . The difference in area is  $\Delta S = 0.004S_{average}$ .

In the spectroscopy data the anti-crossing of  $2GHz$  between the second and the third excited state is clearly visible at  $\Phi = -3m\Phi_0$ . The smaller anti-crossing of  $250MHz$  between those levels is observed at  $\Phi = +2m\Phi_0$ . The difference in the anti-crossings is caused by the difference in tunnel splitting of the individual qubits.

### Effective temperature for a system coupled to more than one bath

Transitions from the first excited state to the higher states are observed in this coupled qubit system as shown in figure 4.3. This means that, in the absence of microwave excitation, there is a non-zero population of this first excited state. The additional excitations are attributed to the presence of the microwave line increasing the effective noise temperature. The temperature of the environment seen via the squid is  $T = 20mK$  since filtering suppresses high frequency noise from higher temperatures. However, the environment seen via the microwave line is at  $T = 1.5K$  since, for the measurements of figure 4.3, no attenuation was present at a lower temperature stage of the cryostat. Both environments cause transitions via emission  $\Gamma_{\downarrow}$  and absorption  $\Gamma_{\uparrow}$  of energy which both contribute to the final effective population of the two levels (figure 4.5).

With the population of the ground state  $|0\rangle$  and the first excited state  $|1\rangle$  denoted as  $p_0$  and  $p_1$ , the rate of change in population of the states for a system coupled to a single environment can be obtained from the balance equations

$$\dot{p}_1 = p_0\Gamma_{\uparrow} - p_1\Gamma_{\downarrow} \tag{4.1}$$

$$\dot{p}_0 = p_1\Gamma_{\downarrow} - p_0\Gamma_{\uparrow} \tag{4.2}$$

The steady state where  $\dot{p}_1 = 0$  and  $\dot{p}_0 = 0$  should satisfy the Boltzmann distribution

$$\frac{p_1}{p_0} = \frac{\Gamma_{\downarrow}}{\Gamma_{\uparrow}} = e^{-\Delta E/k_B T} \tag{4.3}$$

where  $\Delta E = E_1 - E_0$  is the energy difference between the levels,  $T$  is the temperature of the bath, and  $p_0 + p_1 = 1$ . The populations of the  $|0\rangle$  state and the

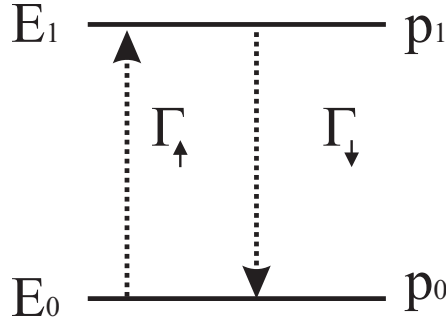


**Figure 4.5:** For a two level system coupled to a bath at a finite temperature the population  $p_0$  and  $p_1$  of the ground and the excited state are determined via a detailed balance of the excitation  $\Gamma_{\uparrow}$  and emission rates  $\Gamma_{\downarrow}$  indicating the system can loose or gain energy from the environment. In the case of coupling to more then one environment at different temperatures the rate equations are more complicated and it is no longer possible to assign a single temperature to the system.

$|1\rangle$  state are

$$p_0 = \frac{1}{1 + e^{-\Delta E/k_B T}} \quad (4.4)$$

$$p_1 = \frac{e^{-\Delta E/k_B T}}{1 + e^{-\Delta E/k_B T}} \quad (4.5)$$

The population of the levels in a two level system coupled to two separate baths at different temperatures can again be described by looking at the population balance. The two baths are associated with the SQUID at  $T_{sq}$  and with the microwave line at  $T_{mw}$ . Absorption from and emission to both baths is possible, yielding

$$\dot{p}_1 = p_0 [\Gamma_{\uparrow, sq} + \Gamma_{\uparrow, mw}] - p_1 [\Gamma_{\downarrow, sq} + \Gamma_{\downarrow, mw}] \quad (4.6)$$

$$\dot{p}_0 = p_1 [\Gamma_{\downarrow, sq} + \Gamma_{\downarrow, mw}] - p_0 [\Gamma_{\uparrow, sq} + \Gamma_{\uparrow, mw}] \quad (4.7)$$

The equilibrium condition is then

$$\frac{p_1}{p_0} = \frac{\Gamma_{\downarrow, sq} + \Gamma_{\downarrow, mw}}{\Gamma_{\uparrow, sq} + \Gamma_{\uparrow, mw}} \quad (4.8)$$

The absorption and emission rates are directly related to the bath to which the system is coupled. For each individual bath the rates follow the Boltzmann distribution  $\frac{\Gamma_{\downarrow, sq}}{\Gamma_{\uparrow, sq}} = e^{-\Delta E/k_B T_{sq}}$  and  $\frac{\Gamma_{\downarrow, mw}}{\Gamma_{\uparrow, mw}} = e^{-\Delta E/k_B T_{mw}}$ . The equilibrium population is now

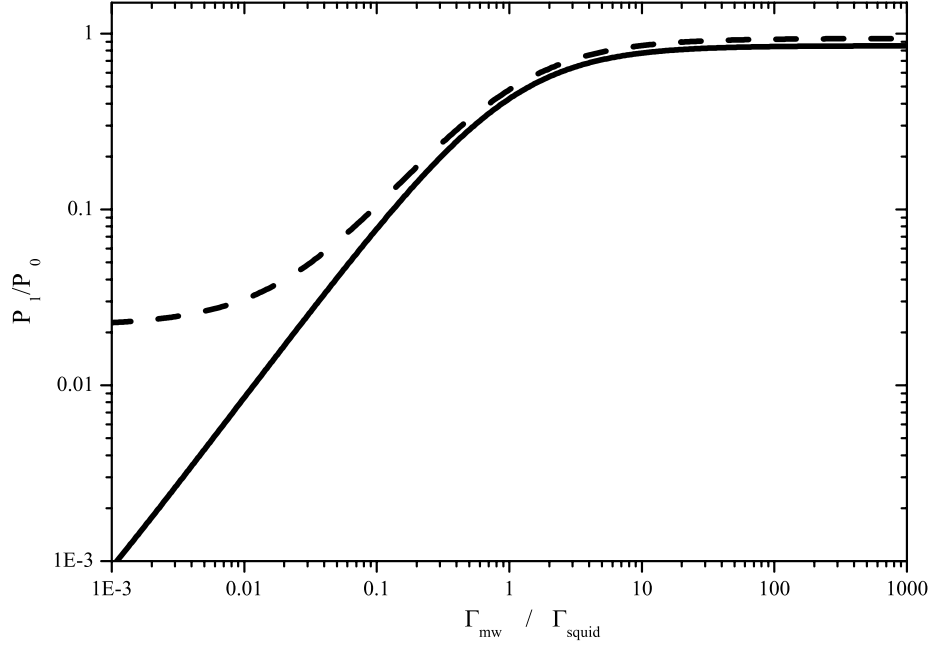


**Figure 4.6:** Population of the excited state in a two level system coupled to two environmental baths, the squid environment being at  $T_{sq} = 25mK$  and the microwave environment at  $T_{mw} = 1.5K$ . The levelsplitting of the quantum system are 2GHz and 5GHz.

$$\frac{p_1}{p_0} = \frac{\Gamma_{\uparrow,sq} e^{-\Delta E/k_B T_{sq}} + \Gamma_{\uparrow,mw} e^{-\Delta E/k_B T_{mw}}}{\Gamma_{\uparrow,sq} + \Gamma_{\uparrow,mw}} \quad (4.9)$$

The population of the excited state in a two state system versus the ratio of the relaxation rates due to the squid (at  $T_{sq} = 25mK$ ) and the microwave line (at  $T_{mw} = 1.5K$ ) is plotted in figure 4.6 for energy differences of 2GHz and 5GHz. Note that one cannot simply define a new effective temperature of the system since depending on the level splitting  $\Delta E$  of the system the relaxation rates are weighted differently. Detailed knowledge of these rates is needed to determine the population [6].

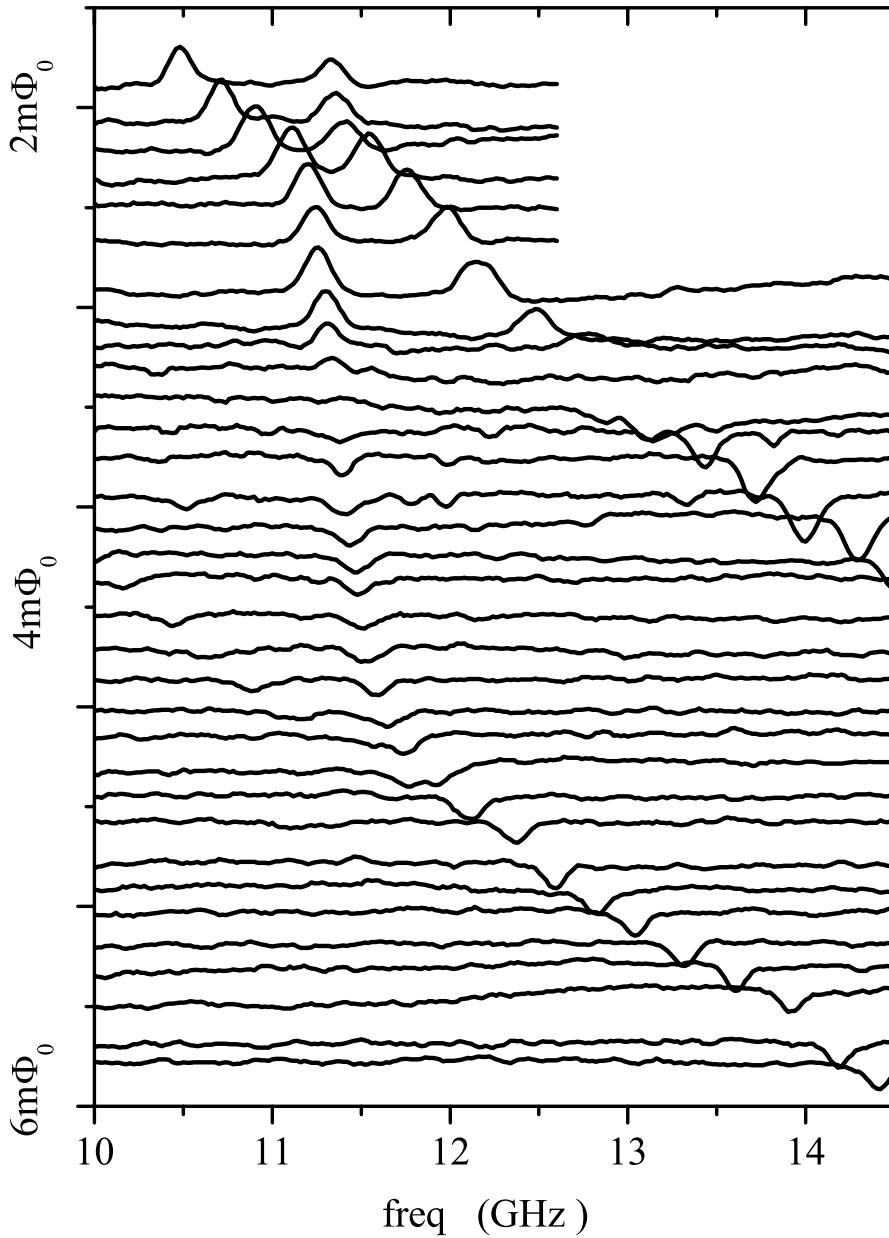


**Figure 4.7:** Spectroscopy measurements showing transitions from the ground to the second and third excited state. Moving the flux in this region changes the character of the observed resonances from a positive signal ("peak") to a negative signal ("dip") as can be seen in these traces. For the observed peaks actually a dip would be expected. This is caused by the fact that the system there relaxes to the second excited state which has a long relaxation time, changing the character of the observed transition.

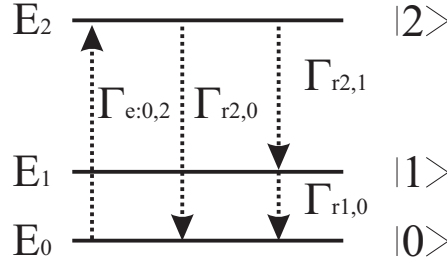


**Figure 4.8:** After excitation of the system to the  $|2\rangle$  state the system can relax to the ground state  $|0\rangle$  directly or via the intermediate energy state  $|1\rangle$ . Depending on the ratio of the relaxation rates a different mixture is obtained when the system is pumped to the second excited state and thus the measured signal strongly depends on this.

### Relaxation via intermediate levels

In figure 4.7 spectroscopy measurements around right the anti-crossing point between the second and third level of the energy spectrum of figure 4.3 are plotted. The anti crossing with a distance of  $250MHz$  is clearly visible in the top of the figure. One observes that, following the two resonance features with increasing flux bias, the character of the resonances change from positive ("peak") to negative ("dip"). However, the slope  $\frac{\partial E}{\partial \Phi}$  of the level as a function of flux does not change. Since the direction of the current is determined by this slope of the energy level with respect to flux according to  $(I_{p1} + I_{p2}) = -\frac{\partial E}{\partial \Phi}$ , the character of the resonance feature should not change. This change in measured signal is caused by a difference in relaxation times for the transitions between the different levels. After excitation of the system to state  $|2\rangle$  using microwaves (figure 4.8) the system very quickly relaxes to state  $|1\rangle$ . Measurement of the signal is performed some  $50ns$  after excitation, so if  $\Gamma_{r2,1}^{-1} \ll 50ns$  the system is then in the first excited state and the measured signal is the signal associated with that state, which is opposite in sign. In the region where this effect is observed the transition element for applied  $\sigma_z$  flux, coupling the second excited state to the first excited state is large, as shown in figure 4.4. In this region around  $\Phi \approx 3m\Phi_0$  the  $|2\rangle$  to  $|1\rangle$  transition element (middle panel) is larger then the  $|2\rangle$  to  $|0\rangle$  element (top panel), making the relaxation rate  $\Gamma_{\downarrow 2,1}$  higher then  $\Gamma_{\downarrow 2,0}$ . Similarly, the  $|3\rangle$  to  $|2\rangle$  element (bottom graph) is larger then the  $|3\rangle$  to  $|1\rangle$  and  $|3\rangle$  to  $|0\rangle$  elements, which makes the system, after it is excited, relax to the second excited state.

In this way, the  $|2\rangle$  level is used to populate the  $|1\rangle$  state using continuous wave radiation, and depopulate the ground state, and similar for the third excited state. The result is a measured signal which belongs to the first excited energy state. The exact sign of the signal depends strongly on the details of the

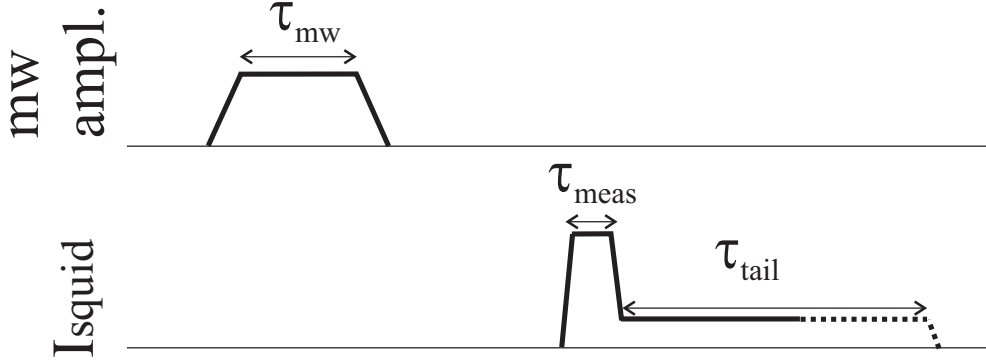


**Figure 4.9:** Timing scheme for applying microwaves and the measurement pulse to the system. First a microwave pulse of a specific duration  $\tau_{mw}$  is applied to the coupled qubit system. When the frequency of the applied microwave is resonant with the energy difference between the levels of the system, the system performs Rabi-oscillations. After the microwave pulse the state of the coupled qubit system is read-out by measuring the switching probability of the SQUID.

incoherent mixture that is created by this process. These relaxation rates cannot be independently measured so no quantitative comparison can be made.

### 4.3 Coherent transitions from the ground state to higher states.

The minimum observed peak width was  $70MHz$  indicating a short dephasing time of  $\tau_\phi \sim 5ns$ . For large microwave powers applied to the qubit system coherent oscillations between the ground state and the first and second excited state have been observed as a function of the applied pulse length. The pulse scheme is schematically shown in figure 4.9. First the microwave radiation is switched on for a duration  $\tau_{mw}$  which is varied between  $1ns$  and  $\sim 100ns$  by mixing the signal from a CW microwave source with a dc pulse of the desired duration, see figure 4.10.

At resonance the double qubit system is oscillating between the two states. The measured oscillations shown in figure 4.11 disappear after a pulse length  $\tau_{mw} \approx 75ns$ . Rabi oscillation were observed at various values of the flux bias, but only for specific values of the bias decay times of up to  $\tau_{mw} \approx 75ns$  were observed. After the microwave pulse, the bias current through the squid is switched on to perform the state detection measurement. Depending on the flux state of the qubit after the microwave pulse the switching probability of the squid is increased

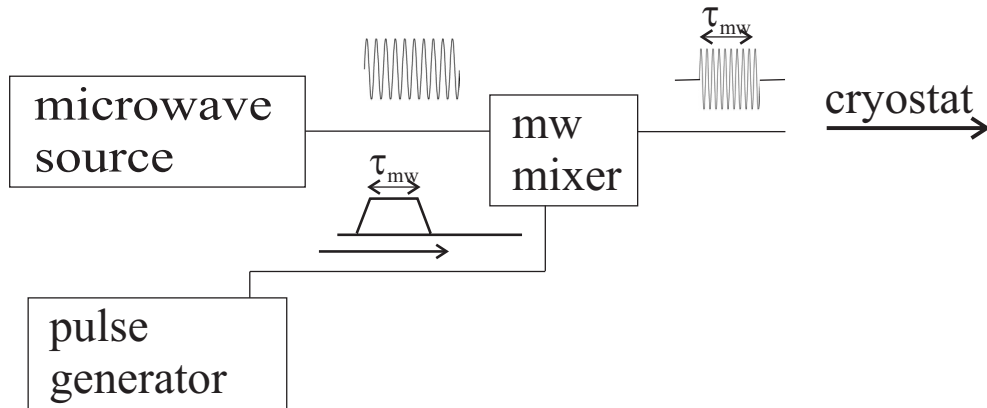


**Figure 4.10:** Continuous microwave radiation is mixed with a dc pulse to create microwave pulses of the desired duration.

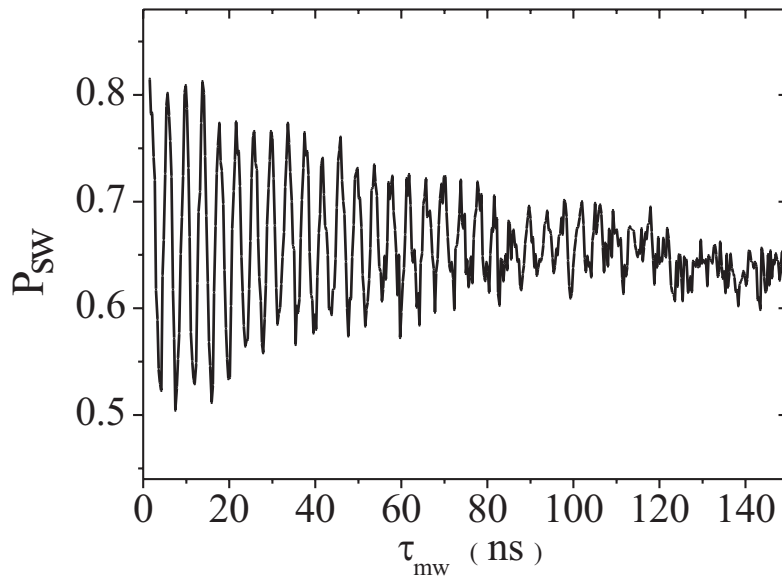


**Figure 4.11:** SQUID switching probability changes due to a changing persistent current in the qubit, which performs coherent oscillations between the ground state  $|0\rangle$  and the first excited state  $|1\rangle$  at a level spacing of  $f = 8.3\text{GHz}$ . The oscillation period is  $\sim 6\text{ns}$ .

or decreased. In figure 4.12 oscillations between the ground state  $|0\rangle$  and the first excited state  $|1\rangle$  are visible for various microwave powers. The frequencies of the fitted oscillations are plotted in 4.13 and show the expected linear behaviour for the low amplitudes of the applied microwaves. For higher driving powers the mixers making the microwave pulse enter the regime where they no longer behave linearly, making it in the specific setup used not possible to verify the frequency versus power relation over a larger range.

### Ramsey interference.

It is observed that for high driving powers coherent oscillations are visible for pulse lengths  $\tau_{mw}$  of up to 70ns. For more complicated pulse schemes, it is important that the phase of the system is conserved over a longer time even without driving. To determine the free decay time of the phase of the system Ramsey interference measurements were performed. Two consecutive  $\pi/2$  pulses are applied to the qubit system (figure 4.14) and the time between the pulses is varied. The first pulse brings the state of the system in a superposition of the ground state and the excited state. Depending on the detuning and the waiting time the second pulse either continues rotation of the system towards the excited state, or rotates the system back to the ground state creating an interference pattern, seen in figure 4.15 at a resonance of 8GHz and a detuning of 200MHz. The interference pattern disappears after only  $\sim 7$ ns indicating a short free decay time for the phase of the system.

### Source of decoherence.

From figure 4.12 we see that the Rabi oscillations are visible up to a microwave pulse length of typically  $\tau_{mw} \approx 50$ ns. During the experiment we experienced low frequency flux jumps on a time scale of  $\sim 5$  minutes causing jumps in peak positions of the order of  $75$ MHz from trace to trace (see figure 4.16). The influence of these flux jumps is strongly reduced in a region where the derivative of the energy difference between the levels  $\Delta E$  to the external flux is zero,  $\frac{\partial \Delta E}{\partial \Phi_{ext}} = 0$ , as indicated in the inset of figure 4.16. This reduction indicates that correlated flux jumps offset the flux bias of our qubits.

These slow flux jumps limit the ability to perform coherent operations since each measured point takes about 1 to 10 seconds and to obtain a trace like in figure 4.17 takes about 10 minutes. One can see that the system oscillates around some equilibrium SQUID switching probability. When the measurement has arrived at pulse lengths of  $\tau_{mw} = 75$ ns this equilibrium value changes indicating the effective flux bias of the system has changed. This change corresponds to a flux

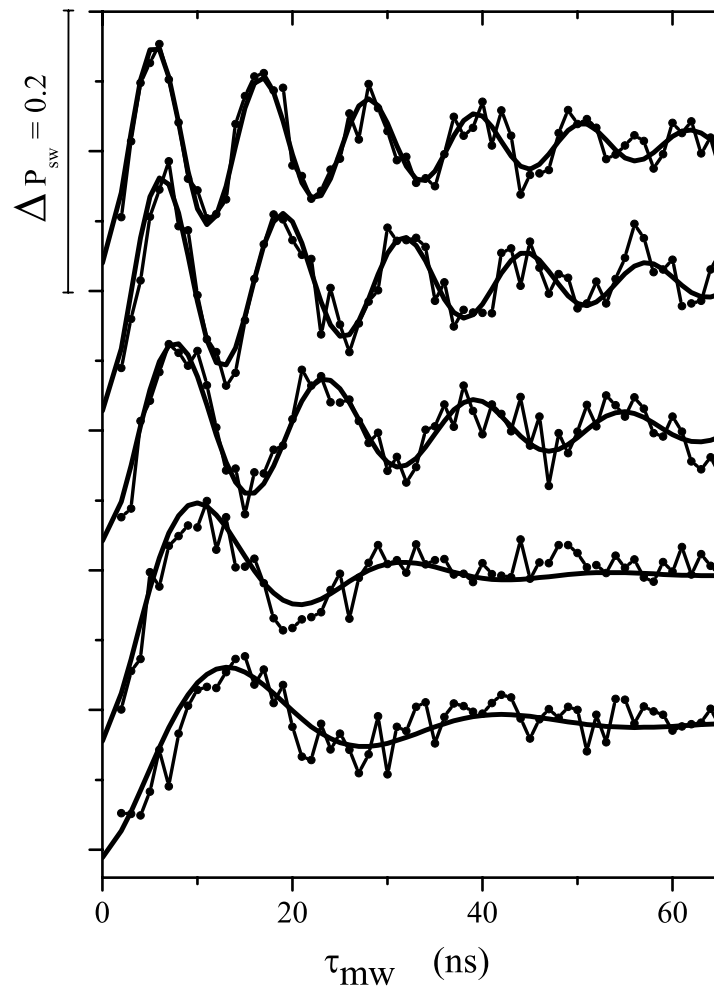


**Figure 4.12:** Coherent oscillations between the ground state  $|0\rangle$  and the first excited state  $|1\rangle$  for various driving powers, each trace is 3dB less in power, going from top to bottom.

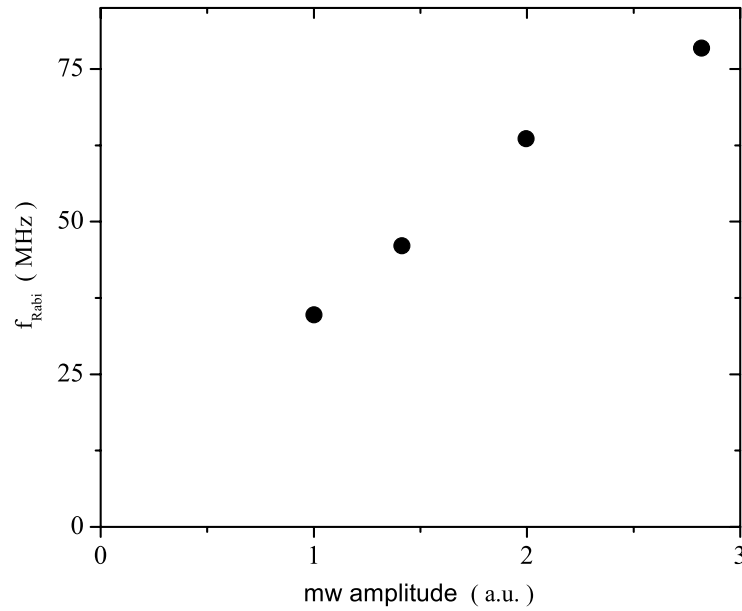


**Figure 4.13:** Observed Rabi frequency versus the applied microwave amplitude.

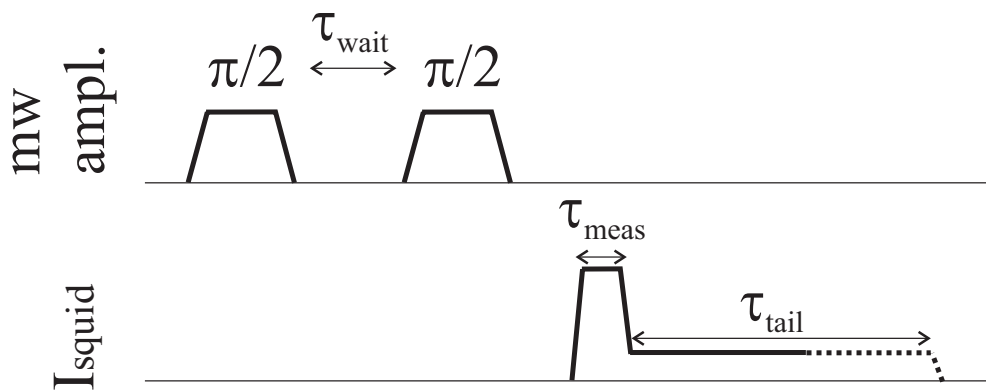


**Figure 4.14:** Ramsey interference scheme: The time between two  $\pi/2$  pulses is varied to probe the nondriven dephasing time of the system.

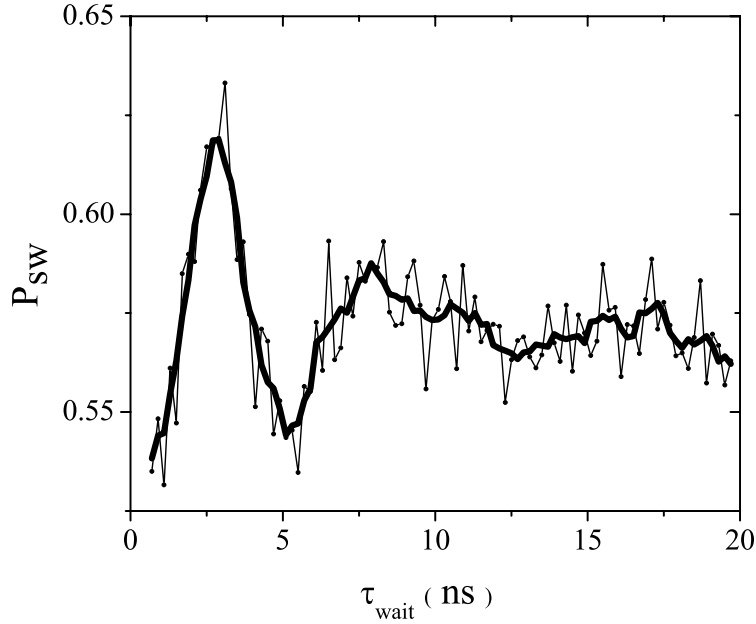


**Figure 4.15:** Ramsey interference pattern at a resonance frequency of 8GHz and a detuning of 200MHz. The interference pattern disappears after only  $\sim 7$ ns indicating a short  $T_2$ .

of  $\Delta\Phi = 40\mu\Phi_0$ . In practice this means that before a trace is taken, the exact position of the resonance should be determined. Even at the flux bias point with  $\frac{\partial\Delta E}{\partial\Phi_{ext}} = 0$  the minimum peak width is of the order of  $\sim 70$ MHz indicating an additional source causing a similar dephasing rate is present, which is not caused by correlated flux noise. Influence of long distance flux noise can thus be reduced [7], but the other noise source cannot. This source is asymmetric in nature. Possible sources are locally originated flux noise or critical current noise.

We changed the bias current through the SQUID and no change was observed, indicating influence of noise via the measurement circuit is not the limiting factor.

#### 4.4 Conditional spectroscopy from the first excited state to higher states.

To perform conditional qubit operations one needs to be able to induce coherent operations on the first qubit followed by coherent transitions on the second qubit.

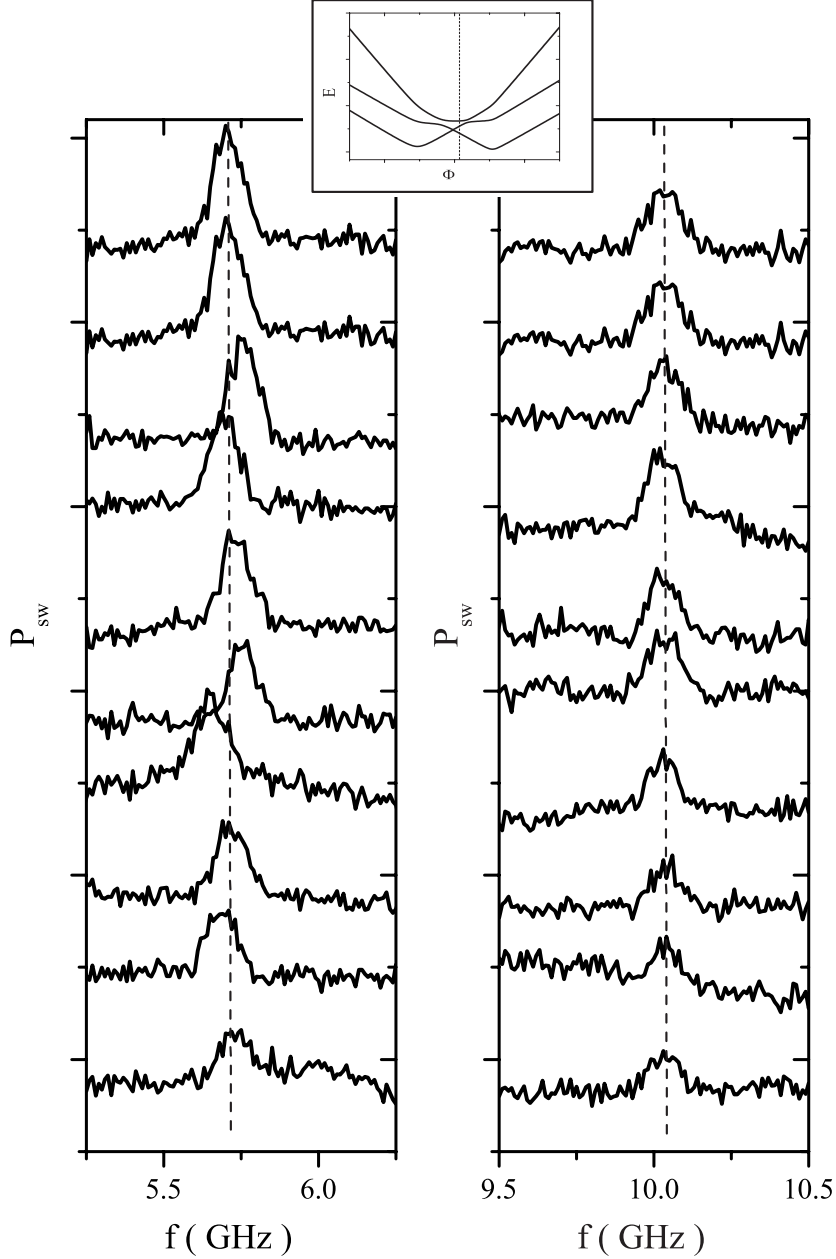


**Figure 4.16:** Measurements of the qubit resonance for the  $|0\rangle$  to  $|1\rangle$  and the  $|0\rangle$  to  $|3\rangle$  transition at a flux value as indicated in the level diagram in the inset by the dashed line. At this flux bias point the energy difference between the  $|0\rangle$  and  $|1\rangle$  state is not independent of the external flux  $\Phi_{ext}$  but the difference in energy between the  $|0\rangle$  and  $|3\rangle$  state is independent of the external flux. The resonances around  $f = 5.7$  GHz show random shifts of  $\Delta f \sim 75$  MHz from trace to trace while those jumps are not visible for the  $f = 10$  GHz resonances.

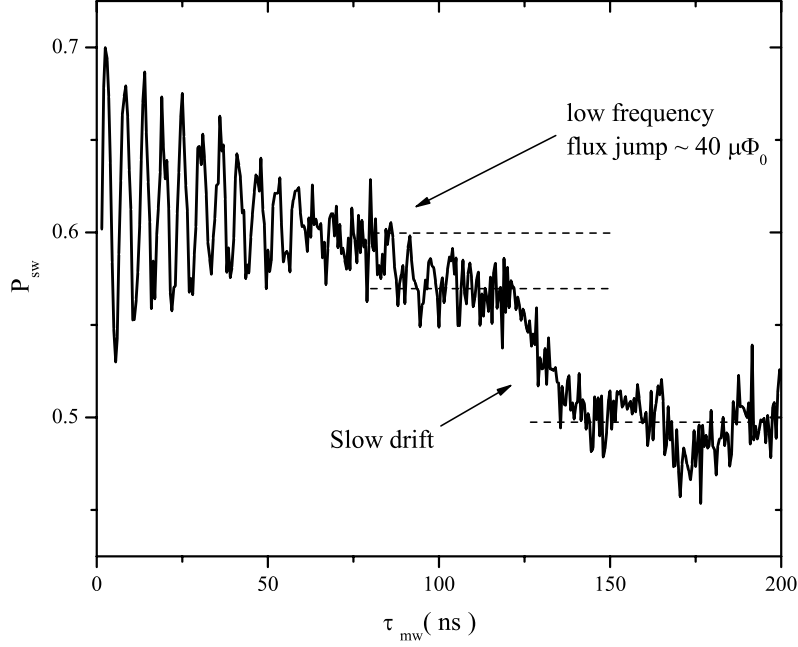


**Figure 4.17:** Rabi oscillations are clearly visible for pulse lengths up to  $\tau_{mw} \sim 60ns$ . When the measurement arrived at a pulse time of  $\tau_{mw} = 80ns$  the mean value of the signal changes, indicating a flux jump of  $\Delta\Phi \sim 40\mu\Phi_0$ . Low frequency flux jumps occur on a time scale of 5-15 minutes. Before every trace showing Rabi oscillations the maximum of the resonance is detected to make sure the Rabi measurement is performed on resonance.

To do this microwave pulses with different frequencies  $f_1$  and  $f_2$  have to be applied sequentially by combining two independent sources (figure 4.18).

A first step towards this is applying a  $\pi$ -pulse to so that the system coherently goes from the  $|0\rangle$  to the  $|1\rangle$  state followed by spectroscopy measurements on the second transition from the  $|1\rangle$  to the  $|3\rangle$  state (see figure 4.19). In this way we probe the location of the second resonance. In figure 4.20 a frequency sweep with  $\tau_2 = 50ns$  performed after an initial  $n\pi$ -pulse at frequency  $f_1$  is shown, with  $n = 0, 1, 2$  or  $3$ . For  $n = 1$  and  $n = 3$  the resonance at  $f_2 = 4.5GHz$ , associated with the  $|1\rangle$  to  $|3\rangle$  transition, indicating the system is excited after coherently populating the  $|1\rangle$  state. For  $n = 0$  and  $n = 2$  these resonances are not visible, indicating that only  $|0\rangle$  is populated at the moment the second microwave pulse is applied.

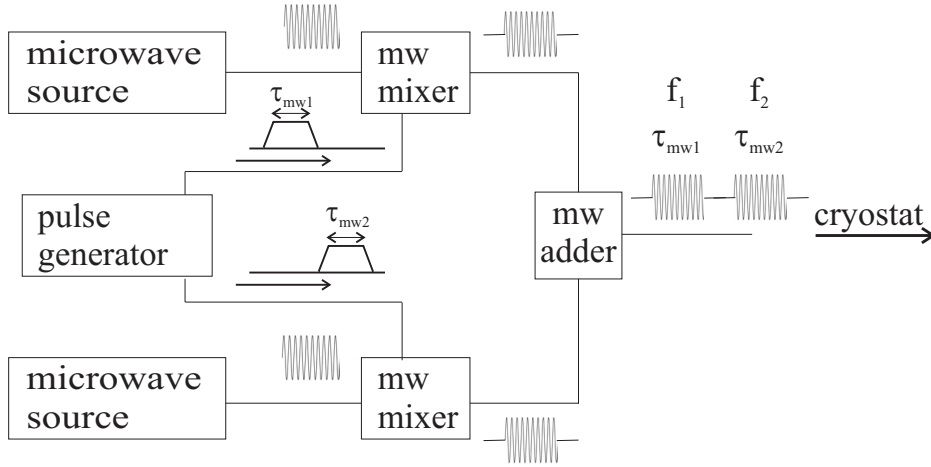


**Figure 4.18:** Setup for applying two consecutive microwave pulses of the order of 10 – 100ns. Each microwave source gives continuous-wave radiation. Pulses generated by a DC pulse generator are then multiplied with the microwaves creating microwave pulses. These two pulses of different frequencies and times are then added and inserted in the microwave line going down in the dilution refrigerator.

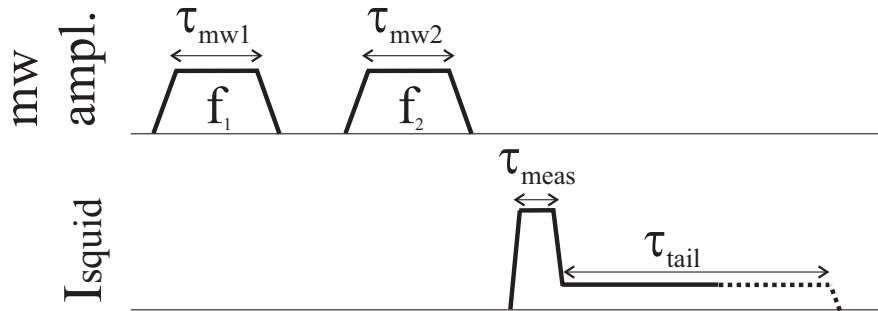


**Figure 4.19:** Timing scheme for applying multiple microwave pulses to the qubit before measuring. For addressing two transitions consecutive pulses of different frequency and duration are applied. First a  $n\pi$  pulse of duration  $\tau_{mw1}$  at frequency  $f_1$  is applied on the  $|0\rangle$  to  $|1\rangle$  transition. After that spectroscopy can be performed at frequency  $f_2$  from this higher state to the other states.

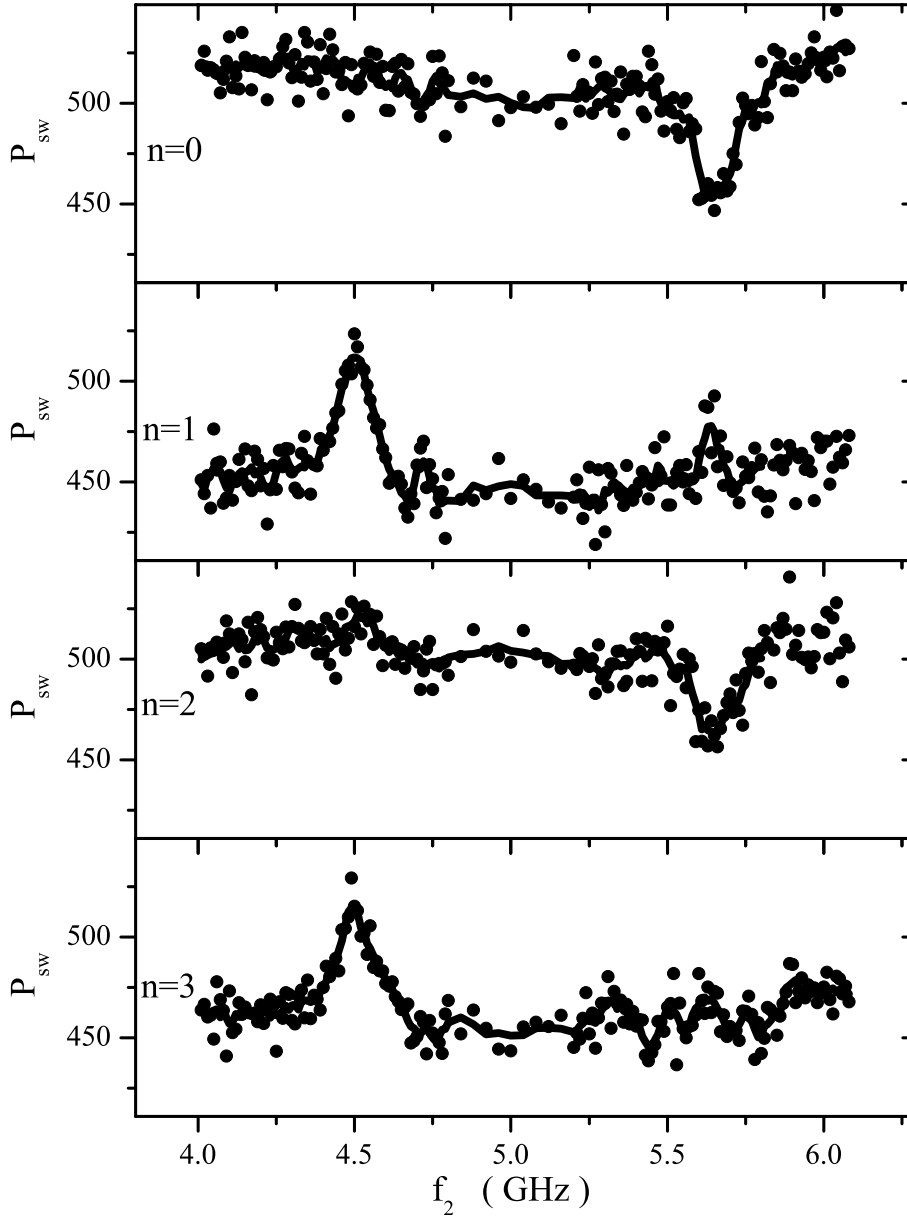


**Figure 4.20:** Conditional spectroscopy measurement. An  $n \cdot \pi$  pulse is applied at  $f_1 = 5.6$  GHz making the system go coherently to the  $|1\rangle$  state and back, depending on  $n$ . After this a  $\tau_2 = 50$  ns microwave burst is applied for various frequencies  $f_2$ . A resonance at  $f_2 = 4.5$  GHz is visible for  $n = 1$  and  $n = 3$ , indicating the energy difference between the  $|1\rangle$  state and the  $|3\rangle$  state corresponds to that frequency.

## 4.5 Conclusions

Continuous wave spectroscopy measurement from the ground state as well as from the partially populated first excited state reveal the level structure of the 2-qubit system. It is shown that the measured level structure can be explained by using the four level approximation of two coupled Josephson persistent current qubits each described as a two state system, coupled via  $\sigma_z\sigma_z$  coupling. Coherent oscillations flipping each qubit have been performed by applying microwaves to the coupled qubit system. The oscillations are visible for pulse lengths up to  $\tau_{mw} \sim 75ns$ . Ramsey interference measurements indicate a short non-driven dephasing time of the order of 7 ns. Conditional spectroscopy measurement from the first excited state to higher states are observed after applying a  $\pi$ ,  $2\pi$  or  $3\pi$  -pulse to go from the ground state to the higher lying states followed by a longer microwave burst. Low frequency flux jumps are observed causing the peak position to shift in the order of  $75MHz$ . This shift was reduced when the system was biased in a region where the levels are to first order independent of the external applied flux. However, no major improvement is seen when operating in such a point indicating the long distance flux jumps were not the only source of dephasing.

## References

- [1] Yu. A. Pashkin, T. Yamamoto, O. Astafiev, Y. Nakamura, D.V. Averin, J. S. Tsai, "Quantum oscillations in two coupled charge qubits" *Nature* **421**, 823 (2003).
- [2] T. Yamamoto, Yu. A. Pashkin, O. Astafiev, Y. Nakamura, J. S. Tsai, "Demonstration of conditional gate operation using superconducting charge qubits" *Nature* **425**, 941 (2003).
- [3] I. Chiorescu, P. Bertet, K. Semba, Y. Nakamura, C. J. P. M. Harmans, J. E. Mooij, "Coherent dynamics of a flux qubit coupled to a harmonic oscillator" *Nature* **431**, 159 (2004).
- [4] J. B. Majer, F.G. Paauw, A.C.J. ter Haar, C.J.P.M. Harmans, J.E. Mooij, "Spectroscopy on two coupled superconducting flux qubits", cond-mat/0308192.
- [5] A. Izmailkov, M. Grajcar, E. Ilichev, Th. Wagner, H.-G. Meyer, A.Yu. Smirnov, M. H. S. Amin, Alec Maassen van den Brink, and A.M. Zagoskin, "Evidence for Entangled States of Two Coupled Flux Qubits", *Phys. Rev. Let* **93** (2004).

- [6] R.J. Schoelkopf, A.A. Clerk, S.M. Girvin, K.W. Lehnert and M.H. Devoret, "Qubits as spectrometers of quantum noise", cond-mat/0210247 (2002).
- [7] M.J. Storcz, and F. K. Wilhelm, *Phys. Rev. A.* **67**, 042319 (2003).

## Chapter 5

# Phase distribution in current carrying double layer superconducting lines

Superconducting persistent current qubits are made by 2-angle shadow evaporation. This technique results in structures and lines consisting of a double aluminium layer with an oxide barrier in between. These structures are modelled and the phase distribution in the lines is investigated. Employing a double layer line for coupling two Josephson persistent current qubits is discussed. It will be shown that, with a carefully chosen design, the coupling strength can be designed over a large range of values making this way of coupling qubits an attractive one.

## 5.1 Introduction

Superconducting two level systems require small Josephson junctions which can be made using shadow evaporation. Evaporation of aluminium is done under two angles, and in between the evaporation steps the first aluminium layer is oxidized creating a barrier that forms the Josephson junction. Due to the shadow evaporation technique most structures consist of superconducting parts on top of each other, separated by a large area junction. In the case of a single Josephson persistent current qubit the additional junctions are larger than the three junctions forming the potential landscape of the system so their influence is small. The phase drop over such a line depends on the detailed way the current flows. This double layer structure is modelled in order to gain understanding of the phase and current distributions. This enables us to use these double layers with their distributed junctions in designing new and more complex systems, like coupling two or more qubits. Also phase drop over these extra junctions can be calculated and taken into account in the design of a system.

In section 5.2 the double layer structure with its distributed junction will be modelled and the differential equations describing the phases in these systems are derived. In section 5.3 stationary solutions for various cases will be given. After this in section 5.4 an example of how to use this extra layer as a coupling element is discussed.

## 5.2 Modelling a double layer separated by a thin oxide barrier

In superconducting devices fabricated using shadow evaporation techniques, like the Josephson junction in figure 5.1, one evaporates aluminium under two angles with an oxidation step in between to define the junction barrier. This aluminium oxide barrier is present in all lines fabricated in the same step as the Josephson junctions and thus all lines are actually two lines separated by a distributed junction.

To describe the phase distribution as a function of the position  $x$  along the line the currents in the line are considered [1, 2]. Schematically a line with an inductance  $L$  and critical current  $I_c$  is depicted in figure 5.2. Taking the limit of  $\Delta x \rightarrow 0$ , differential equations are derived describing the phases in these lines.

At the bottom (top) node there are three currents  $I_{b,in}(x)$ ,  $I_{b,out}(x)$  and  $I_{\perp}(x)$  ( $I_{t,in}(x)$ ,  $I_{t,out}(x)$  and  $I_{\perp}(x)$ ) according to figure 5.2. The distributed critical current per unit length between the layers and the distributed capacitance between the

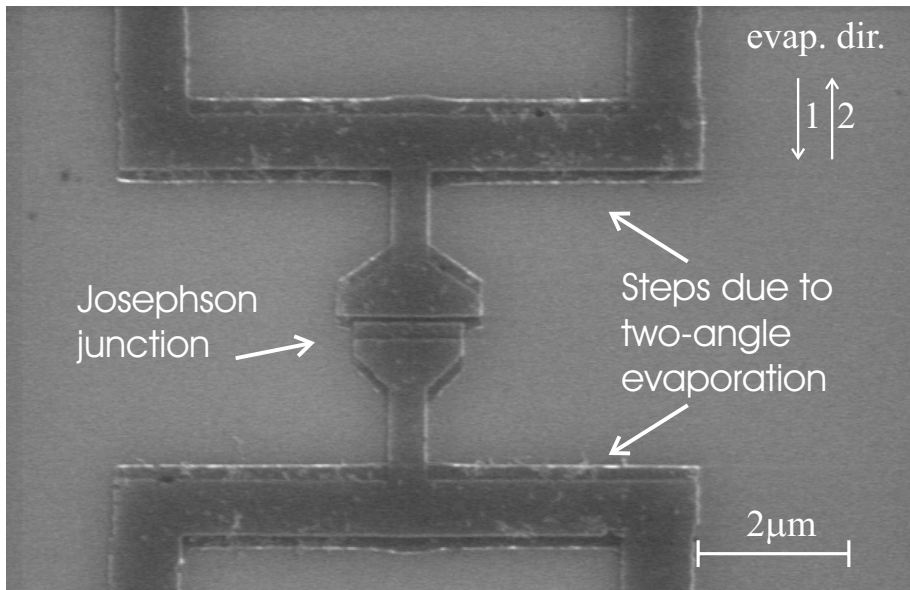


**Figure 5.1:** Josephson junction fabricated using shadow evaporation. Aluminium is evaporated under two angles with an oxidation step between the evaporation steps. The aluminium oxide barrier forms the junction. The lines from the two evaporation steps are shifted with respect to each other in the direction of the shadow evaporation indicated by arrow 1 and 2. This shift creates the actual junction and the steps in the lines.

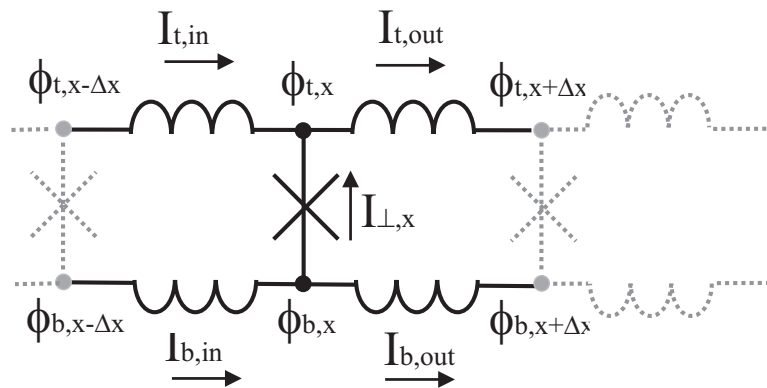


**Figure 5.2:** Equivalent electric circuit of a small section of double layer line. The line consists of two layers of inductors (top and bottom) which are coupled to each other via a distributed Josephson junction. In the nodes phases  $\phi_t$  and  $\phi_b$  and in the lines currents  $I_b$ ,  $I_t$  and  $I_{\perp}$  are defined.

layers per unit length are given by  $i_c = \frac{I_c}{Length}$  and  $c = \frac{C}{Length}$ , so they are given in A/m and F/m. Because the two layers have different inductances (as is the case in our shadow evaporation process where the thickness of the bottom and top layers are different) the distributed inductances  $l_b = \frac{L_b}{Length}$  for the bottom and  $l_t = \frac{L_t}{Length}$  for the top layer are used. For a small section of line with length  $\Delta x$  the critical current, capacitance and inductances are now given by  $i_c \Delta x, c \Delta x$ ,  $l_b \Delta x$  and  $l_t \Delta x$ . The current in a superconductor is related to the phase along the superconductor according to  $\Delta\phi = 2\pi \frac{IL}{\Phi_0}$  where  $L$  is the total inductance of the line and  $I$  is the current through the line. The various currents in figure 5.2 can be written as a function of the phase in the nodes of the line by:

$$\begin{aligned}
I_{b,in}(x) &= \frac{\Phi_0}{2\pi} \frac{1}{l_b \Delta x} (\phi_b(x) - \phi_b(x - \Delta x)) \\
I_{b,out}(x) &= \frac{\Phi_0}{2\pi} \frac{1}{l_b \Delta x} (\phi_b(x + \Delta x) - \phi_b(x)) \\
I_{t,in}(x) &= \frac{\Phi_0}{2\pi} \frac{1}{l_t \Delta x} (\phi_t(x) - \phi_t(x - \Delta x)) \\
I_{t,out}(x) &= \frac{\Phi_0}{2\pi} \frac{1}{l_t \Delta x} (\phi_t(x + \Delta x) - \phi_t(x)) \\
I_{\perp}(x) &= (i_c \Delta x) \sin(\phi_t(x) - \phi_b(x)) + \frac{\Phi_0}{2\pi} c \Delta x (\ddot{\phi}_t(x) - \ddot{\phi}_b(x))
\end{aligned} \tag{5.1}$$

In each node there is current conservation  $I_{b,in}(x) = I_{b,out}(x) + I_{\perp}(x)$  and  $I_{t,in}(x) = I_{t,out}(x) - I_{\perp}(x)$ . By using (5.1) these current conservation rules can be written as a function of the phases in the system:

$$\begin{aligned}
\frac{\Phi_0}{2\pi} \frac{1}{l_b (\Delta x)^2} [2\phi_b(x) - \phi_b(x - \Delta x) - \phi_b(x + \Delta x)] &= i_c \sin(\phi_t(x) - \phi_b(x)) + \frac{\Phi_0}{2\pi} c (\ddot{\phi}_t(x) - \ddot{\phi}_b(x)) \\
\frac{\Phi_0}{2\pi} \frac{1}{l_t (\Delta x)^2} [2\phi_t(x) - \phi_t(x - \Delta x) - \phi_t(x + \Delta x)] &= -i_c \sin(\phi_t(x) - \phi_b(x)) - \frac{\Phi_0}{2\pi} c (\ddot{\phi}_t(x) - \ddot{\phi}_b(x))
\end{aligned} \tag{5.2}$$

In the limit where  $\Delta x \rightarrow 0$  the equations actually contain the derivatives of the phase as a function of the position  $x$ . So differential equations are obtained of the form

$$\frac{\Phi_0}{2\pi} \frac{-\partial^2 \phi_b(x)}{\partial x^2} = l_b i_c \sin(\phi_t(x) - \phi_b(x)) + l_b \frac{\Phi_0}{2\pi} c (\ddot{\phi}_t(x) - \ddot{\phi}_b(x))$$

$$\frac{\Phi_0}{2\pi} \frac{-\partial^2 \phi_t(x)}{\partial x^2} = -l_t i_c \sin(\phi_t(x) - \phi_b(x)) - l_t \frac{\Phi_0}{2\pi} c(\ddot{\phi}_t(x) - \ddot{\phi}_b(x)) \quad (5.3)$$

By separating the sum and difference of the phases the two equations describing the phase difference across the layers and the total phase along the layers are now:

$$\frac{\Phi_0}{2\pi} \frac{\partial^2(\phi_t(x) - \phi_b(x))}{\partial x^2} = (l_b + l_t) i_c \sin(\phi_t(x) - \phi_b(x)) + (l_b + l_t) \phi_0 c(\ddot{\phi}_t(x) - \ddot{\phi}_b(x))$$

$$\frac{\Phi_0}{2\pi} \frac{\partial^2 \left( \frac{\phi_t(x)}{l_t} + \frac{\phi_b(x)}{l_b} \right)}{\partial x^2} = 0 \quad (5.4)$$

Finally, these equations can be written as equations describing both the total phase in the line and the phase difference between the top and the bottom part of the line by defining difference  $\phi_-(x) = \phi_t(x) - \phi_b(x)$  and sum  $\phi_+(x) = \frac{l_t + l_b}{2(l_t l_b)} \frac{(l_b \phi_t(x) + l_t \phi_b(x))}{2}$  coordinates. The average distributed inductance  $l$  is defined as  $l = (l_b + l_t)/2$ . For the case of equal inductances we simply end up with  $\phi_+(x) = \frac{(\phi_t(x) + \phi_b(x))}{2}$ . The system of the double superconducting layers with a distributed Josephson junction is described as

$$\begin{aligned} \frac{\Phi_0}{2\pi} \frac{1}{l} \frac{\partial^2 \phi_-(x)}{\partial x^2} &= 2i_c \sin(\phi_-(x)) + \frac{\Phi_0}{2\pi} c \ddot{\phi}_-(x) \\ \frac{\Phi_0}{2\pi} \frac{1}{l} \frac{\partial^2 \phi_+(x)}{\partial x^2} &= 0 \end{aligned} \quad (5.5)$$

The first equation describes the difference in phase between the top and the bottom layer as a function of the position  $x$  along the line. The second equation describes the phase as we move along the line. The fact that the second derivative of the sum of the phases is zero means there is a constant increase of (the weighted sum of the) phase along the top and bottom layer of the wire. One can see from these equations that the length scale governing the redistribution of the currents between the two layers is given by

$$\lambda = \sqrt{\frac{\Phi_0}{2\pi i_c (l_b + l_t)}} \quad (5.6)$$

Note that  $l$  contains both the geometric and the kinetic inductance, with in thin double layer lines the kinetic inductance being the dominating one. For a small transverse critical current  $i_c$   $\lambda$  will be large, since it is harder for the current to cross the layer.

### Application to double layer aluminium structures.

For the thin film aluminium wires used for making Josephson persistent current qubits the critical current densities are typically 100nA per 100nm by 100nm tunnelbarrier, giving for a 200nm wide wire a transverse critical current density of  $i_c = 2 \mu\text{A}/\mu\text{m}$ . For double layer wires of each 40 nm thick and 200nm wide the kinetic inductance is about 2 pH/ $\mu\text{m}$  [1, 2, 3]. For such wires the length scale for crossing between the layers of the inserted currents is  $\lambda \approx 5\mu\text{m}$ .

## 5.3 Stationary solutions for the current and phase distribution

Assuming  $I_{bias} \ll I_c$  we derive stationary solutions for two cases. One is the case where the current is inserted in the bottom layer of an infinitely long line. The second case is where the current inserted in the bottom layer will be extracted at the top layer at a fixed distance  $x_0$ .

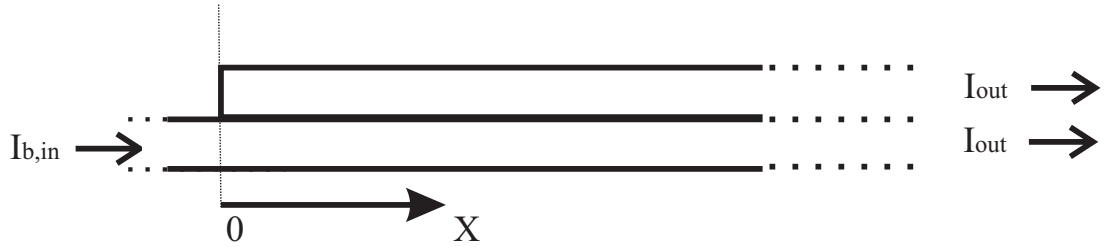


**Figure 5.3:** In the double layer line the current is injected on one side in the bottom layer, and divides equally between the layers after some distance  $x \gg \lambda$ .

For small transverse currents the current in the junction can be written as  $2i \sin(\phi_t(x) - \phi_b(x)) \approx 2i(\phi_t(x) - \phi_b(x))$  hence equation 5.5 can be written as

$$\begin{aligned} \frac{\Phi_0}{2\pi l} \frac{\partial^2 \phi_-(x)}{\partial x^2} &= 2i_c(\phi_-(x)) \\ \frac{\Phi_0}{2\pi l} \frac{\partial^2 \phi_+(x)}{\partial x^2} &= 0 \end{aligned} \quad (5.7)$$

These equations will be used to calculate the phase distribution in the line. In order to derive the currents flowing in the system we have to look at the phase difference between the layers  $\phi_-(x)$  for the transverse current, and at the sum phase  $\phi_+(x)$  for the current in the parallel direction.

$$I_t(x) = \frac{\Phi_0}{2\pi l} \frac{\partial \phi_t(x)}{\partial x} \quad (5.8)$$

$$I_b(x) = \frac{\Phi_0}{2\pi l} \frac{\partial \phi_b(x)}{\partial x} \quad (5.9)$$

### Current in an infinite line of indential layers

For the case shown in figure 5.3 with the current inserted in the bottom layer the solution to equation 5.7 is of the form  $\phi_{-(x)} = Ae^{-\frac{x}{\lambda}}$  where  $\lambda = \sqrt{\frac{\Phi_0}{2\pi i_c(l_b+l_t)}}$ .

For large values of  $x$  the phase difference between both layers approaches zero. To determine the value of  $A$  the boundary condition of the problem is taken into account. For  $x \rightarrow \infty$  the phases are equal and for identical layers half the inserted current  $I_{bias}$  has flown from the bottom to the top layer. The current as a function of the position  $x$  is given by  $I_{\perp(x)} = (i_c \Delta x) \phi_{-(x)}$  so  $\frac{I_{bias}}{2} = \int_0^{\infty} i_c A e^{-\frac{x}{\lambda}} dx$  giving  $A = \frac{1}{\lambda} \frac{I_{bias}}{2i_c}$ . The average phase increase  $\phi_{+(x)}$  is the average of the phase in the top and the bottom layer. This means the phases in the system are given by

$$\phi_{-(x)} = \frac{1}{\lambda} \frac{I_{bias}}{2i_c} e^{-\frac{x}{\lambda}} \quad (5.10)$$

$$\phi_{+(x)} = \frac{l2\pi}{\Phi_0} \frac{I_{bias}}{2} x \quad (5.11)$$

For the case of identical layers with a current  $I_{b,in} = 300nA$  and  $i_c = 2\mu A/\mu m$  the phase difference is plotted in figure 5.4 for the cases where  $l = 0.5pH/\mu m$  and  $l = 2pH/\mu m$ . The phase difference drops exponentially, while the average phase picked up by the line increases linear in  $x$ . For a higher value of the inductance per meter  $l$  the phase is forced to equalise faster. The currents in the transverse direction  $I_{\perp}(x)$  and the average current per layer in the parallel direction  $I_{+}(x) = \frac{I_t(x)+I_b(x)}{2}$  are

$$I_{\perp}(x) = i_c \phi_{-(x)} = \frac{1}{\lambda} \frac{I_{bias}}{2} e^{-\frac{x}{\lambda}} \quad (5.12)$$

and

$$I_{+}(x) = \frac{\phi_0}{l} \frac{\partial \phi_{+}(x)}{\partial x} = \frac{I_{bias}}{2} \quad (5.13)$$

as plotted in figure 5.5. The current is injected in the bottom layer, while  $I_{t,in} = 0$ . After some distance part of the current has crossed the barrier between the layers, and the phases in both layers become equal. For the symmetric case this means the currents flowing in the top and bottom layer become equal.

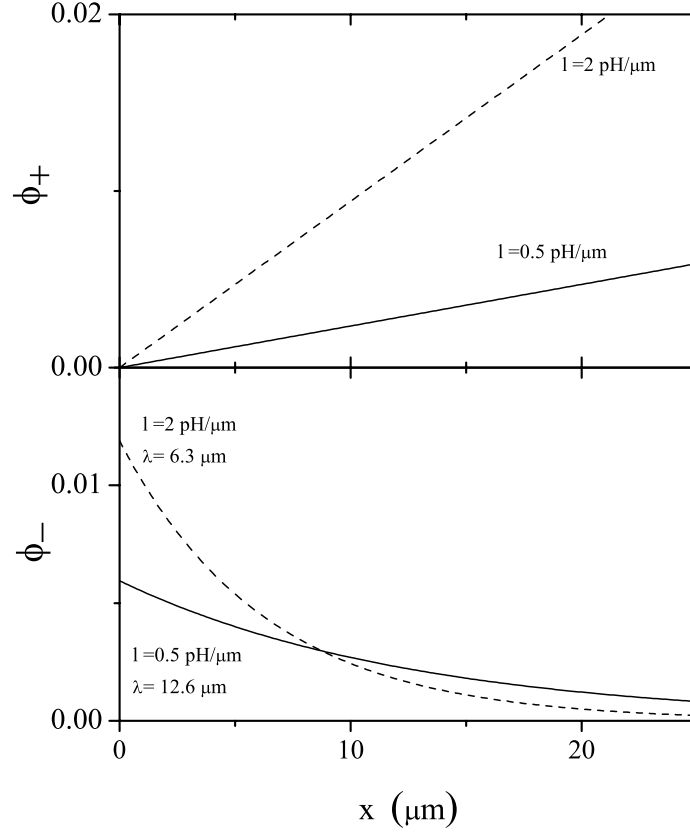


**Figure 5.4:** *a. Sum and difference of the phase in an infinite line consisting of identical layers for various values of  $l$ . Current is inserted in the bottom layer and will redistribute over a typical length scale  $\lambda$ . The bias current is  $I_{bias} = 300nA$ , the critical current  $i_c = 2\mu A/\mu m$ . The inductances are  $l = 0.5pH/\mu m$  (dotted) and  $l = 2pH/\mu m$  (solid), giving a redistribution length of  $\lambda = 12.6\mu m$  and  $\lambda = 6.3\mu m$  respectively. For the line with the higher inductance per meter the phase increases faster along the line, and redistribution of the current occurs earlier since the current flows easier through the junction layer.*

### Transverse current between bottom and top layer

The case where the current is injected on the left in the bottom layer and is extracted at the top layer is depicted in figure 5.6.

The current has to cross the barrier between the layers in the distance  $x_0$ . Due to the symmetry of the problem the function describing the phase difference is of the form  $\phi_-(x) = A[e^{\frac{x}{\lambda}} + e^{-\frac{x}{\lambda}}]$ , since current always flows from the bottom to

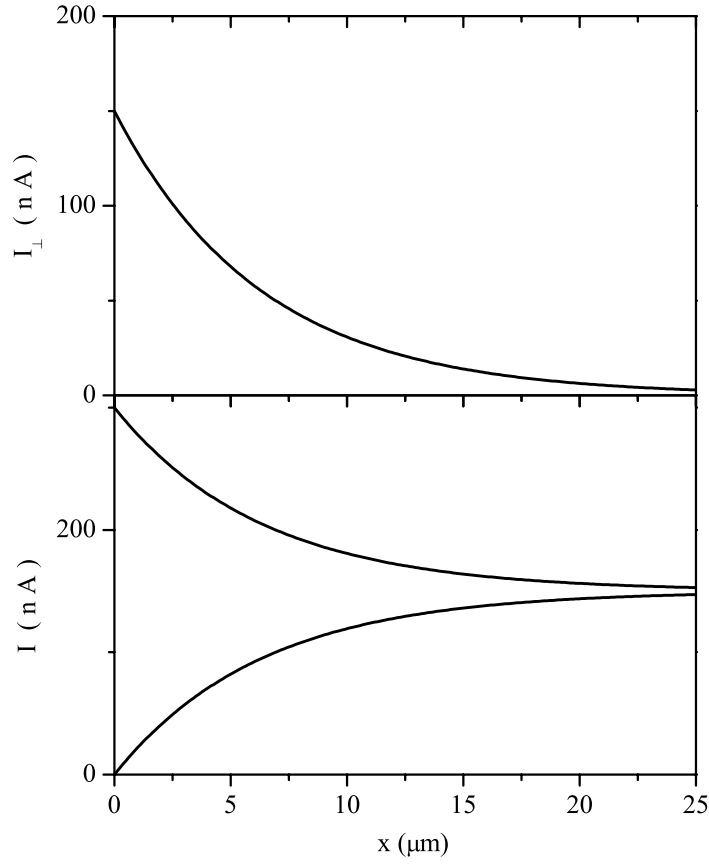


**Figure 5.5:** Plot of the transverse current, the current in the bottom and the current in the top layer for an infinite line consisting of identical layers. The inserted current is  $I_{b,in} = 300\text{nA}$ . The transverse current per micrometer is at a maximum in the beginning of the line, and approaches zero when the currents in the longitudinal direction are equal.

the top line. Also the distribution of the transverse current should be symmetric around the middle of the line. The boundary condition to the equation is that all the current should go through the barrier between the left side of the wire at  $x = -\frac{x_0}{2}$  and the right side at  $x = \frac{x_0}{2}$  giving

$$I_{b,in} = \int_{-\frac{L}{2}}^{\frac{L}{2}} i_c A [e^{\frac{x}{\lambda}} + e^{-\frac{x}{\lambda}}] dx \quad (5.14)$$

or

$$I_{b,in} = [i_c A \lambda [e^{\frac{x}{\lambda}} - e^{-\frac{x}{\lambda}}]]_{-\frac{L}{2}}^{\frac{L}{2}} = i_c A 2 \lambda [e^{\frac{L/2}{\lambda}} - e^{-\beta \frac{L/2}{\lambda}}] \quad (5.15)$$

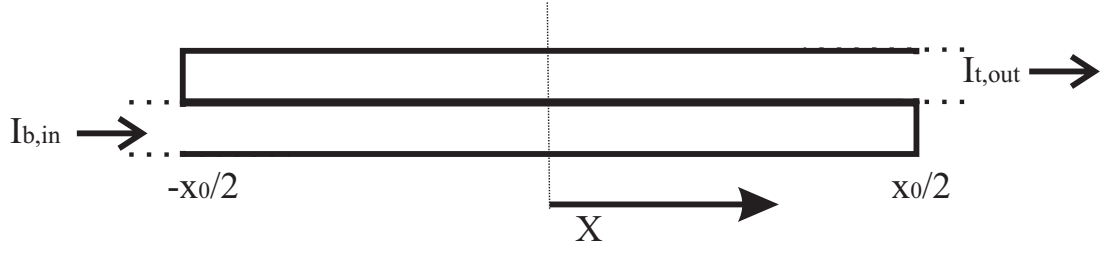


**Figure 5.6:** A double layer line where the current is injected on one side in the bottom layer, and is extracted from the top layer at the other side of the line.

from which we can extract  $A$  :

$$A = \frac{I_{b,in}}{i_c} \frac{1}{2\lambda} \frac{1}{[e^{\frac{L/2}{\lambda}} - e^{-\frac{L/2}{\lambda}}]} \quad (5.16)$$

This gives for the phase difference between bottom and the top layer :

$$\phi_{-(x)} = \frac{I_{bias}}{i_c} \frac{1}{2\lambda} \frac{e^{\frac{x}{\lambda}} + e^{-\frac{x}{\lambda}}}{e^{\frac{L/2}{\lambda}} - e^{-\frac{L/2}{\lambda}}} \quad (5.17)$$

In the limit where the inductance  $l$  of the line goes to zero, the typical length scale  $\lambda$  will go to infinity. This means that there will be (almost) no phase drop over the inductance of the wire and there will be phase drop over the distributed junction only. Since

$$\lim_{\lambda \rightarrow \infty} \frac{I_{b,in}}{i_c} \frac{1}{\lambda} \frac{[e^{\frac{x}{2\lambda}} + e^{-\frac{x}{\lambda}}]}{[e^{\frac{L/2}{\lambda}} - e^{-\frac{L/2}{\lambda}}]} \approx \frac{I_{bias}}{i_c L} \quad (5.18)$$

the line works as if there is a single junction between the parts of the line, with uniform phase, with a critical current of  $i_c \cdot Length$ , the critical current of the total line area.

In figure 5.7 the phase difference and the sum of the phases are shown as a function of the position  $x$  for various values of  $l$  for a given bias current. In figure 5.7a the slope of the sum of the phases is given by the inductance: the higher the inductance, the larger the phase difference established for a given bias current through the line. The phase differences are most significant at the points where the current is injected or extracted from the line (figure 5.7b). Here the difference in current between the top and bottom layer is largest. In the middle half of the current is flowing in the bottom layer and half of the current is flowing in the top layer. For large values of the inductance  $l$  the currents

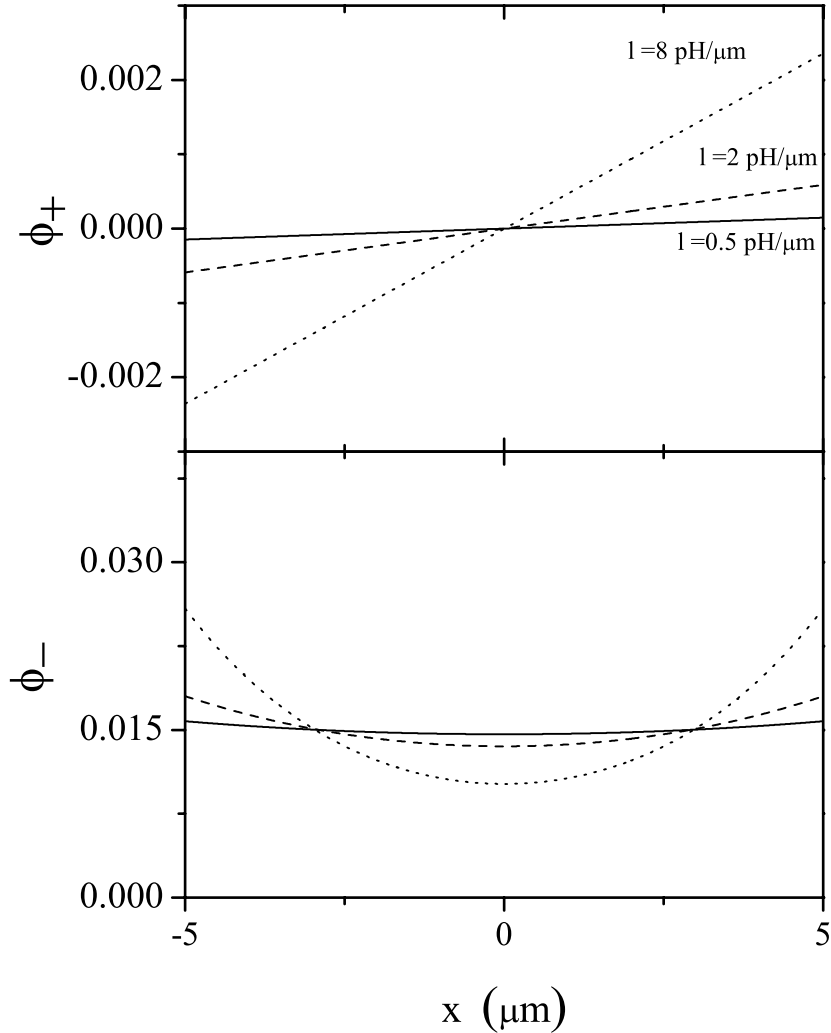


**Figure 5.7:** Sum and difference of the phase in a double layer line for various values of  $l$ .  $I_{bias} = 300\text{nA}$ , and the distributed critical current is  $i = 2000\text{nA}/\mu\text{m}$ . For a higher value of  $l$  the current will be forced to cross to the other layer closer to the edges of the line, creating a larger phase difference there. Currents will then be equally redistributed in the middle, minimizing the phase difference there.

redistribute quicker once inserted into the structure. For small values of  $l$  the current will flow throughout the top or bottom layer more easily, and will cross the barrier over the whole junction. The phase difference across the barrier is almost

independent of the position along the line. The structure acts just as a single junction with, for  $i_c = 2\mu A/\mu m$  and a length of  $x_0 = 10\mu m$ , a critical current of  $I_c = i_c \cdot Length = 20\mu A$ . This gives for an imposed current of  $I_{bias} = 300nA$  a phase difference of  $\Delta\phi = \frac{300nA}{20\mu A} \approx 0.015$

## 5.4 Application of a double layer distributed junction as coupling element

In the previous sections it is shown how to calculate current and phase distributions in double superconducting layers with a tunneling layer. This procedure can also be used to accurately design an element for coupling Josephson persistent current qubits via their phase degree of freedom, see chapter 3. This is done by forcing the currents of both qubits to cross at a well defined part of the circuit. This coupling island is shown in figure 5.8. The currents from the qubits enter the central island via the top layer on the right, and is extracted from the bottom layer on the left. In this way the island behaves as a large Josephson junction. For the typical shadow evaporated junctions used for the samples discussed in this thesis the critical current is for the central island in figure 5.8  $I_c \sim 40\mu A$ . The kinetic inductance per meter for one layer is  $l \approx 0.5pH/\mu m$ , which makes that the current divides equally over the  $4\mu m$  by  $1\mu m$  sized island. The island therefore acts as a single junction with a critical current  $\sim 40\mu A$ , giving a Josephson coupling of  $M = \frac{\Phi_0}{2\pi I_c} \sim 10pH$ , which is in the desired range.

## 5.5 Summary

In a realistic design it is important to take into account that with shadow evaporation we usually end up with double layer structures, forming both wanted and unwanted junctions and inductances. The current redistribution length  $\lambda$ , is of the order of a few micro meter. For qubits with a typical size of  $\lambda$  the behaviour of the lines depend strongly on the details of the lines. By modelling these double layers, the effects can be accurately quantitatively analysed. The unwanted effects can then be taken into account in the system description and can be minimized.

Also double layers can be used to accurately design an element for coupling qubits. This allows for greater flexibility in systems in which two or more qubits or a qubit and a squid are coupled. That this coupling can be designed within the wanted range for Josephson persistent current qubits is shown in chapter 3.

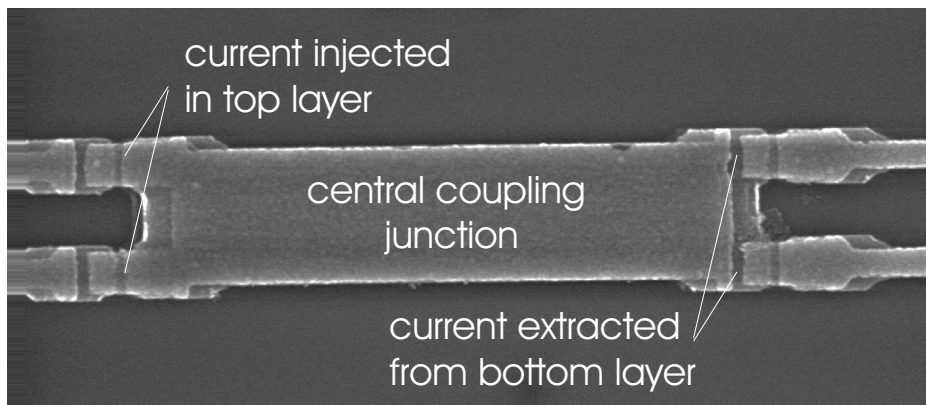


**Figure 5.8:** SEM picture of a part of the coupled qubit system described in chapter 3. The two top junctions are part of one qubit, the two bottom junctions of the other. The current is forced to enter the central island in the top layer on the left and is extracted from the bottom layer on the right. The island consists of two layers separated by a large distributed Josephson junction and therefore determines the coupling between the qubits. The island has a critical current of  $I_c \approx 40\mu A$  and gives a coupling of  $M \approx 10pH$ .

Important for this is accurate knowledge of both the kinetic inductance as well as the critical currents in the specific lines involved.

## References

- [1] T. Orlando, "Foundations of Applied Superconductivity" (1991).
- [2] M. Tinkham, "Introduction to Superconductivity" (1996).
- [3] R. Meservey and P.M. Tedrow, "Measurements of the Kinetic Inductance of Superconducting Linear Structures", *J. of App. Phys.*, **40**, 5, 2028 (1969).



## Chapter 6

# Gradiometer qubit with trapped fluxoid bias

A gradiometer type Josephson persistent current qubit is fabricated to reduce the influence of external flux noise from far away from the qubit on the qubit bias energy. In addition, qubit phase bias is obtained using a fluxoid trapped in a solid superconducting loop is used. To demonstrate the viability of this approach a simple sample without on-chip resistors and capacitors was fabricated and tested. Spectroscopy measurements demonstrate flux biasing of the qubit works.

## 6.1 Introduction

To operate qubits it is required to maintain coherence for a sufficient period of time. Dephasing times in the order of hundreds of  $100ns$  have been established in superconducting devices [1, 2, 3, 4, 5, 6] by operating in the degeneracy point where the energy levels are, to first order, independent of flux or charge. Superconducting quantum systems with  $E_J \gg E_c$ , like the Josephson persistent current qubit, are especially sensitive to phase or flux fluctuations. Noise can be caused by for example thermal fluctuations from resistors coupling to the control lines and measurement circuit [7], by variations in the critical currents of the junctions [8], charge noise [9, 10], and by magnetic field variations. One way to reduce influence from magnetic field or flux noise is to use a gradiometer type qubit. Measurements performed on a gradiometer type Josephson persistent current qubit will be discussed. The main purpose of the gradiometer qubit is to create a quantum system which is not limited to operation in the degeneracy point by reducing influence of flux noise to a level where it is no longer a limiting factor in qubit operations.

A gradiometer qubit can consist of a simple qubit loop with a twist in the loop, making the current in half the loop flow in the opposite direction compared to the current in the other part of the loop (figure 6.1a). The total flux enclosed by the loops will then cancel for flux noise generated at a long distance. Our design of the gradiometer qubit as shown in figure 6.1b works the same as the configuration with a physical twist. The persistent current splits in two circulating currents flowing in opposite directions. Any flux picked up by the left loop will be counteracted by flux through the right loop since the persistent current flows in the opposite direction there. Therefore, also this configuration acts as a gradiometer. The attractive advantage of this is that trapped fluxoids can be used to phase bias the system.

The Josephson persistent current qubit needs a stable phase bias for operation. Since applying strong local magnetic fields is difficult, phase biasing of the circuit via a trap loop in which a fluxoid is trapped can be used to apply a local phase to a system [11]. For any system one needs local control lines for shifting the operating point around the degeneracy point at  $\Phi = \frac{1}{2}\Phi_0$  which can introduce severe decoherence and should therefore be carefully designed. However, since the trapped fluxoid is used to bring the qubit to the degeneracy point only a small magnetic shift is needed which allows weak coupling of the control line to the qubit. The first configuration however needs a large coupling to the flux bias line to apply the initial bias of  $\Phi = \frac{1}{2}\Phi_0$  causing severe decoherence via the control circuit. Due to the gradiometer configuration the signal produced by the

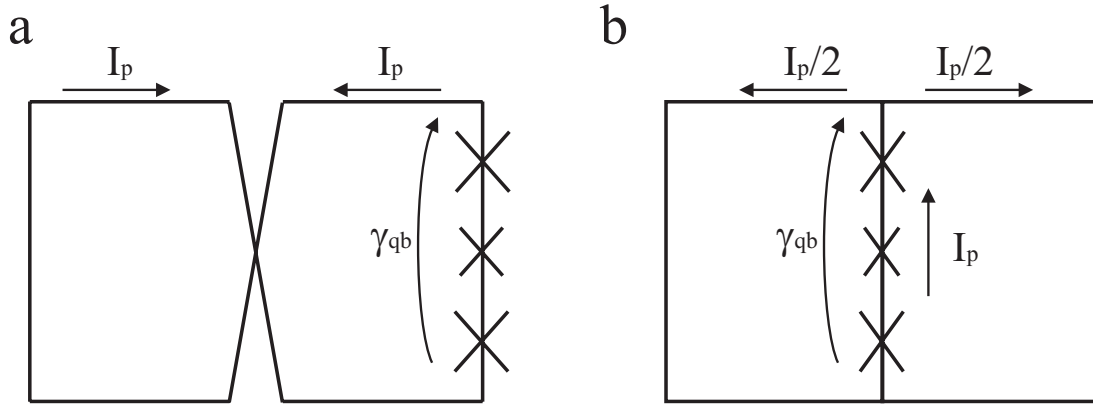


**Figure 6.1:** Josephson persistent current qubit with a gradiometer configuration. Any change in flux induced from a source at a large distance will influence the energy bias of the qubit less than a non gradiometer configuration. This gradiometer configuration can be obtained by adding a crossing in the qubit loop (a) or by making the qubit current flow into two branches (b). The advantage of this second method is that trapped fluxoids can be used to bias the system at a phase of  $\pi$ . Making a small physical crossing as shown in (a) is hard using aluminium shadow evaporated junctions. Both methods require local on-chip flux bias lines for operating the system around the degeneracy point

qubit should be read-out locally using an asymmetrical coupled squid.

Another advantage of the gradiometer flux qubit will become clear when more than a few qubits will be fabricated on chip near each other all with control lines, tunable couplings and read-out SQUIDS. One needs to avoid cross-talk in such a complex system of qubits, SQUIDS, and current carrying lines, and make sure interaction can be switched off almost completely. This will be much easier when a gradiometer configuration is used.

In section 6.2 the influence of flux noise and an unstable flux bias will be discussed. In section 6.3 the principles of the gradiometer Josephson persistent current qubit will be explained. Experimental data shows that trapped fluxoid biasing is achieved. Due to the lack of on-chip circuitry the effect of this on the phase stability could not be investigated.

## 6.2 Dephasing due to an unstable flux bias

The energy level separation of the qubit can be tuned by applying a magnetic flux to the qubit loop (chapter 2). When this flux bias is unstable the resonance peaks are broadened due to the varying energy bias.

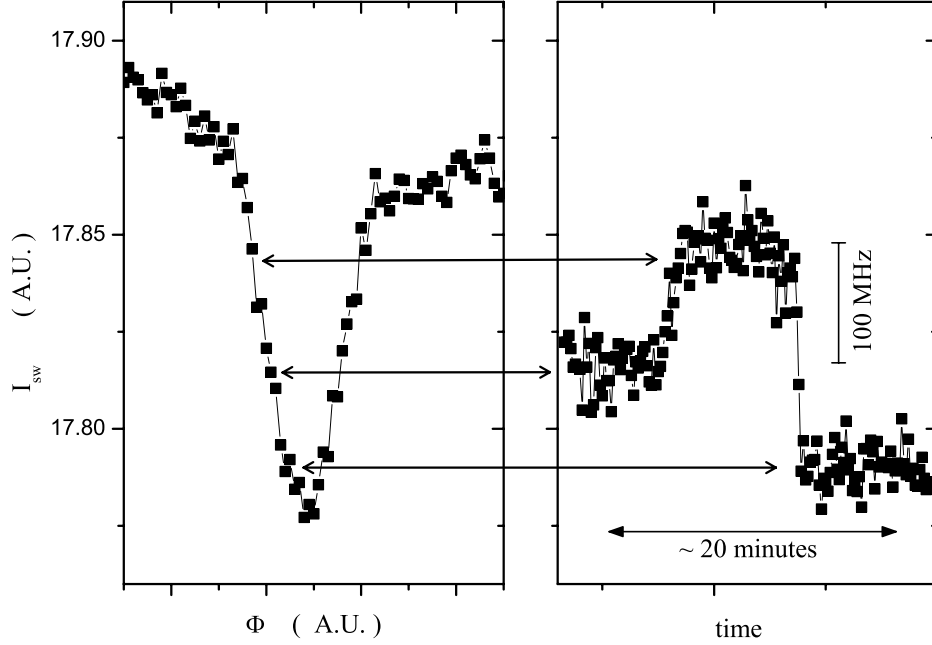


**Figure 6.2:** The left panel shows a resonance of a non-gradiometer type qubit at an energy splitting of  $f = 18.96\text{GHz}$ . To the right are measurements taken at a fixed external flux bias point of the qubit on the slope of the resonance curve. One can clearly see flux jumps on a time scale of minutes moving the energy bias around the resonance, indicating flux jumps are present locally.

In figure 6.2 measurements are shown in which the magnetic field was tuned to be on the slope of a resonance peak. Here the measured signal is highly sensitive to the applied flux. One can see jumps at typical time scales of 10 minutes. The amplitude of the jumps are of the order of  $\Delta\Phi = 5 \cdot 10^{-5}\Phi_0$ , or  $\sim 100\text{MHz}$ , giving an inhomogeneous dephasing time  $T_2^* = \frac{1}{\pi f} \approx 3\text{ns}$ . In order to decrease the sensitivity to flux noise one can use a gradiometer configuration so that flux jumps originated far away are -to first order- cancelled. For a line width of approximately  $100\text{kHz}$ , giving a dephasing time  $T_2^*$  of  $3\mu\text{s}$  the variations in flux bias of the qubit should be of the order of  $\delta\Phi \approx 5 \cdot 10^{-8}\Phi_0$ . For a typical qubit loop of  $5$  by  $5\mu\text{m}^2$ , a field stability of  $\delta B \approx 4 \cdot 10^{-12}\text{T}$  is required. The gradiometer can be used to gain a factor  $\sim 100$  in suppression of flux sensitivity to fluctuations from long distance flux sources.

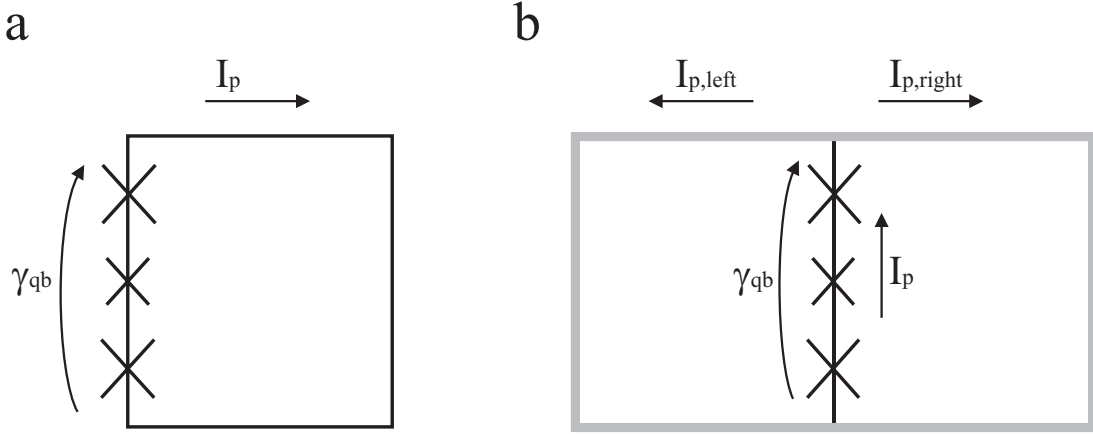


**Figure 6.3:** The layout of the simple Josephson persistent current qubit (a) can be mapped on a gradiometer type qubit with trapped fluxoid bias (b). Half of the qubit current  $I_{qb}$  will flow clockwise, half will flow anti clockwise so the phase picked up by a homogeneous external magnetic field is cancelled.

### 6.3 Gradiometer qubit with phase bias by a superconducting trap loop

The gradiometer type qubit with trapped fluxoid bias is schematically shown in figure 6.3b. The three junctions in the middle line form the Josephson potential just as in the case of a single loop qubit.

For identical loops the persistent current of the qubit will divide equally between the two branches, half going right ( $I_{p,right}$ ) and half going left ( $I_{p,left}$ ). The qubit should be phase biased around  $\gamma_{qb} \approx \pi$ , where  $\gamma_{qb}$  is the sum of the phases over the three qubit junctions, for the system to behave as a two level system. To apply this necessary phase bias of  $\gamma_{qb} = \pi$  over the qubit junctions a trapped fluxoid in the solid superconducting ring can be used [11]. The phase  $\gamma_{tr}$  (figure 6.4) is now the integral of the divergence of the phase along the superconducting line.

$$\gamma_{tr} + 2\pi \frac{\Phi_{ext} + \Phi_{self}}{\Phi_0} = 2\pi n \quad (6.1)$$

where  $\Phi_{ext}$  is the external applied flux through the loop, and is the self produced flux given by  $\Phi_{self} = L_{geo}I_{tr}$ . With

$$\gamma_{tr} = 2\pi \frac{L_{kin}}{\Phi_0} I_{tr} \quad (6.2)$$

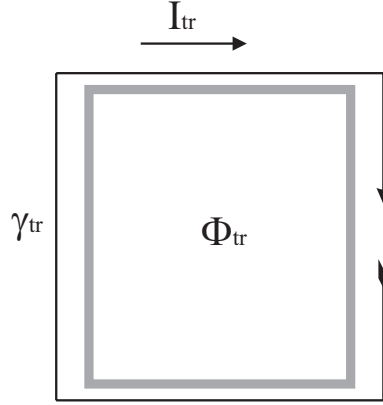


**Figure 6.4:** A solid superconducting loop can be used to trap fluxoids.. When cooled down in a magnetic field there will be a current in the ring to sustain the phase difference according to the number of fluxoids trapped in the loop.

the current in such a traploop is given by

$$I_{tr} = \frac{n\Phi_0 - \Phi_{ext}}{L_{kin} + L_{geo}} \quad (6.3)$$

where  $n$  the fluxoid number trapped in the loop, and  $\Phi_{ext}$  the applied external field. This persistent current in the traploop gives a stable phase bias to superconducting devices like a squid or a Josephson persistent current qubit.

Returning to figure 6.3, the flux quantisation rules for the two loops are

$$\gamma_1 + \gamma_{qb} + 2\pi \frac{\Phi_1}{\Phi_0} = 2\pi n_1 \quad (6.4)$$

$$\gamma_2 - \gamma_{qb} + 2\pi \frac{\Phi_2}{\Phi_0} = 2\pi n_2 \quad (6.5)$$

By realising that eq 6.4+eq 6.5 = eq 6.2 it follows that  $n_1 + n_2 = n$ . The phases over each part of the loop can be written as

$$\gamma_i = 2\pi \frac{L_{kin,i} I_i}{\Phi_0} = 2\pi \frac{L_{kin,i}}{\Phi_0} \frac{n\Phi_0 - \Phi_{ext}}{L_{kin} + L_{geo}} \quad (6.6)$$

flux quantisation is now:

$$\frac{L_{kin,1} + L_{geo,1}}{\Phi_0} I_1 + \gamma_{qb} + 2\pi \frac{\Phi_{ext,1}}{\Phi_0} = 2\pi n_1 \quad (6.7)$$

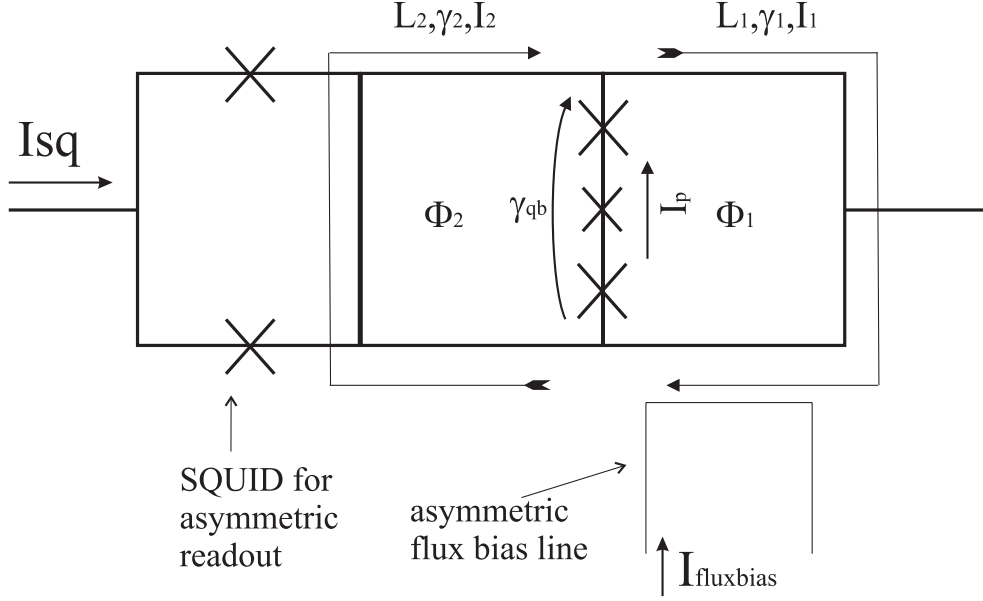


**Figure 6.5:** Gradiometer persistent current qubit with on the left the SQUID detector used for reading out the qubit. A separate line is needed to apply an asymmetric flux bias for moving the operating point around the degeneracy region.

$$\frac{L_{kin,2} + L_{geo,2}}{\Phi_0} I_2 - \gamma_{qb} + 2\pi \frac{\Phi_{ext,2}}{\Phi_0} = 2\pi n_2 \quad (6.8)$$

From this the phase over the qubit can be written as

$$\gamma_{qb} = \frac{1}{2} \frac{(L_{kin,1} + L_{geo,1}) I_1}{\Phi_0} - \frac{1}{2} \frac{(L_{kin,2} + L_{geo,2}) I_2}{\Phi_0} - \pi \frac{\Phi_1 - \Phi_2}{\Phi_0} + \pi(n_1 - n_2) \quad (6.9)$$

For the symmetric case where  $L_{kin,1} = L_{kin,2} \equiv L_{kin}$  and  $L_{geo,1} = L_{geo,2} \equiv L_{geo}$  the only term in the current that does not cancel is the persistent current of the qubit  $I_p$  so this equation reduces to to

$$\gamma_{qb} = -\pi \frac{\Phi_1 - \Phi_2}{\Phi_0} + \pi(n_1 - n_2) - 2\pi \frac{(L_{kin} + L_{geo}) I_{qb}}{\Phi_0} \quad (6.10)$$

In this equation only the qubit current  $I_{qb}$  plays a role. The inductances of the loops form the self inductance just as in the case of a single qubit. The stable phase bias to the qubit is given by the phase of the bias-ring. With  $n_1 + n_2 = n$  it is clear that for  $n \in [-3, -1, 1, 3]$  also  $n_1 + n_2$  should be odd: For an odd number of fluxoids trapped in the loop the phase bias of the qubit is given by  $\gamma_{qb} = \pi(2k+1)$  with  $k \in N$ . By applying  $\Phi_1 \neq \Phi_2$  the operating point of the qubit

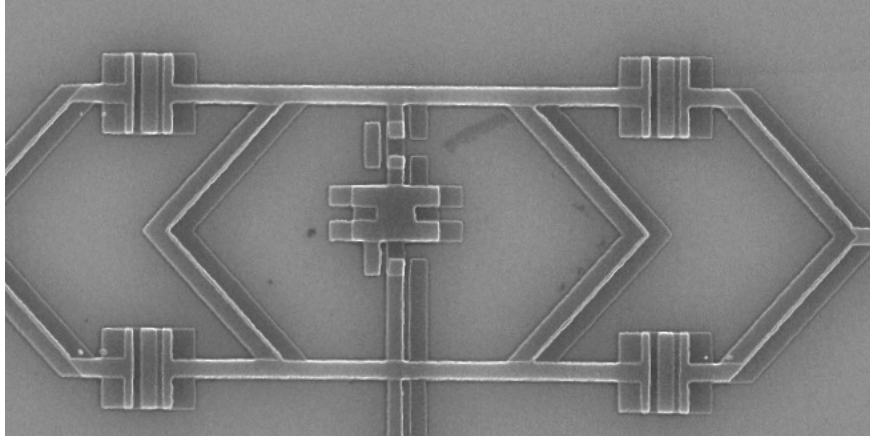


**Figure 6.6:** Gradiometer qubit with two squids attached. The solid loop in the middle is used for trapping fluxoids used for biasing the qubit around  $\gamma_{qb} = \pi$ . The extra 'H'-shaped junction in the qubit branch is to make sure the qubit junctions are attached to the same layer of the traploop. In this picture two squids are attached. However, measurements have been performed on a gradiometer qubit with one squid attached since the squids influenced each other.

can be shifted. This is done via an asymmetric bias line situated on one side of the gradiometer loop as can be seen in figure 6.5. In a similar way the squid used for detecting the qubit signal is asymmetrically attached to the gradiometer loop. Both kinetic and geometric inductance attribute to the qubit-squid coupling  $M$ . The squid picks up a part of the phase of the traploop [11]. The design is such that for the qubit at  $f = \frac{1}{2}\Phi_0$  the squid is operated at a sensitive point with respect to the flux. A gradiometer qubit design with two attached squids can be seen in figure 6.6. The hexagonal loop in the middle is used for trapping fluxoids to bias the qubit junctions. Two squids are attached to let the current noise from the measurement circuit couple into the qubits in a symmetric way. One voltage line is visible in the middle of the trap loop. This can be used to read out the signal of the squids independently. However, in a switching current measurement using attached squids the switching of one squid forces the other to switch as well.

## 6.4 Spectroscopy Measurements

Measurements have been performed on gradiometer qubit systems with trapped fluxoid bias with both one or two squids attached. No spectroscopy measurements were performed with this two squid setup so only measurements with one squid

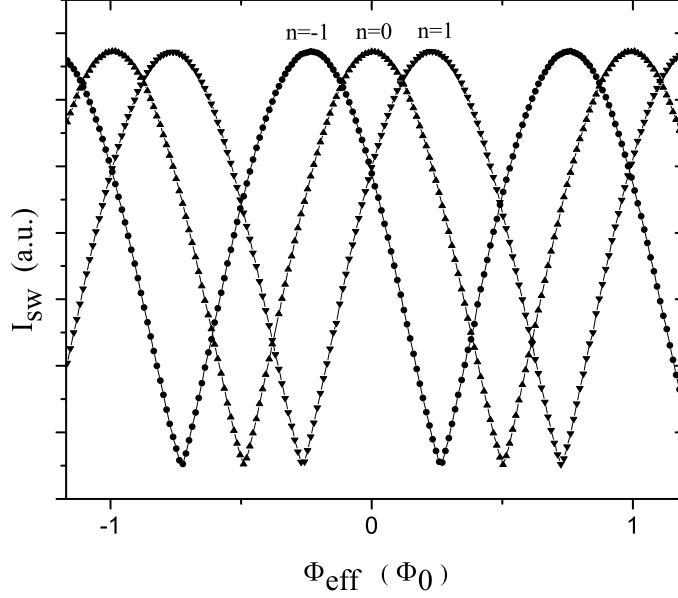


**Figure 6.7:** *SQUID switching current measurements versus the applied magnetic field for different number of fluxoids  $n$  trapped in the traploop. The shift obtained by the traploop when biasing the qubit also biases the SQUID to a sensitive point with respect to flux. External applied flux can be used to shift this point to other places on the SQUID switching current curve.*

attached will be discussed. It will be shown that trapped fluxoids can be used to bias the squid in a region where it is sensitive to the qubit signal and also bias the qubit around its operating point of  $\gamma = \pi$ . No on-chip resistors or capacitances were available, so the on-chip electrical environment was not well defined. This strongly limits the coherence.

### Flux trapping

The system is designed so that for an odd number of fluxoids trapped the squid will be in a sensitive region with respect to the signal produced by the qubit. In figure 6.7 the measured critical current is displayed for  $n = 0$ ,  $n = -1$  and  $n = 1$  fluxoids trapped in the trap loop. This trapping can be done by switching the SQUID to the finite voltage state and applying a current of  $\sim 25\mu\text{A}$ . Heating will cause the trap loop to become normal. By applying the right field for the

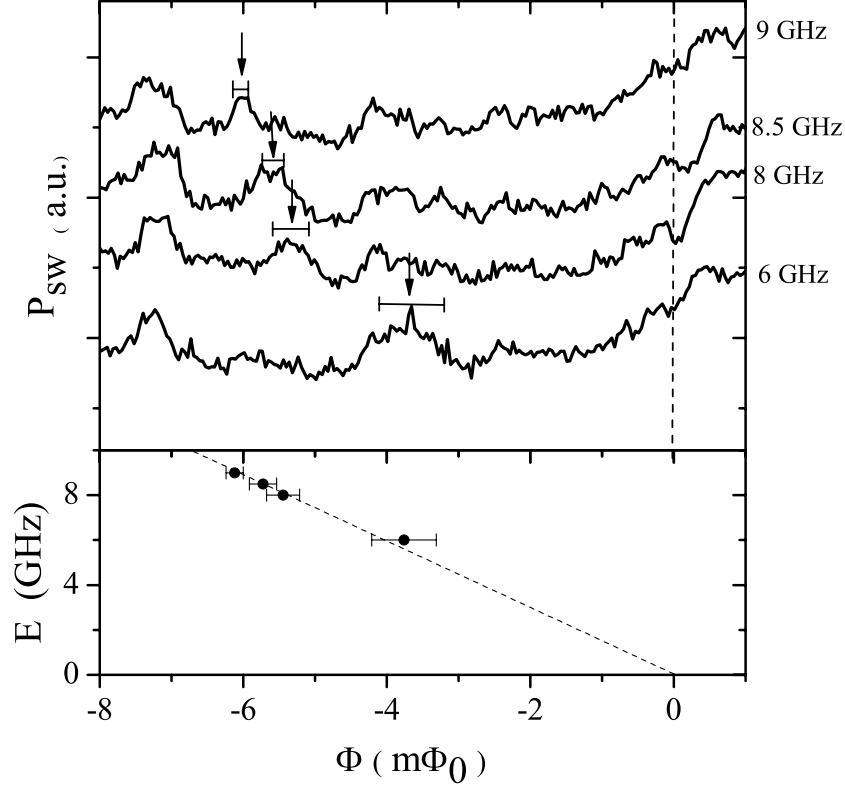


**Figure 6.8:** Spectroscopy peaks visible on one side of the qubit step. The resonance shifts with magnetic field. A persistent current  $I_p = 410\text{nA} \pm 40\text{nA}$  can be extracted from the slope of the energy versus flux. More resonances are visible which do not move with the frequency of the applied microwave radiation. These are attributed to excitation of the qubit due to resonances in the squid environment.

wanted number of fluxoids and decreasing the bias current the loop cools down and the fluxoid is trapped. The shift corresponds to an extra effective phase in the SQUID due to the phase in the trap loop of  $\Phi_{shift} = 0.23\Phi_0$  as is seen in figure 6.7. Due to the double layer structure of superconducting lines fabricated with shadow evaporation (see chapter 5) the amount of phase from the trap loop picked up by the squid is not simply proportional to the length of the line. The exact phase distribution in this line determines the effective coupling of the squid to the trap loop.

### Spectroscopy measurements

Spectroscopy measurements performed on the gradiometer qubit are shown in figure 6.8. From the shift in resonance peak position with respect to flux a persistent current of  $I_p = 410nA \pm 45nA$  is obtained. Behaviour of the resonances observed confirms the system behaves as a persistent current qubit. However, spectroscopy transitions are only visible for frequencies in the range between  $\sim 6GHz$  and  $\sim 9GHz$ , and there is a large uncertainty in the flux bias of the system, making the error in the currents rather large. Clearly visible in the data are other peaks which are attributed to a combination of qubit resonances and resonances in the measurement circuit. No on-chip shunt capacitor or resistors were present making the electrical environment rather undefined and unpredictable, and more sensitive to noise from the measurement circuit. Any asymmetry in the traploop will cause a deviation from the phase proportional to this asymmetry. From the position of the spectroscopy peaks with respect to the asymmetric flux applied it was deduced that an asymmetry in phase bias of 3 percent of  $\gamma_{qb} = \pi$  was present.

### Peak width versus power

To estimate the dephasing time  $T_2^*$  of the resonances under consideration the peak width versus power is plotted in figure 6.9. For low powers the resonance peaks start to reduce in amplitude and finally disappear. Measurements show this happens at a minimal resonance width of  $W_{fwhm} \sim 400MHz$ , indicating a dephasing time in the order of  $T_2 = 1ns$ .

The goal of obtaining an increased dephasing time could not be observed. However, the behaviour of the resonances indicate the qubit is biased using a trapped fluxoid in the trap loop and an asymmetric flux bias line can be used to move around the operating point.

## 6.5 Conclusions

Measurements show a phase bias of a Josephson persistent current qubit has been achieved by using a trapped fluxoid in a superconducting loop. The asymmetric flux bias line can be used to move around the operating point. Measurements have not shown an increase in the dephasing time of the qubit, indicating that flux noise was not the limiting factor. The absence of a well defined and filtered electrical on-chip environment made the measurement circuit and the flux bias circuit likely sources of severe decoherence. These measurements show that gradiometer qubit

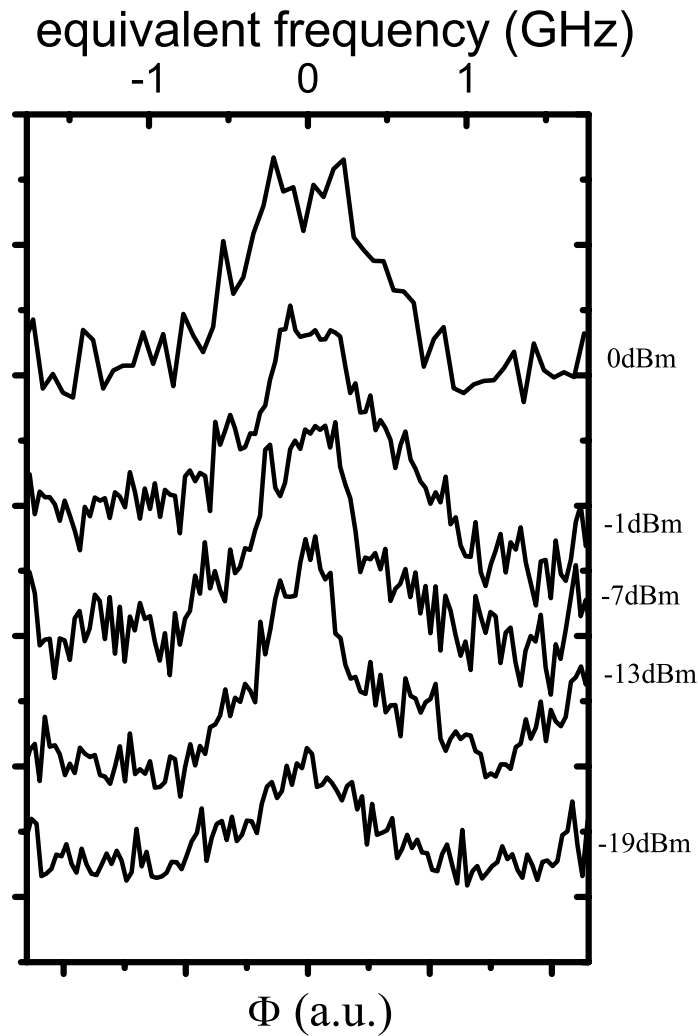


**Figure 6.9:** Spectroscopy peaks for various powers. The peak disappears when the power is lowered with a minimum observed peak width of the order of  $\sim 400\text{MHz}$ .

can be operated with fluxoid bias, opening a way to build systems where the influence of flux noise from sources away from the system is reduced.

## References

- [1] Y. Nakamura, Yu. A. Pashkin, J.S. Tsai, "Coherent control of macroscopic quantum states in a single-Cooper-pair box" *Nature* **398**, 786 (1999).

- 
- [2] D.Vion, A. Aassime, A. Cottet, P. Joyez, H. Pithier, C. Urbina, D. Esteve, M.H. Devoret, " Manipulating the quantum state of an electric Circuit", *Science*, **296**, 886,(2002).
- [3] J.M. Martinis, S. Nam, J. Aumentado, C. Urbina, "Rabi Oscillations in a large Josephson-junction qubit, *Phys. Rev. Lett.* **89**, 117901 (2002).
- [4] I. Chiorescu, Y. Nakamura, C. J. P. M. Harmans, J. E. Mooij, "Coherent quantum dynamics of a superconducting flux-qubit", *Science* **299**, 1869 (2003).
- [5] T. Duty, D. Gunnarsson, K. Bladh and P. Delsing, *Phys. rev B* **69**, 140503 (2004).
- [6] I. Chiorescu, P. Bertet, K. Semba, Y. Nakamura, C. J. P. M. Harmans, J. E. Mooij, *Nature* **431**, 159 (2004).
- [7] C.H. van der Wal, F.K. Wilhelm, C.J.P.M. Harmans, J.E. Mooij, "Engineering decoherence in Josephson persistent current qubits", *Eur. Phys. J. B.* (2001).
- [8] D.J. Van Harlingen, T.L. Robertson, B.L.T. Plourde, P.A. Reichardt, T.A. Crane and John Clarke, "Decoherence in Josephson-junction qubits due to critical current fluctuations" (2004).
- [9] E. Paladino, L. Faoro, G. Falci and R. Fazio, *Phys. Rev. Lett.* **88**, 228304 (2002).
- [10] A. Zorin, *Phys. Rev. B.* **53**, 13682 (1996).
- [11] J.B. Majer, "Superconducting Quantum Circuits", PhD Thesis (2002).
- [12] C.H. van der Wal, "Quantum Superpositions of Persistent Josephson Currents", Phd Thesis (2001).
- [13] T.P. Orlando, K.A. Delin, "Foundations of Applied Superconductivity" (1991).



# Summary

## Single and coupled Josephson junction quantum bits

In this thesis measurements on single and coupled Josephson persistent current qubits are presented. The Josephson persistent current qubit consists of a superconducting loop intersected by three Josephson junctions. When half a flux quantum is applied to the loop this system acts as a quantum two state system. The two states are associated with a clock or anti clockwise current flowing in the loop and can be measured using a SQUID magnetometer. The research presented in this thesis aimed at achieving coupling between two Josephson persistent current qubits and to show conditional gate operations in such a coupled qubit system. Also it was tried to improve the coherence properties of a single qubit by using a gradiometer type configuration to minimize influence from fluxnoise which would cause a disturbance of the energy bias of the qubit system.

The basic principles of the Josephson persistent current qubit are discussed, as well as design criteria to minimize decoherence due to the environment seen by the squid or microwave lines. A SQUID magnetometer operated in the quantum tunnelling regime is used for reading out this flux signal produced by either a single or two coupled Josephson persistent current qubits.

Spectroscopy measurements have been performed on coupled qubit systems mapping out the energy level structure of these systems. For two coupled qubits the origin and magnitude of the coupling  $J$  is derived for coupling via the geometrical inductance between the qubits. Also it is shown that coupling via a shared junction or a shared line acts the same as the geometrical coupling. Spectroscopy measurements show coupling for qubits which are mainly geometrical coupled and spectroscopy measurements on an other sample show a coupling for qubits coupled via a large shared Josephson junction. Using such a shared junction allows for the coupling to be designed within a large range. For the coupled qubit system with coupling via a large junction spectroscopy measurements from both the ground state to higher states as well as from the partially populated first excited state to higher states have been performed and the level structure

of this system is mapped out. The energy level structure is in good agreement with the 4 level approximation for two coupled qubits. Coherent Rabi oscillations between two states flipping either qubit of this system have been performed with an oscillation decay time of up to  $\sim 70ns$ . Also conditional spectroscopy has been performed by first going coherently from the ground state to a higher state and then incoherently pumping the system to other states.

Spectroscopy measurements on a gradiometer type Josephson persistent current qubit show trapped fluxoid biasing can be used to create a phase bias of  $\pi$  over the qubit junctions.

The results of this thesis show that coupling between Josephson persistent current qubits can be achieved and designed within the wanted range. Superpositions between the ground state and higher states in such a coupled qubit system have been created by performing Rabi oscillations. Also conditional spectroscopy has been performed. These results indicate that full control of the two qubit four dimensional Hilbert space is within reach. This forms a basis for future experiments on entanglement of spatially separated qubits, each with separate readout. Then this system can be used to investigate further the properties of quantum mechanics and to investigate the principles of quantum computation.

*Alexander ter Haar*

*December 2004*

# Samenvatting

## Enkele en gekoppelde Josephson junctie quantum bits

In dit proefschrift worden metingen aan enkele en gekoppelde quantum bits gepresenteerd. De Josephson persisterende stroom qubit bestaat uit een supergeleidende ring die op drie plaatsen onderbroken is door Josephson juncties. Bij een magnetische flux van een halve fluxquantum door de ring gedraagt het systeem zich als een quantum twee niveau systeem waarvan de toestanden overeenkomen met een stroom links of rechtsom door de ring. Deze stroom wordt gemeten door gebruik te maken van een SQUID magneetmeter. Het onderzoek dat hier gepresenteerd is was gericht op het koppelen van twee Josephson quantum bits. Ook is er onderzoek gedaan naar het reduceren van de gevoeligheid van het systeem voor flux ruis door gebruik te maken van een gradiometer configuratie.

De basis principes van de Josephsen persisterende stroom qubit zijn behandeld, en ook ontwerp criteria om decoherentie vanuit de omgeving, gezien door de SQUID of de microgolf lijn, te minimaliseren. Een SQUID in het quantum regime wordt gebruikt om het signaal van een enkele of van de gekoppelde qubits uit te lezen. Voor twee geometrisch gekoppelde qubits is de origine en de grootte van de koppeling afgeleid, en het is aangetoond dat kinetische koppeling werkt volgens hetzelfde principe. Door middel van spectroscopie metingen aan twee gekoppelde qubits is het energie spectrum in kaart gebracht. De koppeling tussen de qubits  $J$  is gemeten voor zowel een systeem waarin de qubits vooral geometrisch gekoppeld waren, als voor een systeem met vooral kinetische koppeling via een gedeelde Josephson junctie. Zo'n gedeelde Josephson junctie kan gebruikt worden om de koppeling over een groot bereik te ontwerpen. Voor het sample met koppeling via een gedeelde junctie is spectroscopie vanaf de grondtoestand en vanaf de eerste aangeslagen toestand uitgevoerd en de structuur van de energie niveaus is zo in kaart gebracht. Die structuur is in goede overeenkomst met het 4 niveau model voor twee gekoppelde qubits. Coherente oscillaties tussen twee toestanden zijn uitgevoerd. Ook is conditionele spectroscopy uitgevoerd door eerst coherent van de grondtoestand naar de eerste aangeslagen toestand te gaan, en vervolgens met een stralings puls een incoherent mengsel tussen de hogere toestanden te

bewerkstelligen.

Spectroscopie aan een gradiometer qubit systeem heeft aangetoond dat een ingevangen fluxoid gebruikt kan worden om een phase van  $\pi$  over de juncties aan te leggen.

Dit proefschrift toont aan dat koppeling tussen Josephson persisterende stroom qubits kan worden bewerkstelligd, en dat deze koppeling kan worden ontworpen over een ruim interval. Coherente superposities tussen twee toestanden zijn gemaakt in een gekoppeld qubit systeem door Rabi oscillaties tussen twee niveaus uit te voeren. Ook conditionele spectroscopy is uitgevoerd. Deze resultaten geven aan dat controle over de toestanden van twee gekoppelde flux qubits binnen bereik is. Dit vormt de basis voor experimenten aan quantum mechanische 'verstriktheid' (entanglement) tussen ruimtelijk gescheiden qubits, elk met een eigen uitlees systeem. Dit systeem kan dan gebruikt worden om de eigenschappen van quantum mechanica en de principes van een quantum computer verder te onderzoeken.

*Alexander ter Haar*

*December 2004*

# Curriculum Vitae

Alexander Camillus Johannes ter Haar

- 27-02-1975 Born in Nijmegen, the Netherlands.
- 1987-1993 Secondary school at the Elshof College in Nijmegen.
- 1993-2000 M.Sc. Applied Physics,  
Delft University of Technology.  
Graduate research in the Quantum Transport group of  
prof.dr.ir. J.E. Mooij.
- 2000-2004 Ph.D. research at Delft University of Technology  
under supervision of prof.dr.ir. J.E. Mooij and dr. C.J.P.M. Harmans.  
Subject: Single and coupled Josephson junction qubits



# Publications

1. *Quantum superpositions of macroscopic persistent-current states*  
C. H. van der Wal, A. C. J. ter Haar, F. K. Wilhelm, R. N. Schouten, C. J. P. M. Harmans, T. O. Orlando, S. Lloyd, and J. E. Mooij, *Science* 290, 773 (2000).
2. *Spectroscopy on two coupled superconducting flux qubits*  
J. B. Majer, F. G. Paauw, A. C. J. ter Haar, C. J. P. M. Harmans, and J. E. Mooij, Submitted to *Phys. Rev. Lett.* (2004).
3. *Coherent manipulation of two coupled Josephson Persistent Current Qubits*  
A.C.J. ter Haar, P.C. de Groot, C.J.P.M. Harmans, J.E. Mooij, *in preperation*.



